Technische Universität München
TUM School of Engineering and Design

Model Predictive Control of a Modular Multilevel Converter

Xiaonan Gao

Vollständiger Abdruck der von der TUM School of Engineering and Design der Technischen Universität München zur Erlangung des akademischen Grades eines

Doktors der Ingenieurwissenschaften

genehmigten Dissertation.

Vorsitz: Prof. Dr.-Ing. Sandra Hirche
Prüfer der Dissertation:
1. Prof. Dr.-Ing. Ralph Kennel
2. Prof. Dr.-Ing. José Rodríguez Pérez
(Universidad San Sebastián, Santiago, Chile)

Die Dissertation wurde am 22.09.2021 bei der Technischen Universität München eingereicht und durch die TUM School of Engineering and Design am 29.06.2022 angenommen.

Acknowledgment

I would like to thank Prof. Dr.-Ing. Ralph Kennel for accepting me as a PhD candidate at the Chair of Electrical Drive Systems and Power Electronics at Technische Universität München in 2016, otherwise this dissertation would not come true. He gave me the freedom to choose the doctoral topic in the beginning of my study and encouraged me when I faced problems. I really appreciate his support throughout my doctoral period.
Furthermore, I'd like to thank Prof. José Rodríguez (Universidad San Sebastián, Chile) for agreeing to be the co-examiner of my dissertation and his valuable suggestions for improving the quality of my dissertation.
It is my great pleasure to work with the colleagues at EAL. They gave me support in both my academic research and daily life in Germany. First of all, I feel grateful to Mr. Wei Tian. Without his help, our testbench could not be constructed. Many thanks to Dr.-Ing. Zhenbin Zhang and Dr.-Ing. Xinbo Cai, they gave me valuable guidance on my work. Also, I'd like to express my gratitude to Mr. Yuebin Pang Mr. Ding Dai and Dr. Genji Pei for their support when I was setting up the testbench. Dr.-Ing. Mohamed Abdelrahem, Dr. Xicai Liu, Mr. Qing Chen, Mr. Haotian Xie, Ms. Xinyue Li, Mr. Yingjie He, Ms. Ying Tang and Mr. Qifan Yang are my cooperative partners. Mr. Dehao Kong, Mr. Darshan Manoharan and Mr. Shih-Wei Su are very good friends of mine, with whom I shared many memorable moments in Munich.
I appreciate Mr. Dietmar Schuster for his work that improved our experimental testbench. Many thanks to Dr.-Ing. Julien Cordier and Mr. Stefan Klaß for their help in revising my abstract.
The financial support of the China scholarship council (CSC) is gratefully acknowledged.
At last, thanks to all my family for their support.

Munich, in June 2021
Xiaonan Gao

Abstract

This work focuses on the implementation of the model predictive control (MPC) method for modular multilevel converters (MMCs). The computational complexity is currently a major impediment to the application of MPC in MMC systems. This is due to the fact that, conventional MPC algorithms enumerate all possible insertion index combinations to make the optimal decision. In contrast, the present work considers the control problem as a quadratic program (QP) with bound constraints and then employs an infeasible active set method to work out an optimal solution efficiently. The latter is used to determine a reduced control set for MPC. Doing so greatly reduces the number of insertion index combinations and ensures that the computational burden does not increase with the number of submodules (SMs) per arm.

This dissertation then studies MMC-based motor drive systems and proposes an MPC method with a novel cost function for MMCs, which enables MMCs to operate in a wide frequency range. In contrast with conventional MPC methods, the proposed scheme can effectively control the output currents and balance the SM capacitor voltage in the low- and high-frequency range. Besides, the corresponding control structure is simpler because it does not require different control schemes under low- and high-frequency conditions.

Finally, an extrapolation technique is combined with the MPC to realize the quasi-two-level operation of the MMC. This approach accelerates the arm current commutation process of MMC and thus further suppresses the ripples of the SM capacitor voltage.

Zusammenfassung

Die vorliegende Arbeit befasst sich mit der Umsetzung der Methode der modellprädiktiven Regelung (MPC) für modulare Mehrpunktumrichter (MMCs). Die Rechenkomplexität stellt gegenwärtig ein wesentliches Hindernis zur Anwendung der MPC in MMC-basierten Systemen dar. Dies liegt daran, dass herkömmliche MPC-Algorithmen alle möglichen Kombinationen des sogenannten „insertion index“ auswerten, um die optimale Entscheidung zu treffen. Die vorliegende Arbeit hingegen betrachtet das Regelungsproblem als quadratisches Programm (QP) mit Box-Restriktionen und nutzt anschließend eine Infeasible-Active-Set-Methode zur effizienten Ermittlung einer optimalen Lösung. Letztere wird zur Bestimmung einer verkleinerten Steuermenge für die MPC herangezogen. Auf diese Weise lässt sich die Anzahl an Kombinationen des „insertion index“ deutlich senken und es wird sichergestellt, dass sich der Rechenaufwand bei steigender Anzahl an Submodulen innerhalb eines Zweigs nicht erhöht.

Ferner untersucht die Dissertation MMC-basierte Antriebssysteme. Hierbei wird eine MPC-Methode für MMCs mit einer neuartigen Kostenfunktion vorgeschlagen. Diese ermöglicht den Betrieb von MMCs in einem breiten Frequenzbereich. Im Gegensatz zu üblichen MPC-Verfahren kann der vorgeschlagene Ansatz sowohl im niedrigen, als auch im hohen Frequenzbereich die Ausgangsströme effektiv regeln und die Kondensatorspannung in den Submodulen glätten. Des Weiteren ist die zugehörige Regelstruktur einfacher, da diese keine verschiedenen Regelverfahren abhängig vom Frequenzbereich erfordert.

Schließlich wird eine Extrapolationsmethode mit der MPC kombiniert, um einen Betrieb des MMC ähnlich dem Zweipunktumrichter zu gewährleisten. Diese Vorgehensweise beschleunigt die Stromkommutierung in einem Zweig des MMC und unterstützt die Dämpfung von Oszillationen der Kondensatorspannung in den Submodulen.

Contents

CHAPTER 1

Introduction

1.1 Brief overview of high power voltage source converters

Power converters are well known in industries and academia as one of the preferred choices for high-efficiency electric power conversion instruments. Among them, voltage source converters (VSCs) have the highest market share and are widely used in industries. The VSC refers to a type of power electronic topology in which the dc side presents voltage source characteristics and the ac side voltage is regulated by pulse width modulation (PWM) technology. Nowadays, the VSCs widely used in the industry mainly include the two-level converter, neutral-point clamped (NPC) converter, flying capacitor (FC) converter, cascaded H-bridge (CHB) converter, and modular multilevel converter (MMC).

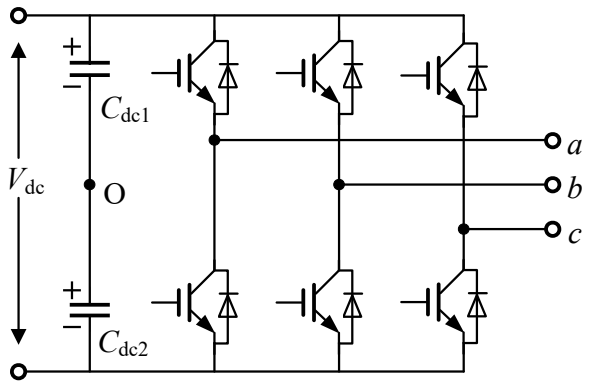

Figure 1.1: Two-level voltage source converter topology.

The two-level converter shown in Fig. 1.1 is the most classical VSC topology. However, due to its simple configuration, each semiconductor device has to support the total dc-link voltage. Therefore, it has been limited to low-voltage and low-power applications. For high dc voltage

applications, a two-level converter requires a series connection of semiconductor components to withstand a high dc-link voltage. However, this measure does not bring additional benefits in improving power quality, and the reliability of the converter will be significantly affected due to these series-connected components [1].

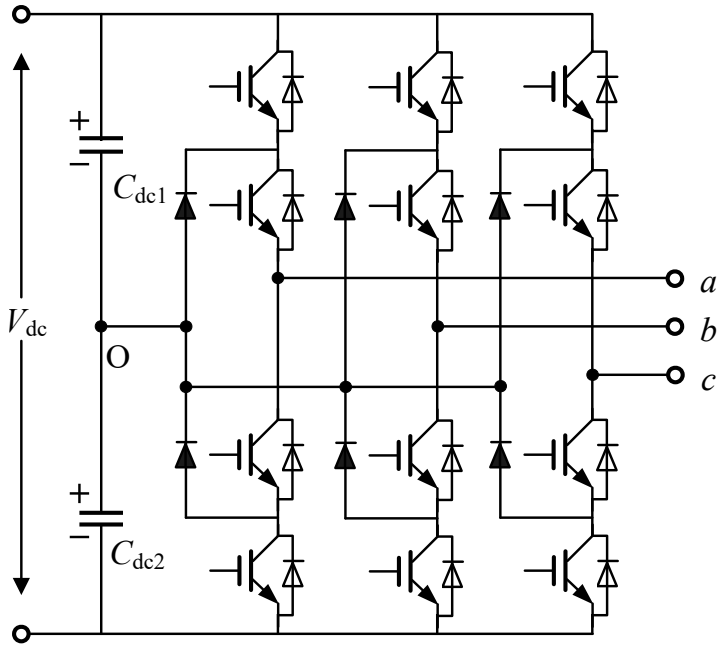

Figure 1.2: Three-level neutral-point clamped converter.

The three-level NPC shown in Fig. 1.2 is the only multilevel NPC topology popularly available in the market [2]. Although the multilevel NPC topology evolves from three-level NPC, it is difficult to be used in high voltage applications in practice. As the number of output voltage levels increases, the required diode devices will increase in a square relationship. Also, the circuit configuration and control method will become more complex. Therefore, the NPC topology is widely used in industrial medium power motor drives as well as power converters for wind and solar systems [3, 4].

The multilevel FC converter shown in Fig. 1.3 is an alternative topology for multilevel converters [5]. It is constructed with multiple cells and each cell includes a pair of switches and a flying capacitor. Because of this modular structure, a higher number of output voltage levels can be achieved by adding cells to the converter. Compared with the NPC converter, the FC converter has a naturally balanced voltage on flying capacitors, which is realized by using the phase-shifted carrier modulation (PSC-PWM) scheme with a high carrier frequency. Besides, unlike the NPC converter, the FC converter will not have the challenge of unbalanced dc-link capacitor voltages when higher output voltage levels are required. However, the capacitor voltage ripple is a great challenge in FC converters. Although a higher carrier frequency can help to reduce voltage ripples, it will also limit the power conversion efficiency of the FC converters. Therefore, the FC topology is currently attractive for high-speed drives and those applications that require low current ripples [4].

The CHB converter is another multilevel topology [6, 7], which is shown in Fig. 1.4. It employs a series connection of H-bridge submodules (SMs) structure to increase the voltage

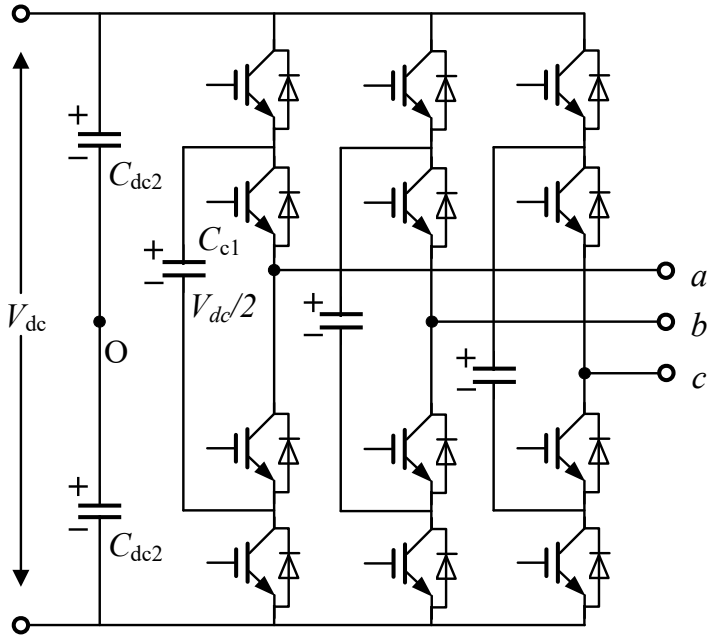

Figure 1.3: Three-level flying capacitor converter.

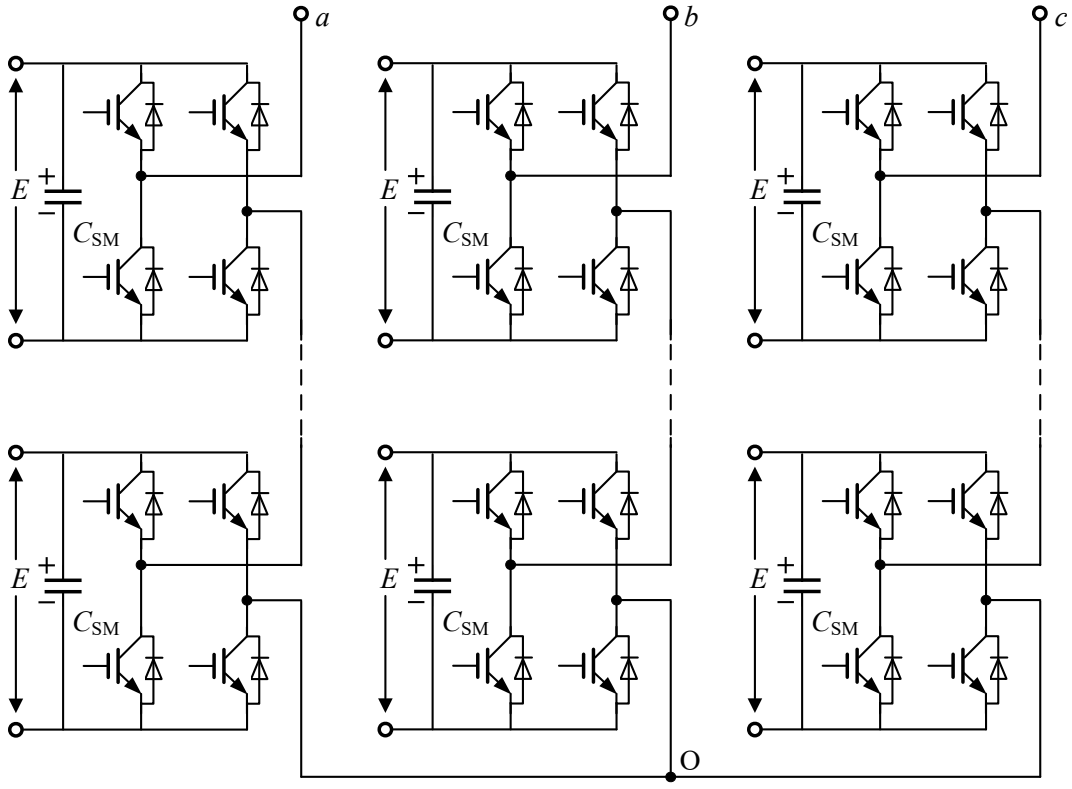

Figure 1.4: Cascaded H-bridge converter.

rating. As a result, the CHB converter can generate a higher output phase voltage level by connecting the low-voltage power modules in series. Simultaneously, a staircase-like voltage

waveform can be obtained, thereby achieving low switching frequency and low $\mathrm{d}v/\mathrm{d}t$. Besides, by using the CHB converter, low harmonic distortions can be achieved and the output filter size will be reduced. However, a phase-shifted transformer is required to provide an isolated dc source for each SMs of the CHB converter. As we know, phase-shifted transformers are usually difficult to manufacture and can cause high losses and heat dissipation when the load is not operating at its rated power. In addition, the CHB converter does not have the common dc bus, which indicates a unidirectional power flow. Therefore, all these disadvantages will limit the applications of the CHB converter in high voltage/power scenarios.

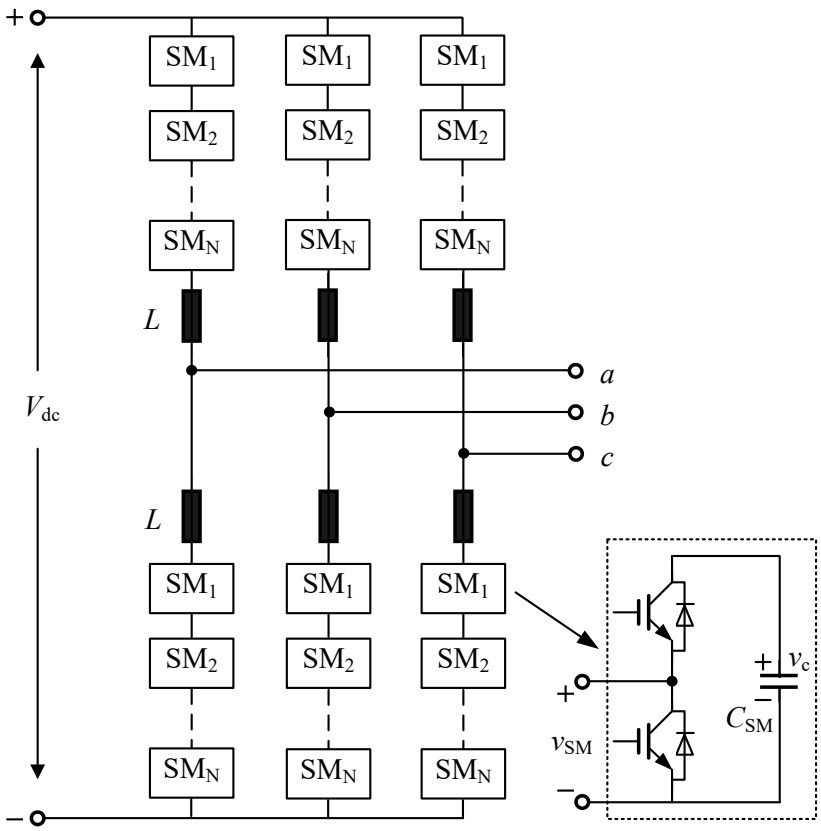

Figure 1.5: Modular multilevel converter.

It can be seen that all these above-mentioned voltage source converters have their own limitations and are difficult to meet the future requirements in high-power applications. The modular multilevel converter was introduced to eliminate these issues [8, 9]. MMC was first introduced by Marquardt in 2001 and attracted widespread attention rapidly. As it is shown in Fig. 1.5, MMC has three legs, and each leg contains two arms (upper and lower arm). Each arm is constructed with N cascaded SMs and an arm inductor L. Compared with the two-level VSC and NPC converter, MMC features a modular structure. Hence, instead of adopting the series-connected semiconductor devices, MMC can achieve higher voltage/power ratings with a cascaded connection of low-power SMs, which avoids the dynamic voltage balancing of semiconductor devices and the use of high-voltage semiconductor devices. Also, low switching frequency and low harmonic distortions can be achieved. In comparison with the CHB converter, MMC does not require the bulky transformer, which facilitates the overall size reduction

and cost reduction of the system. Moreover, MMC has a useful dc bus, which is crucial for many high-power applications. At last, MMC shows better modularity and scalability and thus it can reach a higher voltage/power rating. Due to these excellent features, MMC is very suitable for high-voltage high-power applications. In fact, MMC has greatly promoted the development of VSC-based high-voltage direct current (HVDC) transmission technology [10, 11]. The list of MMC-based HVDC transmission projects is summarized in Table 1.1.

Table 1.1: MMC-based HVDC projects

Project Name	Power (MW)	DC Voltage (±kV)	Length (km)	Year	Company
Trans Bay, USA	400	200	85	2010	Siemens
Nanhui wind farm integration, China	18	30	85	2011	SGCC
Nanao multi-terminal, China	200	160	9	2013	CSG
Zhoushan multi-terminal, China	1000	200	141	2014	SGCC
BorWin2, Germany	800	300	200	2015	Siemens
DolWin1, Germany	800	320	165	2015	ABB
HelWin1, Germany	576	250	130	2015	Siemens
INELFE, France-Spain	2000	320	64	2015	Siemens
Xiamen island Infeed, China	1000	320	11	2015	SGCC
DolWin2, Germany	1000	320	135	2016	ABB
DolWin3, Germany	900	320	160	2017	Alstom
Maritime Link, Canada	500	200	360	2017	ABB
Caithness-Moray Link, UK	1200	320	160	2018	ABB
COBRAcable, Netherlands-Denmark	700	320	325	2019	Siemens
NordLink, Germany-Norway	1400	525	570	2020	ABB

MMC has also been widely concerned in many fields such as medium-voltage (MV) motor drives [12, 13], static synchronous compensator (STACOM) [14, 15], and unified power quality conditioner [16, 17]. Recently, MMC has attracted more and more attention from industry and academia and a series of progress has been made in the evolution of topologies, modulation techniques, control schemes and industrial applications.

1.2 Overview of model predictive control methods for MMC

Although MMC has many advantages and has achieved many industrial applications, it requires more complex control methods to achieve multiple objective regulations compared with other converters. The control problem of MMC is quite challenging owing to its multi-input-multi-output (MIMO) control structure. Generally speaking, three main control tasks need to be fulfilled for the MMC: ac-side power/current control, dc-link voltage/current control, and arm-balancing control (internal control). These objectives can be realized by classical control methods (modulation-based control methods) or model predictive control (MPC) methods.

The classical control methods can be classified into direct modulation-based control methods and indirect modulation-based control methods. The main difference between these two types of methods is the calculation method for the insertion index. The direct modulation-based control inherently balances the energy of different arms, thus greatly simplifying the control of the MMC system [18]. However, as the arm output voltage cannot track its reference correctly, a considerable circulating current, especially twice line frequency components, appears in the leg current, which needs to be suppressed by increasing the inductance of arm inductors or by circulating-current controllers. In [19, 20], a proportional-integral (PI) controller in dq rotating frame is used to suppress the twice-line frequency component of the circulating current. This parasitic component can also be suppressed by proportional-resonant (PR) controllers in the abc/$\alpha\beta$ stationary frame [21–23]. However, both PI and PR controllers cannot guarantee the dynamic performance of the MMC system as MMC has a wide range of operational points [24, 25].

In indirect modulation-based control methods, the ideal insertion index is applied and thus the arm output voltage adheres to its reference. Besides, no parasitic components appear in the circulating current. However, the balancing of each arm energy will be marginally stable [26]. Therefore, the arm energy balancing control is required. In [26], two independent controllers are applied to control the total arm energies in one phase and the difference between upper and lower arm energies in the same phase. In [27], a comprehensive arm energy control method suitable for generalized dc bus control is proposed. Besides, the decoupled control of dc-link current, circulating currents, and ac-side currents can be achieved by using this method.

When the insertion indices are determined by direct modulation-based control or indirect modulation-based control, the capacitor voltage balancing among the submodules in each arm should be considered. The capacitor voltage balancing control can be achieved by using a linear proportional controller for each SM [28, 29] or a simple sorting algorithm for each arm [30, 31].

Overall, implementing these conventional control methods with multiple PI/PR control loops for the MMC system is quite challenging as the tuning effort for these controllers is heavy especially when multi-objective regulation is required. In addition, conventional methods are difficult to guarantee the fast control actions during transients and good steady-state performance when the switching frequency is low [25].

The drawbacks of conventional methods prompt researchers to investigate modern control methods. In recent years, the model predictive control method as an alternative control scheme for the MMC system has drawn more and more attention due to its prominent features, such as its straightforward implementation, ability to control multiple objectives in a single cost function, excellent dynamic response and easy handling of nonlinearities and constraints. As previously discussed, MMC is a MIMO system and MPC has the advantage of controlling such a system compared with the conventional methods mentioned above. However, the main challenge of using MPC for the MMC is the large computational burden. Therefore, almost all the research studies focus on reducing the computational complexity of MPC for the MMC in the past few years.

Initially, the direct finite control set (FCS)-MPC was first employed to the MMC in [32], where the MPC controller has been used to control the ac-side currents, SM capacitor voltages, and circulating currents by evaluating all the C_{2N}^{N} possible switching states per phase, where N is the number of SMs in each arm. However, it can be seen that the number of the switching states increases significantly when N increases, which leads to a huge computational

burden. Besides, with this method, the MMC can only produce $N+1$ output phase voltage levels. In [33], the performance of the MPC method was compared with that of the conventional method based on cascaded PI controllers [28]. With this method, the output current and SM capacitor voltages can be controlled while suppressing circulating currents. Besides, $2N+1$ output phase voltage levels can be achieved. However, the proposed MPC controller needs to evaluate all the 2^{2N} possible switching states to select the optimal one, which leads to a huge computational burden. In order to reduce the computational burden, an improved MPC method was proposed in [34]. In this method, the insertion index combinations become $N+1$ rather than C_{2N}^{N} per phase but the voltage sorting algorithm has to be integrated. Based on the similar idea in [34], a grouping-sorting-optimized MPC method for the MMC was proposed in [35] to further decrease the computational burden, from $N+1$ to $2X+M+3$ ($N=M\times X$). With this method, the optimal group combination was first determined and the optimal combination of the inserted number of SMs can be obtained in the second stage. However, the MMC can only provide $N+1$ phase voltage levels with these methods mentioned in [34, 35]. Almost at the same time as [34], an indirect FCS-MPC scheme for MMCs has been proposed in [36]. Similarly, this method decoupled the control of SM capacitor voltages from the cost function and used an external voltage sorting algorithm. Unlike [34], with this scheme the MMC can provide up to $2N+1$ phase voltage levels but the total number of possible control options has increased to $(N+1)^2$ in each phase. In [37], a fast MPC method for MMCs has been proposed. In this method, only two or three adjacent voltage levels need to be evaluated in the optimization process regardless of the number of SMs and thus $\mathrm{d}v/\mathrm{d}t$ can be limited effectively. However, the dynamic performance of these methods will be influenced by sacrificing a large number of the possible control options. In [38–41], the voltage–level based MPC methods for MMC have been proposed. In these methods, the number of control options evaluated in each control cycle depends on the allowed range of the sum of the upper and lower insertion indices in each phase based on the output voltage level. Consequently, the computational burden increases linearly when the sum boundary increases.

So far, all the mentioned MPC methods are based on the per-phase model of MMC in order to reduce the computational complexity. However, the per-phase model is not an accurate model for MMC and thus it is not suitable for the FCS-MPC method. Some experiments show that the control performance for MMC will be degraded when FCS-MPC uses such an inaccurate model [25]. Besides, the dc-link current/voltage cannot be controlled directly by using the per-phase model based MPC method. Also, it is difficult to apply the per-phase model based MPC scheme for the MV motor drive applications as the common-mode voltage cannot be controlled directly.

In order to overcome the disadvantage of the per-phase model, a three-phase model based MPC was presented in [42, 43]. In [42], a dual-stage MPC method based on the three-phase model was proposed which needs to evaluate $(N+1)^3$ switching vectors at the first stage and $C_N^{N/2}$ switching states per arm at the second stage. It can be seen that the biggest obstacle to applying the three-phase model based MPC method is the huge computational burden. The possible switching combinations increase to $(N+1)^3$ for the $N+1$ phase voltage levels [42,43] or $(N+1)^6$ for $2N+1$ phase voltage levels.

In the last few years, modulated MPC methods for the MMC have attracted attention in academia [44–47]. In [44], a model predictive current controller with the multilevel PWM scheme has been proposed. However, this method used off-the-shelf solvers, which was dif-

ficult to be implemented in the real-time control system. A different modulated MPC method has been proposed in [45]. In this method, two voltage levels were selected to control the ac current and suppress the circulating current. Based on the similar idea, a more computationally efficient modulated MPC method for the MMC has been proposed in [47]. However, in these experimental verification methods [45–47], only the case of the per-phase model of MMC has been considered and the steady-state performance under the high modulation index condition has not been discussed.

Overall, it is necessary to find a computationally efficient way to realize the three-phase model based MPC method for the MMC system to achieve better steady-state performance and fast dynamic response, especially when MMC is operating at high modulation index.

1.3 Challenges and issues of MPC for MMC

MPC is a very simple and intuitive control method. It is possible to eliminate the hierarchical control structure and PWM modulators which are typically used in the control scheme for the MMC to obtain very fast dynamic responses and low average switching frequency. Besides, the MPC method can easily handle nonlinearities and constraints. Therefore, by using the MPC scheme, the linearization process of the system model for a given operating point can be avoided and the operating range will be extended. These benefits make MPC widely used in high-power converters. Although the MPC method is popular, it has various challenges when it comes to the MMC:

1) Computational complexity brought by the three-phase model based MPC: As we have discussed in Section 1.2, the per-phase model based MPC has been used in most of the literature due to its simplicity and low computational complexity. In the per-phase model, each leg of the MMC is considered independent, and the common-mode voltage between the ac-side neutral point and the dc-link virtual midpoint is neglected. Under this assumption, the dynamics of current components (ac-side current and circulating current) in each phase are independent of other phases. However, without considering the effect of the common-mode voltage, the per-phase model based MPC method will lead to a higher total harmonic distortion (THD) of the ac-side current in comparison with the three-phase model based MPC scheme [25]. Besides, the per-phase model based method cannot achieve the decoupled control of the dc-link current, circulating currents, and ac-side currents. Also, the common-mode voltage cannot be controlled directly and thus the medium-voltage motor control is difficult to be realized with the per-phase model. Therefore, it is necessary to apply the three-phase model for the MPC in some cases. However, the biggest obstacle to applying the three-phase model based MPC method for the MMC is the large computational burden. This is because the dynamics of the current components depend on the six arm voltages. Therefore, the number of the possible insertion index combinations increases to $(N+1)^3$ for the $N+1$ phase voltage level [42, 43] or $(N+1)^6$ for $2N+1$ phase voltage level. It can be seen that even if N is small, the number of insertion index combinations required to be evaluated is high under the $2N+1$ phase voltage level condition, which makes the three-phase model based MPC method difficult to be implemented in real time.

2) How to use MPC to realize the MMC-based motor drive control: As we know, low-frequency operation has been a major problem of MMC-based motor drive applications owing to the high ripple amplitude of capacitor voltages. The circulating current injection method is the common measure, which allows MMC to operate at low frequency. In order to achieve the low-frequency operation of MMC, the injection method has to compensate for the low-frequency pulsating power in the SM capacitors by injecting the high-frequency common-mode voltage and circulating currents. This requires the control method with the ability to accurately track the common-mode voltage and circulating currents. However, with FCS-MPC, MMC can only generate integer insertion indices, which means that the common-mode voltage and circulating currents cannot be tracked exactly, especially in the case of high modulation index. This will lead to a large steady-state error in the energy of the upper and lower arms, or even to system instability due to the divergence of the energy between the upper and lower arms. How to realize the operation of MMC at a low frequency based on the FCS-MPC method is an open issue. In other words, the key is how to control the arm energy of MMC by FCS-MPC. The most straightforward idea is to put the control objective of arm energy into the cost function. However, the time constants of arm energy and other control variables (such as ac currents and dc current) are very different and the conventional form of the cost function [36] is difficult to realize the control for variables with different time constants within a short prediction horizon. Therefore, for the conventional FCS-MPC scheme, it is difficult to achieve MMC-based motor drive control. In fact, to the best of the author's knowledge, little or no effort has been made to develop an FCS-MPC method for MMC-based motor drive applications due to the limitation of the conventional form of the cost function. Therefore, it is necessary to design a novel cost function to deal with the different time-constant control variables and realize the operation of MMC in a wide frequency range.

3) Selection of weighting factors: In MPC methods, the weighting factor adjustment is one of the major challenges, especially when multiple control objectives need to be fulfilled. The weighting factor indicates the importance of one control objective relative to the others. The tuning process of weighting factors is difficult. This is because the variance in one control objective affects the performance of other objectives and the difficulty increases as the number of control objectives increases. Besides, the optimal weighting factors may vary with the operating point of the control system. Although some studies have given guidance on the selection of weighting factors (the per-unit method [48] and empirical method [49]), it is still an open issue.

In this work, the first two issues, the computational burden reduction and the novel cost function design to deal with the low-frequency operation of MMC, have been addressed.

1.4 Contributions

This dissertation mainly focuses on the application of MPC technology to realize the control of MMC.

Firstly, an MPC method based on a bound-constrained quadratic programming (QP) solver is proposed in this work. The control problem for the MMC system based on the MPC method

has been formulated as a QP problem with simple bounds. After that, an infeasible active-set method [50] has been employed to obtain the optimal solution to this control problem. Then, this continuous solution can be used to realize the modulated MPC scheme. Compared to the conventional modulated MPC schemes [46, 47, 51], due to the use of the optimal solution, the proposed method can provide a better control performance when the MMC operates at high modulation indices or transients. To further reduce the average switching frequency, a computationally efficient FCS-MPC method has been implemented based on this optimal solution. This method adopts the optimal solution obtained by the QP solver to determine a reduced control set for FCS-MPC. Compared to the conventional algorithm that has to enumerate all possible insertion index combinations $(N+1)^6$ to make the optimal decision, the proposed method greatly reduces the number of insertion index combinations to be evaluated and ensures that the computational burden does not increase with the number of SMs per arm. Therefore, the proposed FCS-MPC method seems promising for HVDC applications, in which N is large.

Secondly, in order to enable MMC to operate in a wide frequency range, an MPC scheme with a novel cost function has been proposed to realize the internal dynamic control of the MMC. Different from the square error type cost function used in the conventional MPC scheme for the MMC [25, 36], the proposed cost function can automatically regulate the power according to its related energy error. Instead of directly controlling the arm/phase energy of the MMC, it is easy to achieve control of the corresponding arm/phase power in the MPC scheme. This is because compared with energy, the time constant of power is closer to the other control variables (ac-currents, circulating currents, and dc-link current). As we know, MPC is difficult to realize the control for variables with largely different time constants when the prediction horizon is short. By using this novel cost function, this problem can be avoided. Besides, the proposed method not only achieves satisfactory performance at low frequencies but also works effectively at high frequencies, and thus it is particularly suitable for MMC-based MV motor drive applications.

At last, to further reduce the voltage ripple of the SM capacitor or the required amount of SM capacitance, the quasi-two-level (Q2L) operation mode of the MMC based on the MPC technique has been studied. The Q2L operation mode mimics the operation of the conventional two-level inverter. Unlike the output rectangle waveform of the two-level inverter, a staircase waveform for the Q2L operation has been applied, which can limit the $\mathrm{d}v/\mathrm{d}t$ of the output voltage and guarantee the voltage balancing between different SMs. It can be seen that the long-time charging/discharging of the SM capacitor at low frequency can be avoided by using the Q2L operation mode for the MMC. Instead, the arm energy variation only occurs during the arm current commutation process in the ideal case. Therefore, the completion speed of the commutation process is the key. In this work, the MPC with extrapolation technique has been used to control the arm current commutation process. With this method, MMC can complete the commutation process as quickly as possible and thus the ripple amplitude of SM capacitor voltages can be suppressed significantly at low frequencies.

1.5 Outline

The outline of this dissertation is as follows:

In Chapter 2, two different mathematical models of MMC, namely, the per-phase model and the three-phase model, have been discussed. Besides, the power analysis based on these two

different models has been provided.

Chapter 3 presents a unified method to solve the computational burden brought by MPC based on the three-phase model. A fast bound-constrained quadratic programming method has been employed to obtain the continuous optimal solution of the insertion indices. Then, the modulated MPC scheme can be implemented based on the optimal solution. Furthermore, based on this optimal solution, the search space for the FCS-MPC method will be greatly reduced from $(N+1)^6$ to 2^6 and is independent of the number of SMs per arm.

In Chapter 4, a novel cost function has been designed to allow the MMC to operate over a wide frequency range. The realization method for FCS-MPC and modulated MPC based on this novel cost function has been provided in this chapter.

Following, a particular operation mode (Q2L mode) of the MMC has been investigated in Chapter 5. In this chapter, an efficient arm current commutation control method using MPC with extrapolation technique has been proposed. By using this method, the commutation process can be completed as quickly as possible. As a result, large voltage fluctuations that occur during the commutation process will be avoided.

At last, the whole work is summarized in Chapter 6.

CHAPTER 2

System modeling and control

2.1 Introduction

In this chapter, fundamental aspects of modular multilevel converter (MMC) are considered. Unlike many other converters, MMC has relatively complex models and control strategies. For this reason, the MMC topology has been described at first for system modeling. Next, the per-phase model and three-phase model of the MMC will be introduced. Due to the use of different models, two different definitions of the circulating current are derived. The power analysis will be given based on different circulating currents. These models and related power analysis are the basis for the control system design. At last, two arm-balancing (internal) control methods combined with the model predictive control (MPC) technique will be applied to the MMC system. The corresponding experimental results are also provided.

2.2 Topology of MMC

Fig. 2.1 shows the topological structure of a three-phase MMC operating in the inverter mode. It can be seen that the three-phase MMC has three legs, and each leg contains two arms (upper and lower arms). Each arm is constructed with N cascaded submodules (SMs) and an arm inductor L (neglecting the resistance of the inductor R). "O" is the virtual midpoint of the dc link and "N" is the neutral point of the ac side. $i_{\mathrm{u}a}$, $i_{\mathrm{l}a}$, $i_{\mathrm{u}b}$, $i_{\mathrm{l}b}$, $i_{\mathrm{u}c}$ and $i_{\mathrm{l}c}$ are the currents flowing through the upper and lower arms in three phases, respectively. $v_{\mathrm{u}a}$, $v_{\mathrm{l}a}$, $v_{\mathrm{u}b}$, $v_{\mathrm{l}b}$, $v_{\mathrm{u}c}$ and $v_{\mathrm{l}c}$ represent the voltages produced by the upper and lower arms in three phases respectively. $v_{\mathrm{s}a}$, $v_{\mathrm{s}b}$ and $v_{\mathrm{s}c}$ are the equivalent ac-side output voltages of the MMC. V_{dc} and i_{dc} are the dc-link voltage and current, respectively.

As shown in Fig. 2.1, the standard half-bridge SM has been applied in this work. It consists of two insulated-gate bipolar transistors (IGBTs) and one capacitor connected across both IGBTs. Based on such a structure, each SM has three switching states:

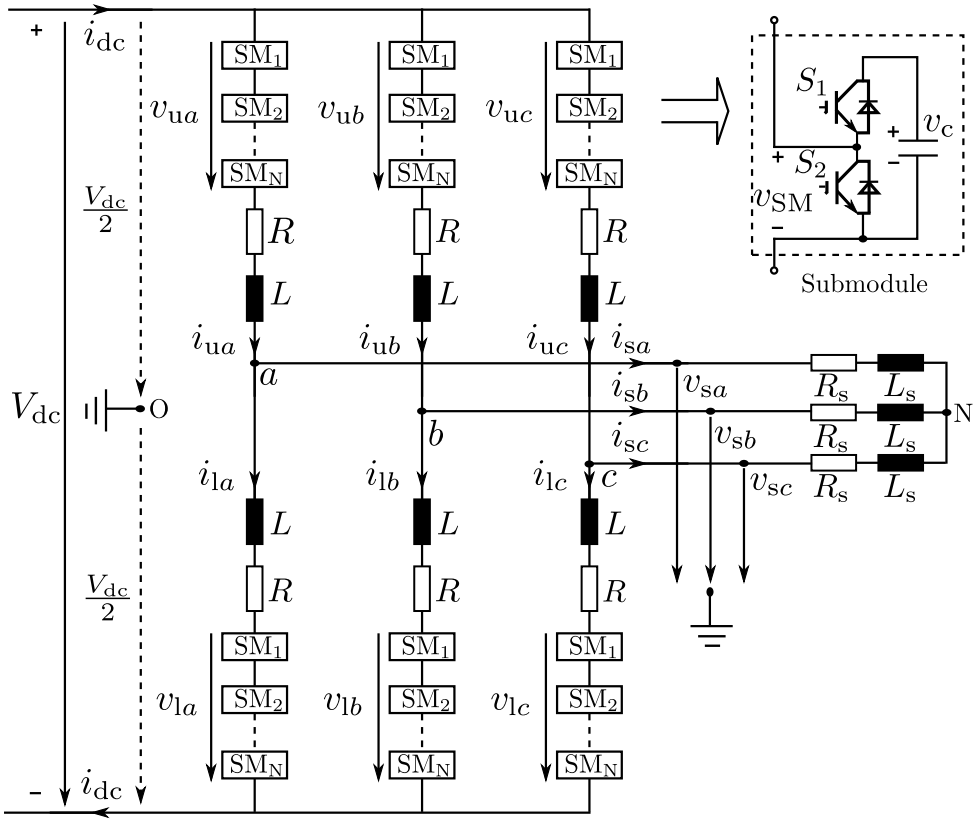

Figure 2.1: The configuration of a three-phase MMC.

1) Inserted: the upper IGBT S_1 is turned on and the lower IGBT S_2 is turned off. In this state, the capacitor is inserted in the arm circuit and provides the voltage v_c on the terminal of the SM. In this case, the SM capacitor will be charging or discharging based on the direction of the arm current.

2) Bypassed: the upper IGBT S_1 is turned off and the lower IGBT S_2 is turned on. The capacitor is bypassed in this case and the terminal voltage of the SM is zero. The capacitor voltage remains constant regardless of the arm current.

3) Blocked: Both S_1 and S_2 are turned off. The capacitor can charge through the diode of S_1 but cannot discharge. This state is often used for the uncontrollable charging process of the MMC. It can also be used to protect the IGBT from overcurrent in a short time.

It can be seen that by selecting the appropriate number of SMs to insert in the arm, the desired arm output voltage can be generated, which is the total voltage of the inserted SMs.

2.3 Mathematical models of MMC

The mathematical model of the MMC is the foundation for the control designs, especially for the MPC method. Using either the per-phase model or the three-phase model of MMC for MPC mainly depends on the applications. Usually, the per-phase model is used for MMC-based

HVDC applications, in which the number of SMs in each arm is high. Instead, the three-phase model is employed in the MMC-based medium voltage motor drives, in which the number of SMs is low. In the following sections, the per-phase model and three-phase model for the MMC will be derived.

2.3.1 Per-phase model of MMC and its power analysis

2.3.1.1 Per-phase model of the MMC

In the per-phase modeling, each phase is regarded as independent and thus the dynamics of current components are only related to the dc link and the leg on which they are located. The benefit of using this model is that each phase of the MMC can be controlled independently. The control designs can be simplified by using this model. However, it should be noted that this assumption holds only if the three-phase MMC system is well-balanced.

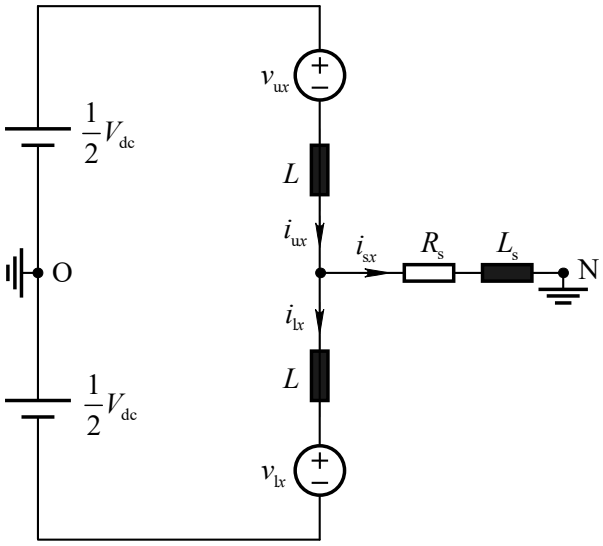

Figure 2.2: Per-phase equivalent circuit of the MMC.

The equivalent circuit of phase x is shown in Fig. 2.2. According to Kirchhoff's voltage law, the upper and lower arm voltages with respect to the midpoint of the dc link can be obtained as

$$\begin{aligned} \frac{V_{\mathrm{dc}}}{2} &= v_{\mathrm{u}x} + L\frac{\mathrm{d}i_{\mathrm{u}x}}{\mathrm{d}t} + R_{\mathrm{s}}i_{\mathrm{s}x} + L_{\mathrm{s}}\frac{\mathrm{d}i_{\mathrm{s}x}}{\mathrm{d}t}, \\ \frac{V_{\mathrm{dc}}}{2} &= v_{\mathrm{l}x} + L\frac{\mathrm{d}i_{\mathrm{l}x}}{\mathrm{d}t} - R_{\mathrm{s}}i_{\mathrm{s}x} - L_{\mathrm{s}}\frac{\mathrm{d}i_{\mathrm{s}x}}{\mathrm{d}t}. \end{aligned} \tag{2.1}$$

The control objectives concerning current components can be divided into two parts: ac-side currents and circulating currents. The ac-side current of phase x can be obtained with

$$i_{\mathrm{s}x} = i_{\mathrm{u}x} - i_{\mathrm{l}x}. \tag{2.2}$$

The circulating current is defined as

$$i_{\mathrm{cir}x} = \frac{i_{\mathrm{u}x} + i_{\mathrm{l}x}}{2}. \tag{2.3}$$

The dc-link current can be derived as

$$i_{\mathrm{dc}} = \sum_{x=a,b,c} i_{\mathrm{cir}x}. \tag{2.4}$$

Note that the definition of the circulating current in the per-phase model will be different from that in the three-phase model. According to the definition in (2.3), there will be a dc component in the circulating current $i_{\mathrm{cir}x}$. When the ac side is well balanced, the dc-link current i_{dc} should be evenly distributed to the three-phase circulating currents to minimize converter losses, that is $i_{\mathrm{cir}x} = i_{\mathrm{dc}}/3$.

Based on (2.1)-(2.3), the dynamics of ac-side currents and circulating currents can be derived as

$$\begin{aligned} \frac{\mathrm{d}\boldsymbol{i}_{\mathrm{s}x}}{\mathrm{d}t} &= \frac{1}{2L_{\mathrm{s}}+L}\left(\boldsymbol{v}_{\mathrm{l}x} - \boldsymbol{v}_{\mathrm{u}x} - 2R_{\mathrm{s}}\boldsymbol{i}_{\mathrm{s}x}\right) \\ \frac{\mathrm{d}\boldsymbol{i}_{\mathrm{cir}x}}{\mathrm{d}t} &= \frac{1}{2L}\left(\boldsymbol{V}_{\mathrm{dc}} - \boldsymbol{v}_{\mathrm{l}x} - \boldsymbol{v}_{\mathrm{u}x}\right) \end{aligned} \tag{2.5}$$

where

$$\boldsymbol{i}_{\mathrm{s}x} = \begin{bmatrix} i_{\mathrm{s}a} \\ i_{\mathrm{s}b} \\ i_{\mathrm{s}c} \end{bmatrix}, \quad \boldsymbol{v}_{\mathrm{l}x} = \begin{bmatrix} v_{\mathrm{l}a} \\ v_{\mathrm{l}b} \\ v_{\mathrm{l}c} \end{bmatrix}, \quad \boldsymbol{v}_{\mathrm{u}x} = \begin{bmatrix} v_{\mathrm{u}a} \\ v_{\mathrm{u}b} \\ v_{\mathrm{u}c} \end{bmatrix}, \quad \boldsymbol{i}_{\mathrm{cir}x} = \begin{bmatrix} i_{\mathrm{cir}a} \\ i_{\mathrm{cir}b} \\ i_{\mathrm{cir}c} \end{bmatrix}, \quad \boldsymbol{V}_{\mathrm{dc}} = \begin{bmatrix} V_{\mathrm{dc}} \\ V_{\mathrm{dc}} \\ V_{\mathrm{dc}} \end{bmatrix}.$$

As can be seen in (2.5), the ac-side current $i_{\mathrm{s}x}$ can be controlled by the difference between the lower and upper arm voltages ($v_{\mathrm{l}x} - v_{\mathrm{u}x}$). Similarly, the circulating current $i_{\mathrm{cir}x}$ can be regulated by the sum of the upper and lower arm voltages ($v_{\mathrm{u}x} + v_{\mathrm{l}x}$) and the dc-link voltage (V_{dc}).

It is worth noting that due to the SM balancing control, all the SM capacitor voltages in the same arm can be controlled to the mean value and the small individual differences between the SM capacitor voltages can be neglected in the dynamic model. Therefore, the upper and lower arm voltages can be expressed as follows:

$$\begin{aligned} v_{\mathrm{u}x} &= \frac{n_{\mathrm{u}x}}{N}\sum_{i=1}^{N} v_{\mathrm{c,u}x}^{i} = n_{\mathrm{u}x}\bar{v}_{\mathrm{u}x}, \\ v_{\mathrm{l}x} &= \frac{n_{\mathrm{l}x}}{N}\sum_{i=1}^{N} v_{\mathrm{c,l}x}^{i} = n_{\mathrm{l}x}\bar{v}_{\mathrm{l}x}. \end{aligned} \tag{2.6}$$

where $v_{\mathrm{c,u}x}^{i}$ and $v_{\mathrm{c,l}x}^{i}$ are the ith SM capacitor voltages in the upper and lower arms of phase x, respectively. $\bar{v}_{\mathrm{u}x}$ and $\bar{v}_{\mathrm{l}x}$ are the average capacitor voltages of the upper and lower arms. $n_{\mathrm{u}x}$ and $n_{\mathrm{l}x}$ are the insertion index of the upper and lower arms in phase x. The insertion index is the number of inserted SMs in the related arm and it has $N+1$ discrete values (from 0 to N).

In order to implement the MPC method, a discrete-time model of the system is required. By using the forward Euler method for (2.5), the discrete-time model can be expressed as:

$$\begin{aligned} \boldsymbol{i}_{\mathrm{s}x}(k+1) &= \alpha_1\boldsymbol{i}_{\mathrm{s}x}(k) + \alpha_2\left(\boldsymbol{v}_{\mathrm{l}x}(k) - \boldsymbol{v}_{\mathrm{u}x}(k)\right), \\ \boldsymbol{i}_{\mathrm{cir}x}(k+1) &= \boldsymbol{i}_{\mathrm{cir}x}(k) + \alpha_3\left(V_{\mathrm{dc}}(k) - \boldsymbol{v}_{\mathrm{l}x}(k) - \boldsymbol{v}_{\mathrm{u}x}(k)\right). \end{aligned} \tag{2.7}$$

where

$$\alpha_1 = 1 - \frac{2R_{\mathrm{s}}T_{\mathrm{s}}}{2L_s+L}, \alpha_2 = \frac{T_{\mathrm{s}}}{2L_s+L}, \alpha_3 = \frac{T_{\mathrm{s}}}{2L},$$

$$\boldsymbol{v}_{\mathrm{u}x}(k) = \begin{bmatrix} n_{\mathrm{u}a}\bar{v}_{\mathrm{u}a}(k) & n_{\mathrm{u}b}\bar{v}_{\mathrm{u}b}(k) & n_{\mathrm{u}c}\bar{v}_{\mathrm{u}c}(k) \end{bmatrix}^{\mathrm{T}},$$
$$\boldsymbol{v}_{\mathrm{l}x}(k) = \begin{bmatrix} n_{\mathrm{l}a}\bar{v}_{\mathrm{l}a}(k) & n_{\mathrm{l}b}\bar{v}_{\mathrm{l}b}(k) & n_{\mathrm{l}c}\bar{v}_{\mathrm{l}c}(k) \end{bmatrix}^{\mathrm{T}},$$
$$\boldsymbol{V}_{\mathrm{dc}}(k) = \begin{bmatrix} V_{\mathrm{dc}}(k) & V_{\mathrm{dc}}(k) & V_{\mathrm{dc}}(k) \end{bmatrix}^{\mathrm{T}}.$$

T_{s} is the control period. k means the current sampling instant, and $k+1$ represents the next moment. It can be seen from (2.7) that the ac-side currents and circulating currents at the next moment $k+1$ can be predicted with the system inputs (insertion indices) and the measured state variables at the current sampling instant k.

2.3.1.2 Power analysis and arm energy control based on the per-phase model

The power flowing into the upper arm and lower arm in phase x can be expressed as

$$P_{\mathrm{u}x} = v_{\mathrm{u}x}i_{\mathrm{u}x},\ P_{\mathrm{l}x} = v_{\mathrm{l}x}i_{\mathrm{l}x}. \tag{2.8}$$

According to (2.2) and (2.3), the upper arm current and lower arm current in phase x can be written as

$$\begin{aligned} i_{\mathrm{u}x} &= \frac{i_{\mathrm{s}x}}{2} + i_{\mathrm{cir}x}, \\ i_{\mathrm{l}x} &= -\frac{i_{\mathrm{s}x}}{2} + i_{\mathrm{cir}x}. \end{aligned} \tag{2.9}$$

Similarly, based on (2.5) and (2.9), the upper arm voltage and lower arm voltage can be expressed as

$$\begin{aligned} v_{\mathrm{u}x} &= \frac{V_{\mathrm{dc}}}{2} - v_{\mathrm{s}x} - v_{\mathrm{cir}x}, \\ v_{\mathrm{l}x} &= \frac{V_{\mathrm{dc}}}{2} + v_{\mathrm{s}x} - v_{\mathrm{cir}x}. \end{aligned} \tag{2.10}$$

where $v_{\mathrm{s}x} = (L_{\mathrm{s}} + \frac{L}{2})\frac{\mathrm{d}i_{\mathrm{s}x}}{\mathrm{d}t} + R_{\mathrm{s}}i_{\mathrm{s}x}$ and $v_{\mathrm{cir}x} = L\frac{\mathrm{d}i_{\mathrm{cir}x}}{\mathrm{d}t}$. It can be seen that $v_{\mathrm{s}x}$ is the voltage imposed on the equivalent load and it only has the fundamental frequency component in a steady state. $v_{\mathrm{cir}x}$ can be used to control the circulating current $i_{\mathrm{cir}x}$.

According to (2.8), (2.9) and (2.10), the power flowing into phase x (P_x^{Σ}) and the differential power, the difference between the power flowing into the upper and lower arms in the same phase x (P_x^{Δ}), can be obtained as

$$P_x^{\Sigma} = V_{\mathrm{dc}}i_{\mathrm{cir}x} - v_{\mathrm{sx}}i_{\mathrm{s}x} - 2v_{\mathrm{cir}x}i_{\mathrm{cir}x}. \tag{2.11}$$

$$P_x^{\Delta} = \frac{V_{\mathrm{dc}}i_{\mathrm{s}x}}{2} - 2v_{\mathrm{s}x}i_{\mathrm{cir}x} - v_{\mathrm{cir}x}i_{\mathrm{cir}x}. \tag{2.12}$$

It can be seen from the first term in (2.11) that the sum of the power flowing into the upper and lower arms can be regulated by the circulating current with a dc component. This dc component can be drawn from the infinite dc link to charge or discharge the whole energy in phase x. In (2.12), the differential power between the upper arm and lower arm can be controlled by the circulating current with a fundamental frequency component. It means that this fundamental frequency component can redistribute the energy between the upper and lower arms. It should be noted that the first term on the right-hand side of (2.12) cannot accumulate energy in a

fundamental period but it will lead to a large energy variation when the MMC operates at a low frequency.

In the steady state, both P_x^{Σ} and P_x^{Δ} should not have dc components and the steady-state circulating current can be expressed as

$$i_{\mathrm{cir}x,\mathrm{dc}} = \frac{v_{\mathrm{s}x} i_{\mathrm{s}x}|_{\mathrm{dc}}}{V_{\mathrm{dc}}} = \frac{\sum\limits_{x=a,b,c} v_{\mathrm{s}x} i_{\mathrm{s}x}}{3V_{\mathrm{dc}}}. \tag{2.13}$$

Based on the aforementioned power analysis, the arm energy controllers can be designed and the control blocks are shown in Fig 2.3 and Fig. 2.4.

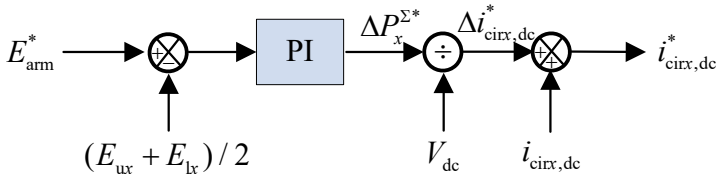

Figure 2.3: The total energy of the upper arm and lower arm in phase x.

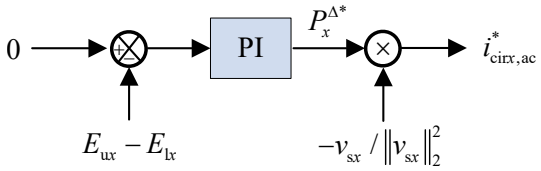

Figure 2.4: The differential energy between the upper arm and lower arm in phase x.

At last, the reference of the circulating current in phase x can be obtained as

$$i^*_{\mathrm{cir}x} = i^*_{\mathrm{cir}x,\mathrm{dc}} + i^*_{\mathrm{cir}x,\mathrm{ac}} \tag{2.14}$$

2.3.1.3 Benefits and drawbacks of the per-phase model

With the per-phase model, each phase of MMC can be controlled independently, which can obviously simplify the control design process. Besides, this modeling approach can be easily extended to the multiple-phase MMC. Also, when such a model is applied in the FCS-MPC scheme, the computational burden will be reduced significantly.

However, as the per-phase model neglects the common-mode voltage v_{NO}, the total harmonic distortion (THD) of the ac current will increase slightly when the FCS-MPC method has been applied. It is worth mentioning that when the modulation method has been used, this phenomenon will not happen. This is because, in the modulation-based control approach, the common-mode voltage has been considered in each control period. Moreover, the reference voltage can be synthesized in each control cycle without steady-state error. Instead, FCS-MPC generates discrete values in each control period, which means that the reference voltage cannot be perfectly tracked and the common-mode voltage cannot be guaranteed to be zero in each control cycle. Therefore, the control performance of FCS-MPC based on the per-phase model

will deteriorate without considering the effect of common-mode voltage. Moreover, the per-phase model cannot completely decouple the dc-link current and the circulating current, which means that the dc-link current/voltage cannot be controlled directly. At last, with the per-phase model, it is difficult to achieve the decoupled control for the MMC system, in which the MMC is regarded as a buffer between the ac side and the dc side. In other words, FCS-MPC needs a more accurate model of the MMC.

2.3.2 Three-phase model of MMC and its power analysis

2.3.2.1 Three-phase model of the MMC

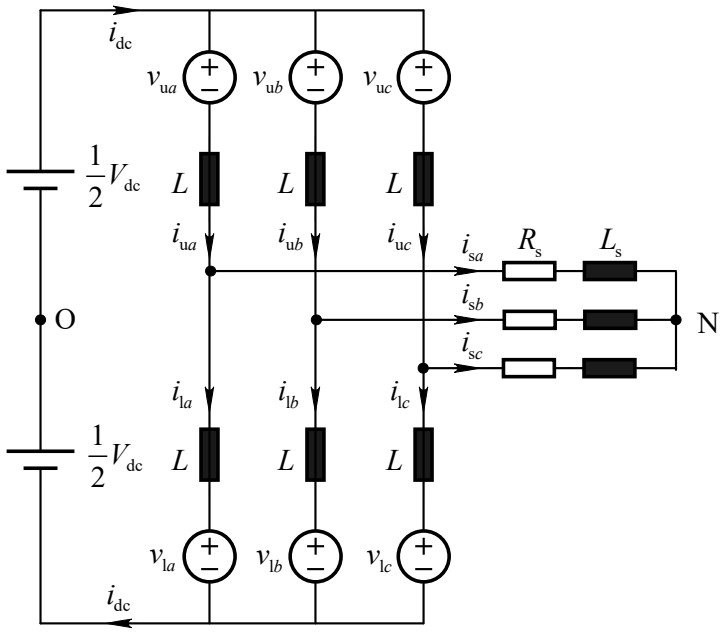

Figure 2.5: Three-phase equivalent circuit of the MMC.

The three-phase equivalent circuit of the MMC is shown in Fig. 2.5. Unlike the definition of current components in the per-phase modeling method, in the three-phase model, the control variables concerning the current can be divided into three parts: ac-side currents, dc-link current, and circulating currents. The ac-side currents can be obtained with

$$i_{sx} = i_{ux} - i_{lx},\ x = a, b, c. \tag{2.15}$$

The dc-link current is given by

$$i_{dc} = \sum_{x=a,b,c} i_{ux} = \sum_{x=a,b,c} i_{lx}. \tag{2.16}$$

The circulating currents are defined as

$$i_{zx} = \frac{i_{ux} + i_{lx}}{2} - \frac{i_{dc}}{3},\ x = a, b, c. \tag{2.17}$$

It is worth noting that the definition of the circulating current in the three-phase model is different from that in the per-phase model. Under this definition, the sum of circulating currents is zero. It means that the circulating currents flow only among the three legs of the converter without being leaked to either the ac side or the dc side.

According to Kirchhoff's voltage law, the upper and lower arm voltages with respect to the midpoint of the dc link can be obtained as

$$\begin{aligned}\frac{V_{\mathrm{dc}}}{2} &= v_{\mathrm{u}x} + L\frac{\mathrm{d}i_{\mathrm{u}x}}{\mathrm{d}t} + R_{\mathrm{s}}i_{\mathrm{s}x} + L_{\mathrm{s}}\frac{\mathrm{d}i_{\mathrm{s}x}}{\mathrm{d}t} + v_{\mathrm{NO}},\\ \frac{V_{\mathrm{dc}}}{2} &= v_{\mathrm{l}x} + L\frac{\mathrm{d}i_{\mathrm{l}x}}{\mathrm{d}t} - R_{\mathrm{s}}i_{\mathrm{s}x} - L_{\mathrm{s}}\frac{\mathrm{d}i_{\mathrm{s}x}}{\mathrm{d}t} - v_{\mathrm{NO}}.\end{aligned} \tag{2.18}$$

Based on (2.15)-(2.18), the dynamics of three-phase ac-side currents, circulating currents, and dc-link current can be derived as

$$\begin{aligned}\frac{\mathrm{d}\boldsymbol{i}_{\mathrm{s}x}}{\mathrm{d}t} &= \frac{1}{2L_{\mathrm{s}}+L}\left(\boldsymbol{v}_{\mathrm{l}x} - \boldsymbol{v}_{\mathrm{u}x} - 2\boldsymbol{v}_{\mathrm{NO}} - 2R_{\mathrm{s}}\boldsymbol{i}_{\mathrm{s}x}\right),\\ \frac{\mathrm{d}\boldsymbol{i}_{\mathrm{z}x}}{\mathrm{d}t} &= \frac{1}{2L}\left(\boldsymbol{v}_{\mathrm{sum}} - \boldsymbol{v}_{\mathrm{l}x} - \boldsymbol{v}_{\mathrm{u}x}\right),\\ \frac{\mathrm{d}i_{\mathrm{dc}}}{\mathrm{d}t} &= \frac{3}{2L}\left(V_{\mathrm{dc}} - v_{\mathrm{sum}}\right),\end{aligned} \tag{2.19}$$

where

$$\boldsymbol{i}_{\mathrm{s}x} = \begin{bmatrix} i_{\mathrm{s}a}\\ i_{\mathrm{s}b}\\ i_{\mathrm{s}c}\end{bmatrix},\quad \boldsymbol{v}_{\mathrm{l}x} = \begin{bmatrix} v_{\mathrm{l}a}\\ v_{\mathrm{l}b}\\ v_{\mathrm{l}c}\end{bmatrix},\quad \boldsymbol{v}_{\mathrm{u}x} = \begin{bmatrix} v_{\mathrm{u}a}\\ v_{\mathrm{u}b}\\ v_{\mathrm{u}c}\end{bmatrix}, \boldsymbol{i}_{\mathrm{z}x} = \begin{bmatrix} i_{\mathrm{z}a}\\ i_{\mathrm{z}b}\\ i_{\mathrm{z}c}\end{bmatrix},$$

$$\boldsymbol{v}_{\mathrm{NO}} = \begin{bmatrix} v_{\mathrm{NO}}\\ v_{\mathrm{NO}}\\ v_{\mathrm{NO}}\end{bmatrix},\quad \boldsymbol{v}_{\mathrm{sum}} = \begin{bmatrix} v_{\mathrm{sum}}\\ v_{\mathrm{sum}}\\ v_{\mathrm{sum}}\end{bmatrix},\quad \begin{aligned} v_{\mathrm{NO}} &= \tfrac{1}{6}\sum_{x=a,b,c}(v_{\mathrm{l}x} - v_{\mathrm{u}x}),\\ v_{\mathrm{sum}} &= \tfrac{1}{3}\sum_{x=a,b,c}(v_{\mathrm{l}x} + v_{\mathrm{u}x}).\end{aligned}$$

It should be noted that v_{NO} is the common mode voltage and represents the voltage potential between the neutral point "N" and dc bus virtual midpoint "O". v_{sum} is the equivalent dc-link output voltage of the MMC and it can be used to control the dc-link current/voltage. The expression of the arm voltages ($v_{\mathrm{u}x}$ and $v_{\mathrm{l}x}$) can be found in (2.6).

As the MPC method is applied to control MMCs in this work, the three-phase discrete-time model of the MMC system has been given. By using the forward Euler method for (2.19), the discrete-time domain mathematical model can be obtained as

$$\begin{aligned}\boldsymbol{i}_{\mathrm{s}x}(k+1) &= \alpha_1\boldsymbol{i}_{\mathrm{s}x}(k) + \alpha_2\left(\boldsymbol{v}_{\mathrm{l}x}(k) - \boldsymbol{v}_{\mathrm{u}x}(k) - 2\boldsymbol{v}_{\mathrm{NO}}(k)\right)\\ \boldsymbol{i}_{\mathrm{z}x}(k+1) &= \boldsymbol{i}_{\mathrm{z}x}(k) + \alpha_3\left(\boldsymbol{v}_{\mathrm{sum}}(k) - \boldsymbol{v}_{\mathrm{l}x}(k) - \boldsymbol{v}_{\mathrm{u}x}(k)\right)\\ i_{\mathrm{dc}}(k+1) &= i_{\mathrm{dc}}(k) + 3\alpha_3\left(V_{\mathrm{dc}} - v_{\mathrm{sum}}(k)\right),\end{aligned} \tag{2.20}$$

where

$$\alpha_1 = 1 - \frac{2R_{\mathrm{s}}T_{\mathrm{s}}}{2L_s+L}, \alpha_2 = \frac{T_{\mathrm{s}}}{2L_s+L}, \alpha_3 = \frac{T_{\mathrm{s}}}{2L},$$

$$\boldsymbol{v}_{\mathrm{u}x}(k) = \begin{bmatrix} n_{\mathrm{u}a}\bar{v}_{\mathrm{u}a} & n_{\mathrm{u}b}\bar{v}_{\mathrm{u}b} & n_{\mathrm{u}c}\bar{v}_{\mathrm{u}c}\end{bmatrix}^{\mathrm{T}},$$

$$\begin{aligned}
\boldsymbol{v}_{\mathrm{l}x}(k) &= \begin{bmatrix} n_{\mathrm{l}a}\bar{v}_{\mathrm{l}a} & n_{\mathrm{l}b}\bar{v}_{\mathrm{l}b} & n_{\mathrm{l}c}\bar{v}_{\mathrm{l}c} \end{bmatrix}^{\mathrm{T}}, \\
v_{\mathrm{sum}}(k) &= \frac{1}{3}\begin{bmatrix} 1 & 1 & 1 \end{bmatrix}(\boldsymbol{v}_{\mathrm{l}x}(k) + \boldsymbol{v}_{\mathrm{u}x}(k)), \\
v_{\mathrm{NO}}(k) &= \frac{1}{6}\begin{bmatrix} 1 & 1 & 1 \end{bmatrix}(\boldsymbol{v}_{\mathrm{l}x}(k) - \boldsymbol{v}_{\mathrm{u}x}(k)).
\end{aligned}$$

n_{yx} ($y = u, l$ and $x = a, b, c$) is the insertion indices and $\bar{v}_{yx}$ is the average voltage in arm y of phase x. T_{s} is the control period.

2.3.2.2 Power analysis and arm energy control based on the three-phase model

The power flowing into the upper arm and lower arm in phase x can be expressed as

$$P_{\mathrm{u}x} = v_{\mathrm{u}x} i_{\mathrm{u}x},\ P_{\mathrm{l}x} = v_{\mathrm{l}x} i_{\mathrm{l}x}. \tag{2.21}$$

According to (2.15)-(2.17), the upper arm current and lower arm current in phase x can be written as

$$\begin{aligned}
i_{\mathrm{u}x} &= \frac{i_{\mathrm{s}x}}{2} + i_{\mathrm{z}x} + \frac{i_{\mathrm{dc}}}{3} \\
i_{\mathrm{l}x} &= -\frac{i_{\mathrm{s}x}}{2} + i_{\mathrm{z}x} + \frac{i_{\mathrm{dc}}}{3}.
\end{aligned} \tag{2.22}$$

Similarly, based on (2.18) and (2.22), the upper arm voltage and lower arm voltage can be expressed as

$$\begin{aligned}
v_{\mathrm{u}x} &= \frac{V_{\mathrm{dc}}}{2} - v_{x\mathrm{N}} - v_{\mathrm{NO}} - v_{\mathrm{z}x} - \frac{L}{3}\frac{\mathrm{d}i_{\mathrm{dc}}}{\mathrm{d}t} \\
v_{\mathrm{l}x} &= \frac{V_{\mathrm{dc}}}{2} + v_{x\mathrm{N}} + v_{\mathrm{NO}} - v_{\mathrm{z}x} - \frac{L}{3}\frac{\mathrm{d}i_{\mathrm{dc}}}{\mathrm{d}t},
\end{aligned} \tag{2.23}$$

where $v_{x\mathrm{N}} = (L_{\mathrm{s}} + \frac{L}{2})\frac{\mathrm{d}i_{\mathrm{s}x}}{\mathrm{d}t} + R_{\mathrm{s}} i_{\mathrm{s}x}$ and $v_{\mathrm{z}x} = L\frac{\mathrm{d}i_{\mathrm{z}x}}{\mathrm{d}t}$. It can be seen that $v_{x\mathrm{N}}$ is the voltage imposed on the equivalent load and it only has the fundamental frequency component in a steady state. $v_{\mathrm{z}x}$ can be used to control the circulating current $i_{\mathrm{z}x}$. In motor control applications, the inductance of the arm inductor L is usually small. Besides, $\frac{\mathrm{d}i_{\mathrm{dc}}}{\mathrm{d}t}$ is small in steady state. Therefore, the term $\frac{L}{3}\frac{\mathrm{d}i_{\mathrm{dc}}}{\mathrm{d}t}$ in (2.23) can be neglected. The arm voltages can be approximately written as

$$\begin{aligned}
v_{\mathrm{u}x} &\approx \frac{V_{\mathrm{dc}}}{2} - v_{x\mathrm{N}} - v_{\mathrm{NO}} - v_{\mathrm{z}x}, \\
v_{\mathrm{l}x} &\approx \frac{V_{\mathrm{dc}}}{2} + v_{x\mathrm{N}} + v_{\mathrm{NO}} - v_{\mathrm{z}x}.
\end{aligned} \tag{2.24}$$

According to (2.21), (2.22) and (2.24), the power flowing into phase x (P_x^{Σ}) and the difference of the power flowing into the upper arm and lower arm in the same phase x (P_x^{Δ}) can be obtained as

$$\begin{aligned}
P_x^{\Sigma} \approx& \frac{V_{\mathrm{dc}} i_{\mathrm{dc}}}{3} - v_{x\mathrm{N}} i_{\mathrm{s}x} - v_{\mathrm{NO}} i_{\mathrm{s}x} \\
&- \frac{2}{3} v_{\mathrm{z}x} i_{\mathrm{dc}} - 2 v_{\mathrm{z}x} i_{\mathrm{z}x} + V_{\mathrm{dc}} i_{\mathrm{z}x},
\end{aligned} \tag{2.25}$$

$$\begin{aligned}
P_x^{\Delta} \approx& \frac{V_{\mathrm{dc}} i_{\mathrm{s}x}}{2} - v_{\mathrm{z}x} i_{\mathrm{s}x} - \frac{2}{3} v_{x\mathrm{N}} i_{\mathrm{dc}} \\
&- \frac{2}{3} v_{\mathrm{NO}} i_{\mathrm{dc}} - 2 v_{x\mathrm{N}} i_{\mathrm{z}x} - 2 v_{\mathrm{NO}} i_{\mathrm{z}x}.
\end{aligned} \tag{2.26}$$

The first two terms on the right-hand side of (2.25) will be balanced in a steady state, which means the energy will not be accumulated by these two terms in a fundamental period. The last term of (2.25) also indicates that the circulating current i_{zx} can be used to control the energy in phase x when i_{zx} has the dc component. In fact, the dc component in the circulating currents can be used to transfer energy between three phases of the MMC.

It can be seen that the first term on the right-hand side of (2.26) contributes the most significant differential power between the upper and lower arms. As the energy is integral to the instantaneous power, this term will lead to a large energy variation when the MMC operates at a low frequency. Therefore, it is necessary to compensate for this term in (2.26) at low frequency. The last two terms in (2.26) can be used to regulate the differential power. For example, if the circulating current i_{zx} has a fundamental component, the integral of $v_{x\mathrm{N}}i_{zx}$ will be used to balance the energy. However, in motor drive applications, $v_{x\mathrm{N}}$ will be small at low speed. Besides, the energy response caused by $v_{x\mathrm{N}}i_{zx}$ is slow due to the long fundamental period. Therefore, its capability of energy balancing at low speed is limited. The term $v_{\mathrm{NO}}i_{zx}$ is usually used to balance the energy between the upper and lower arms at low-speed conditions. Actually, if the sign of (2.26) can be controlled, the differential energy between the upper and lower arms can be regulated. For example, when the energy of the upper arm $E_{\mathrm{u}x}$ is greater than the energy of the lower arm $E_{\mathrm{l}x}$, the instantaneous power of (2.26) should be less than 0 so that the energy of the lower arm increases faster or decreases slower than that of the upper arm and can catch up the energy of the upper arm at last, that is, in case $E_{\mathrm{u}x} - E_{\mathrm{l}x} > 0$, $P_x^{\Delta} < 0$.

Based on (2.25), the total power flowing into the MMC can be obtained as

$$P_{\mathrm{total}}^{\Sigma} = \sum_{x=a,b,c} P_x^{\Sigma} \approx V_{\mathrm{dc}} i_{\mathrm{dc}} - \sum_{x=a,b,c} v_{x\mathrm{N}} i_{\mathrm{s}x} - \sum_{x=a,b,c} 2 v_{\mathrm{z}x} i_{\mathrm{z}x}. \tag{2.27}$$

According to (2.27), we can find that the difference between the power flowing from the dc side and the power flowing into the ac side will increase or decrease the total energy of the MMC. It means that the total energy of the MMC can be controlled by dc-side current i_{dc} when MMC operates in the inverter mode or the ac-side active power $\sum_{x=a,b,c} v_{x\mathrm{N}} i_{\mathrm{s}x}$ when the MMC operates in the rectifier mode. The last term on the right-hand side of (2.27) can be regarded as the disturbance.

Similarly, according to (2.26), the common differential power of three phases can be derived as

$$P_{\mathrm{com}}^{\Delta} = \sum_{x=a,b,c} P_x^{\Delta} \approx -2 v_{\mathrm{NO}} i_{\mathrm{dc}} - \sum_{x=a,b,c} (v_{x\mathrm{N}} i_{\mathrm{z}x} + 2 v_{\mathrm{z}x} i_{\mathrm{s}x}). \tag{2.28}$$

The common differential power $P_{\mathrm{com}}^{\Delta}$ can be used to eliminate the overall errors between the upper and lower arm energy of the whole three phases. From (2.28), we can find that $P_{\mathrm{com}}^{\Delta}$ can be controlled by injecting positive sequence circulating currents or a dc component in common-mode voltage.

According to the power analysis mentioned above, the energy balancing control will be achieved by adjusting these power components (P_x^{Σ}, P_x^{Δ}, $P_{\mathrm{total}}^{\Sigma}$ and $P_{\mathrm{com}}^{\Delta}$) properly.

Considering MMC-based HVDC applications, a useful arm energy control strategy will be introduced in the following part briefly [27].

From (2.27), it can be seen that the difference between the power flowing into the dc link and the power flowing into the ac side will charge or discharge the whole capacitors of the MMC

(neglecting the arm inductor). The control block diagram of the total capacitor energy control is shown in Fig. 2.6 and Fig. 2.7, respectively.

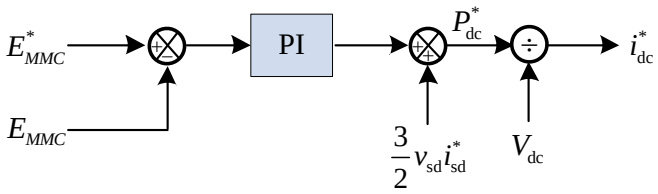

Figure 2.6: Control block diagram of the total energy controller when MMC operates in the inverter mode.

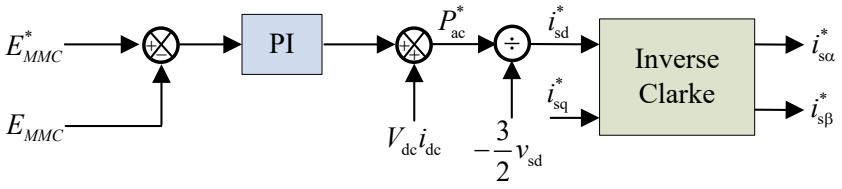

Figure 2.7: Control block diagram of the total energy controller when MMC operates in the rectifier mode.

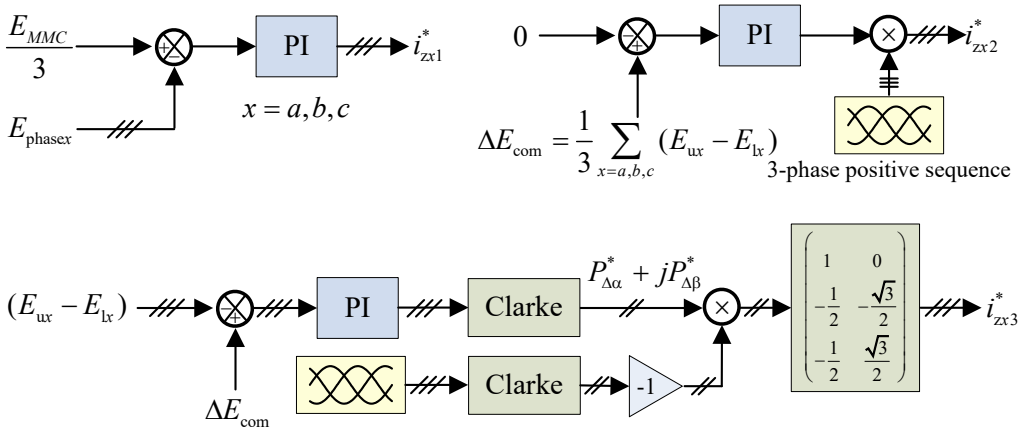

Figure 2.8: Block diagram of the internal energy controller.

For the decoupled control, the balance of three-phase energy and the balance between the upper and lower arm energy should neither affect ac-side active power nor dc-link current. As we know, the circulating currents only flow among the three phases of MMC without being leaked to either the ac side or the dc side. Therefore, the circulating currents can be used to transfer energy between different phases and different arms. The control block diagram of the internal energy balancing is shown in Fig. 2.8.

2.4 Conventional MPC scheme for MMC

The MPC schemes for the MMC can be divided into two groups in the initial stage: direct model predictive control (DMPC) and indirect model predictive control (IMPC) as discussed in Section 1.2. In the DMPC method, all the control objectives can be achieved by using a cost function. However, this method is difficult to realize in real time due to its heavy computational burden. The IMPC method removes the control of SM capacitor voltages from the cost function. Instead, it employs an external voltage sorting algorithm to guarantee the SM balancing control. In this way, the computational burden has been reduced significantly and the control algorithm can be easily implemented in practice. In this work, the IMPC approach has been applied.

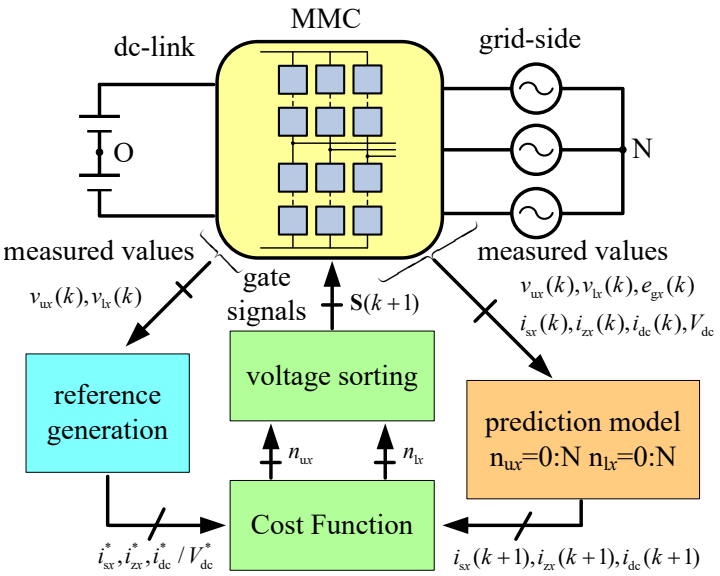

Figure 2.9: Block diagram of the IMPC scheme.

The control block diagram of the IMPC scheme is shown in Fig. 2.9. At first, the MPC scheme uses the discrete-time model, which is also called the prediction model, to obtain the predictive values of the control variables at $k+1$ time instant for all the possible control options. The control option here refers to a combination of insertion indices for all the arms. After that, a proper cost function is evaluated for these predictive values. The optimal control option, which minimizes the cost function, will be selected. Next, the sorting algorithm reads these selected insertion indices and determines which SMs to insert or bypass in each arm. At last, the gate signals from the sorting algorithm are then applied to the MMC.

As it can be seen that the IMPC requires a discrete-time model of the MMC system, which has been given in Section 2.3. Based on the different mathematical models of MMC, the IMPC scheme can be categorized into two groups naturally: per-phase model based MPC and three-phase model based MPC. The design procedure and control method of per-phase MPC and three-phase MPC will be introduced in the following sections.

2.4.1 Per-phase model based MPC scheme

In this method, the per-phase model has been used as the prediction model to implement the algorithm. Besides, as it has been illustrated in Section 2.3.1, each phase of the MMC can be controlled independently by using the predictive controller. Therefore, a total of three predictive controllers will be employed to achieve all the control targets for the three-phase MMC. In each predictive controller, two control objectives, i.e. ac-side current and circulating current, should be controlled at the same time while the arm energy can be achieved indirectly by controlling the circulating current.

From (2.7), it can be seen that different predictive values of control variables can be obtained based on different combinations of the insertion indices ($n_{\mathrm{u}x}$ and $n_{\mathrm{l}x}$). Both of $n_{\mathrm{u}x}$ and $n_{\mathrm{l}x}$ have discrete values ranging from 0 to N. Therefore, a total of $(N+1)^2$ combinations will be introduced into the prediction model and generate $(N+1)^2$ predictive values. The cost function is used to evaluate these predictive values and it is defined as

$$J = \|i^*_{\mathrm{s}x} - i_{\mathrm{s}x}(k+1)\|_2^2 + w_1 \|i^*_{\mathrm{cir}x} - i_{\mathrm{cir}x}(k+1)\|_2^2 , \tag{2.29}$$

where w_1 is the weighting factor. In this work, the trial and error method is applied to determine the w_1. $i^*_{\mathrm{s}x}$ represents the reference of the ac-side output current in phase x. $i^*_{\mathrm{cir}x}$ is the reference of the circulating current in phase x (see (2.14)) and it can be used to regulate the sum energy and differential energy of the upper and lower arms in the same leg x.

After evaluating all the predictive values by using (2.29), the optimal combination of insertion indices can be selected, that is, its corresponding predictive values can minimize the cost function. At last, the selected insertion index for each arm will be transferred to the voltage sorting algorithm. The flowchart of the per-phase model based MPC can be found in Fig. 2.10.

2.4.2 Three-phase model based MPC scheme

Different from the per-phase model based MPC method, the three-phase model based MPC scheme uses a single cost function to achieve all the control objectives. Four control objectives, i.e., ac-side currents, circulating currents, dc-link voltage/current and common-mode voltage, should be regulated at the same time in the predictive controller while the SM capacitor voltage control is achieved by using an external voltage sorting algorithm.

At first, a three-phase discrete-time model of the MMC (see (2.20)) has been employed to predict the future behavior of control variables. It can be seen from the prediction model (2.20) that the predictive value of the ac-side current in phase x is not only related to the ac-side output voltage of phase x itself, it also depends on the ac-side output voltages of the other phases. The same is true for circulating currents, dc-link voltage/current and common-mode voltage. Therefore, in order to obtain all the predictive values of the control variables, a total of $(N+1)^6$ combinations will be introduced into the prediction model. All these predictive values will be evaluated by a cost function. The cost function is defined as follows:

$$J = \|\boldsymbol{i}^*_{\mathrm{s}x} - \boldsymbol{i}_{\mathrm{s}x}(k+1)\|_2^2 + w_1 \|\boldsymbol{i}^*_{\mathrm{z}x} - \boldsymbol{i}_{\mathrm{z}x}(k+1)\|_2^2 + w_2 \|V^*_{\mathrm{dc}} - v_{\mathrm{sum}}\|_2^2 + w_3 \|v^*_{\mathrm{NO}} - v_{\mathrm{NO}}\|_2^2 , \tag{2.30}$$

or

$$\begin{aligned} J = {} & \|\boldsymbol{i}^*_{\mathrm{s}x} - \boldsymbol{i}_{\mathrm{s}x}(k+1)\|_2^2 + w_1 \|\boldsymbol{i}^*_{\mathrm{z}x} - \boldsymbol{i}_{\mathrm{z}x}(k+1)\|_2^2 \\ & + w_2 \|i^*_{\mathrm{dc}} - i_{\mathrm{dc}}(k+1)\|_2^2 + w_3 \|v^*_{\mathrm{NO}} - v_{\mathrm{NO}}\|_2^2 , \end{aligned} \tag{2.31}$$

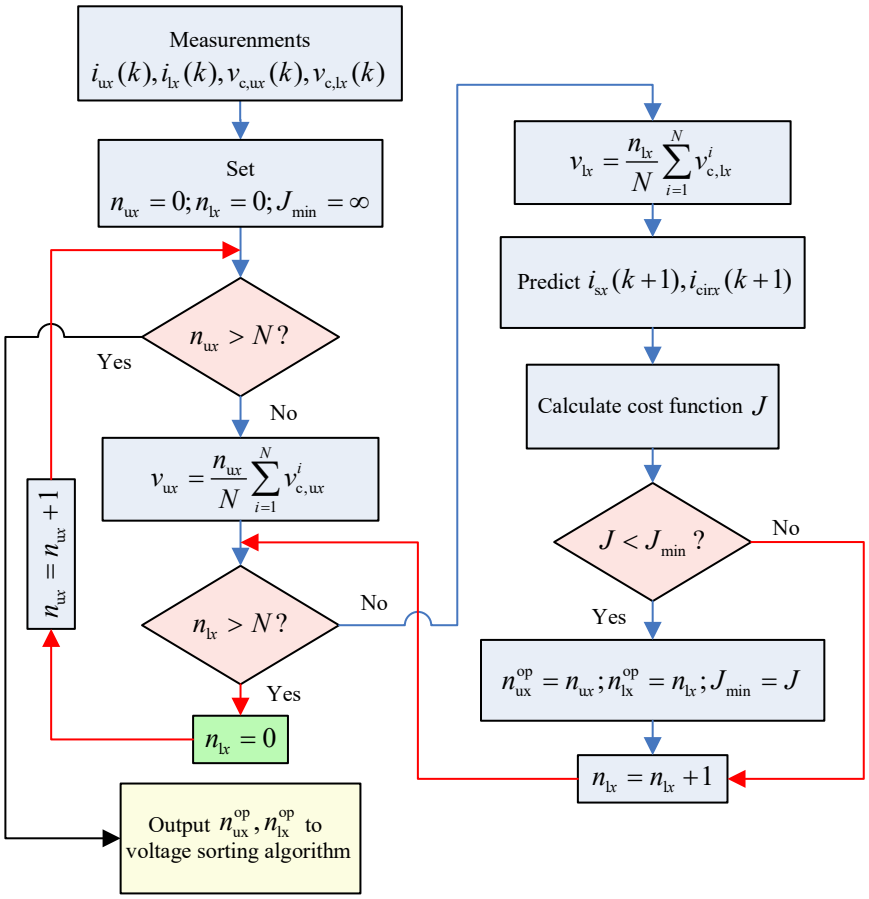

Figure 2.10: Flowchart of the per-phase model based MPC for the MMC.

where $\boldsymbol{i}_{sx}^{*} = \begin{bmatrix} i_{sa}^{*} \\ i_{sb}^{*} \\ i_{sc}^{*} \end{bmatrix}$, $\boldsymbol{i}_{zx}^{*} = \begin{bmatrix} i_{za}^{*} \\ i_{zb}^{*} \\ i_{zc}^{*} \end{bmatrix}$, $\boldsymbol{i}_{sx}(k+1) = \begin{bmatrix} i_{sa}(k+1) \\ i_{sb}(k+1) \\ i_{sc}(k+1) \end{bmatrix}$, $\boldsymbol{i}_{zx}(k+1) = \begin{bmatrix} i_{za}(k+1) \\ i_{zb}(k+1) \\ i_{zc}(k+1) \end{bmatrix}$, $v_{\mathrm{NO}}^{*} = 0$. w_1, w_2 and w_3 are the weighting factors. $\boldsymbol{i}_{zx}^{*}$ represents the reference of the circulating current and it can be obtained from the arm energy controller (see Section 2.3.2.2).

When the MMC operates in the rectifier mode, equation (2.30) will be applied as the cost function. On the other hand, when the MMC operates in the inverter mode, equation (2.31) will be employed. After evaluating all these predictive values, the optimal insertion index for each arm can be determined. The flowchart of the three-phase model based MPC can be found in Fig. 2.11.

It can be seen that for the conventional three-phase model based MPC method, a total $(N+1)^6$ combinations will be evaluated by the cost function. Compared with the per-phase model based MPC method, the computational burden of three-phase model based MPC method is significantly increased. Therefore, it is difficult to implement FCS-MPC in practice without some specific measures. On the other hand, due to the use of a more accurate mathematical model of the MMC, the three-phase model based MPC can achieve a better steady-state performance in terms of lower THD of the ac-side currents. Besides, the ac and dc sides of the MMC can be de-

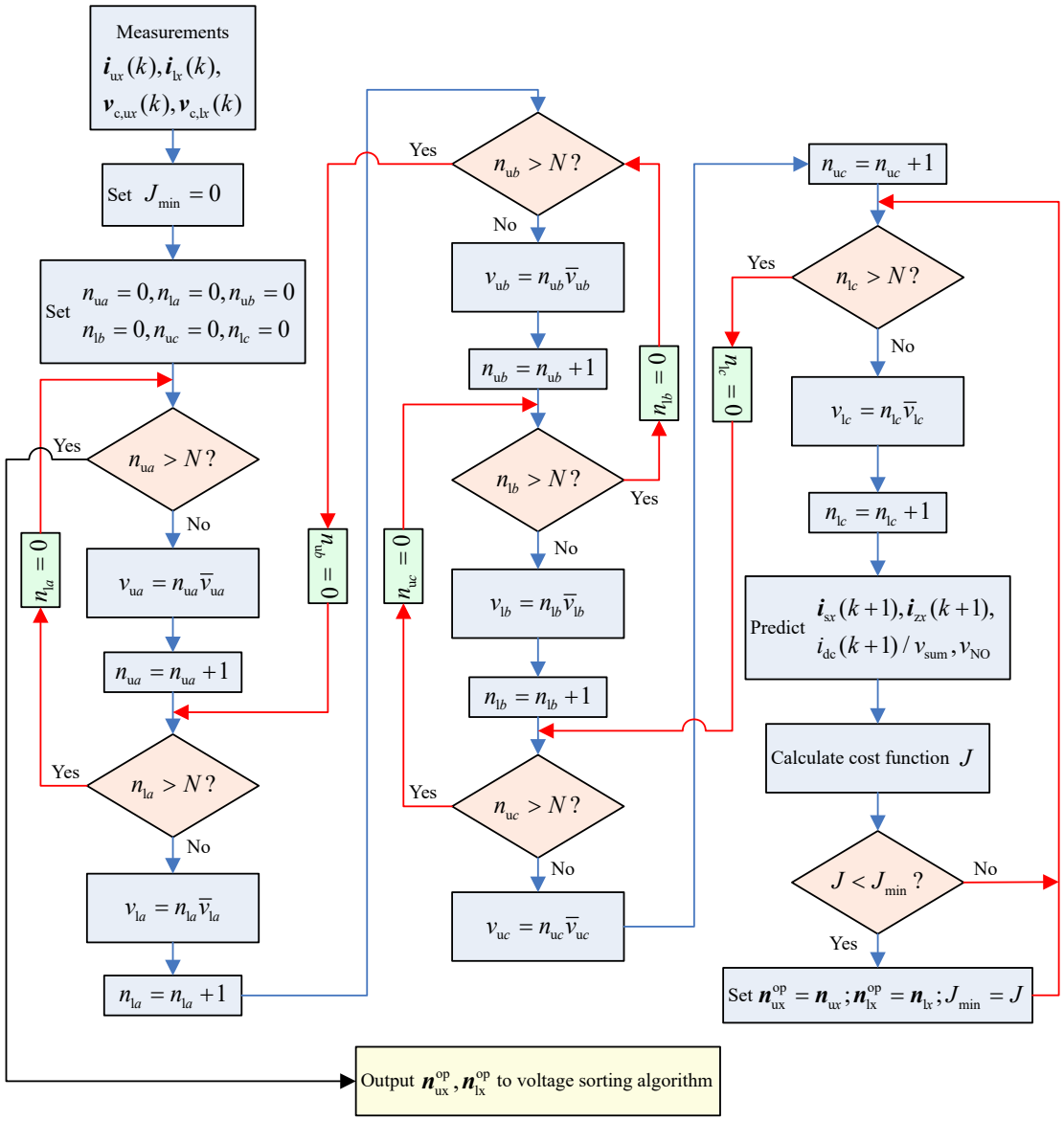

Figure 2.11: Flowchart of the three-phase model based MPC for the MMC.

coupled, and the MMC itself can act as a buffer by using the three-phase model based method. In this way, the control system can achieve a very fast dynamic response, especially for the dc-link voltage. Unfortunately, due to its large computational burden, there is little research on three-phase model based MPC for the MMC system in academia.

2.4.3 Voltage sorting algorithm

In order to generate the final switching signals, the selected insertion indices ($n_{\mathrm{ux}}^{\mathrm{op}}$ or $n_{\mathrm{lx}}^{\mathrm{op}}$) obtained from MPC will be passed to the voltage sorting algorithm. This sorting algorithm will be employed in every arm of the MMC to balance the voltages of SMs in the same arm. Based on the sign of the arm current $i_{\mathrm{u}x}(k)/i_{\mathrm{l}x}(k)$ at current moment k, the algorithm determines which

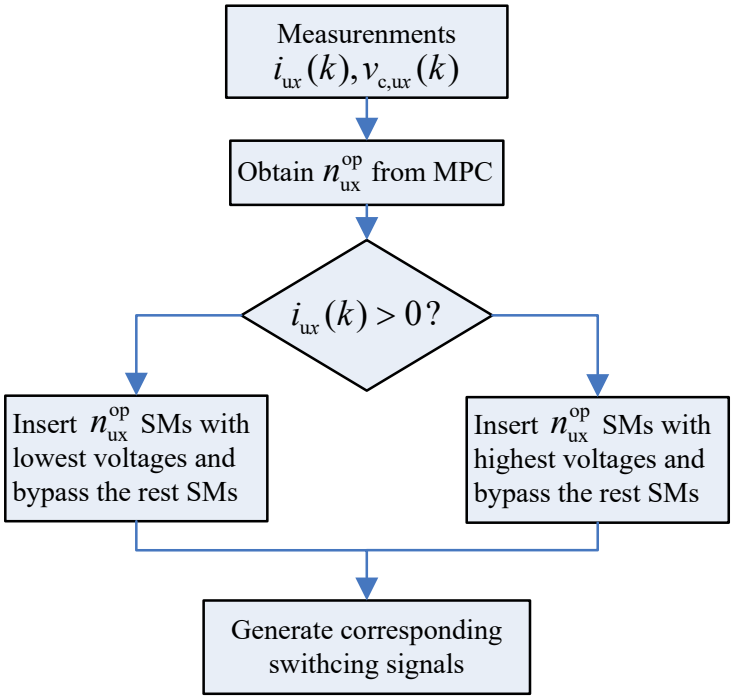

Figure 2.12: Flowchart of the voltage sorting algorithm for the upper arm in phase x.

SMs will be inserted and which SMs need to be bypassed. For example, if $i_{ux}(k) > 0$, this algorithm will insert n_{ux}^{op} SMs with the lowest capacitor voltages in the related arm and bypass the rest SMs. On the other hand, if $i_{ux}(k) < 0$, the algorithm will insert n_{ux}^{op} SMs with the highest capacitor voltages and bypass the other SMs. In this way, the SM balancing control can be achieved. The switching signals will be applied to the MMC at the next sampling instant $k+1$. The flowchart of the voltage sorting algorithm can be found in Fig. 2.12.

2.5 Experimental results of conventional MPC schemes

Table 2.1: Parameters for the experimental platform

Parameter	Symbol	Value
DC-link voltage	V_{dc}	100 V
Number of SMs on each Arm	N	2
SM Capacitance	C_{SM}	5.04 mF
Arm Inductance	L	1.9 mH
AC-side Resistance	R_s	5 Ω
AC-side Inductance	L_s	6.8 mH

A practical three-phase prototype for the MMC has been built as shown in Fig. 2.13 and its parameters are listed in Table 2.1. Both the per-phase model based MPC algorithm and three-phase model based algorithm are implemented on a dSPACE SCALEXIO real-time control system, which consists of a 4-core 3.5-GHz Intel XEON E3V6 processor and a Xilinx Kintex-7

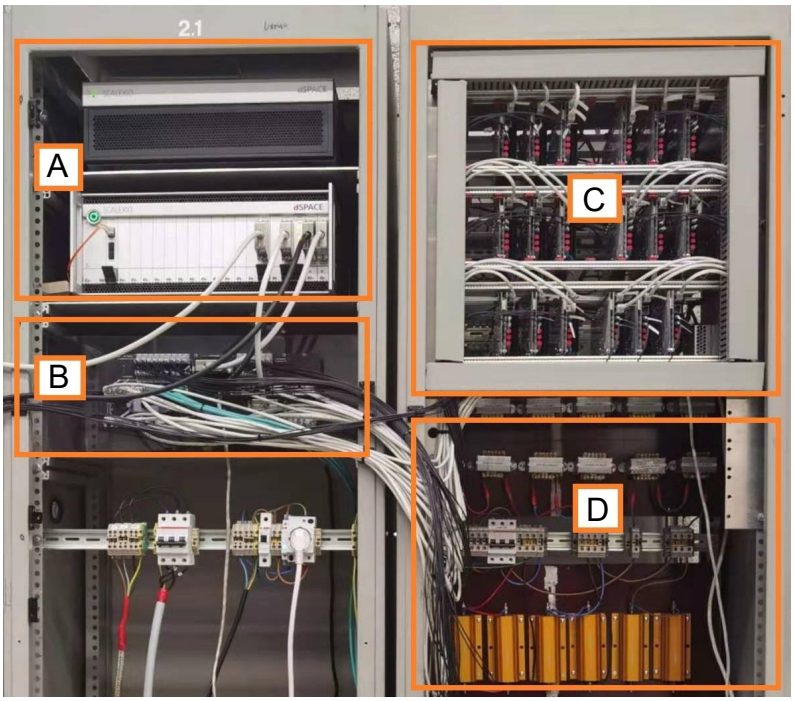

Figure 2.13: Setup of the testbench system. A: dSPACE SCALEXIO real-time control system, B: Interface, C: Three phase MMC with imperix PEH2015 submodule, D: RL load

160T field-programmable gate array (FPGA) chip. The sampling time of these MPC methods is 100 µs.

2.5.1 Experimental results of the per-phase model based MPC scheme

The experimental results of the conventional per-phase model based MPC method under the step change in ac currents at nominal frequency are shown in Fig. 2.14. Fig. 2.14(a) shows the three-phase ac-side currents under this related change. Fig. 2.14(b) shows the circulating current of phase a. It should be noted that in order to compare with the experimental results of the three-phase model based MPC method, the definition of circulating currents here is based on (2.17), which is $i_{za} = i_{cira} - \frac{i_{dc}}{3}$. The capacitor voltages of the upper and lower arm in phase a are shown in Fig. 2.14(c). The ripple magnitude of all the voltages is less than 10% of the reference value. Fig. 2.14(d) shows the dc-link current. It can be seen that the ripple of dc-link current is large. Besides, the dc-link current experience a long time to reach a stable value when the step change occurs. As we have analyzed that the dc-link current cannot be controlled directly by using the per-phase model and thus its steady-state performance and dynamic performance are poor. At last, the upper and lower arm currents are shown in Fig. 2.14(e).

The control performance of the per-phase model based MPC method at different frequencies has also been tested, as shown in Fig. 2.15 and Fig. 2.16. It can be seen that the SM capacitor voltage ripple increases with the decrease of ac current frequency. Fig. 2.15(c) shows that the dc-link current has an obvious ac component when the amplitude of ac currents is $10\,\mathrm{A}$. This phenomenon is even more pronounced when the MMC system operates at $5\,\mathrm{Hz}$. The frequency of this ac component in the dc-link current is three times that of the circulating current. This

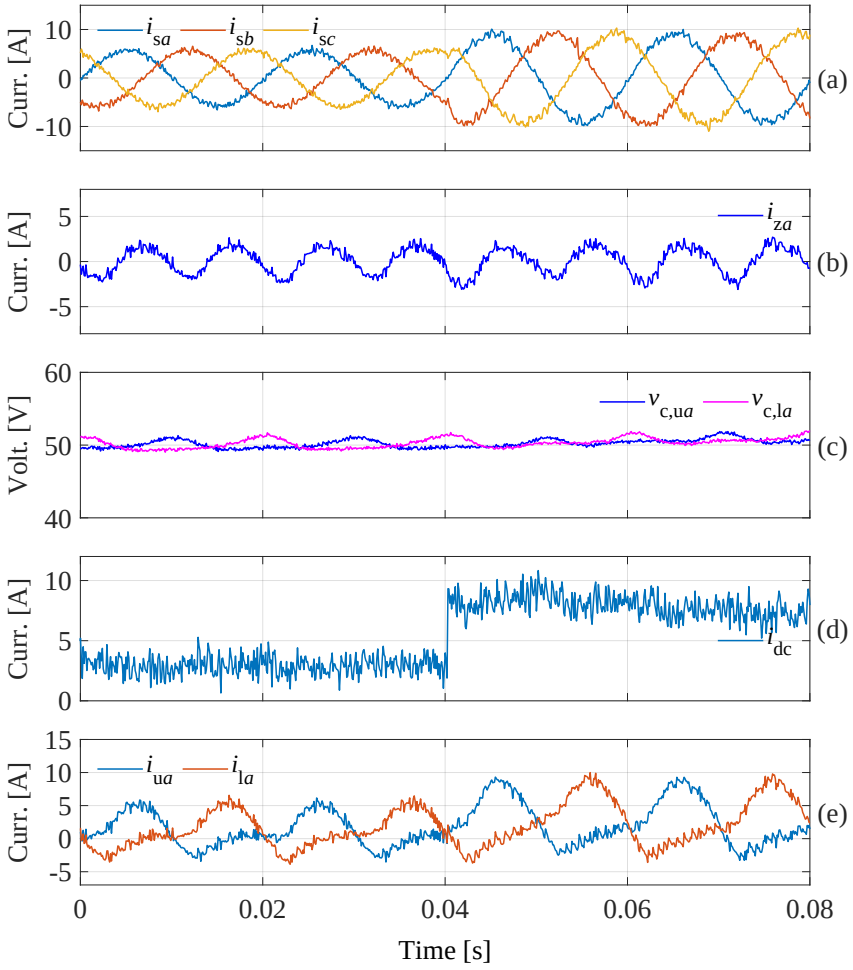

Figure 2.14: Step change in ac currents with per-phase model based MPC at 50 Hz.

means that the ac components in the circulating currents will also be present on the dc link. Although such a per-phase approach can achieve the independent control for each phase of the MMC, but it sacrifices the ability to directly control the dc-link current/voltage and the common-mode voltage. Moreover, the steady-state performance of the ac currents will deteriorate.

2.5.2 Experimental results of the three-phase model based MPC scheme

In order to illustrate the effect of using different models on the ac currents, an ideal experiment has been designed in the simulation. In the simulation, a three-phase MMC system has been constructed on MATLAB/Simulink and its parameters are the same as those used in the experiment (see Table 2.1) except the capacitance C_{SM}. C_{SM} in the simulation has been set to infinity and thus the control objective only has ac-side currents. The simulation results of the ac current i_{sa} by using per-phase model based MPC and three-phase model based MPC are shown in Fig. 2.17. It can be seen that even in this ideal case, the steady-state performance of the ac current i_{sa} is different for these two control methods. The results show that the control performance of three-phase model based MPC is superior to that of per-phase model based MPC.

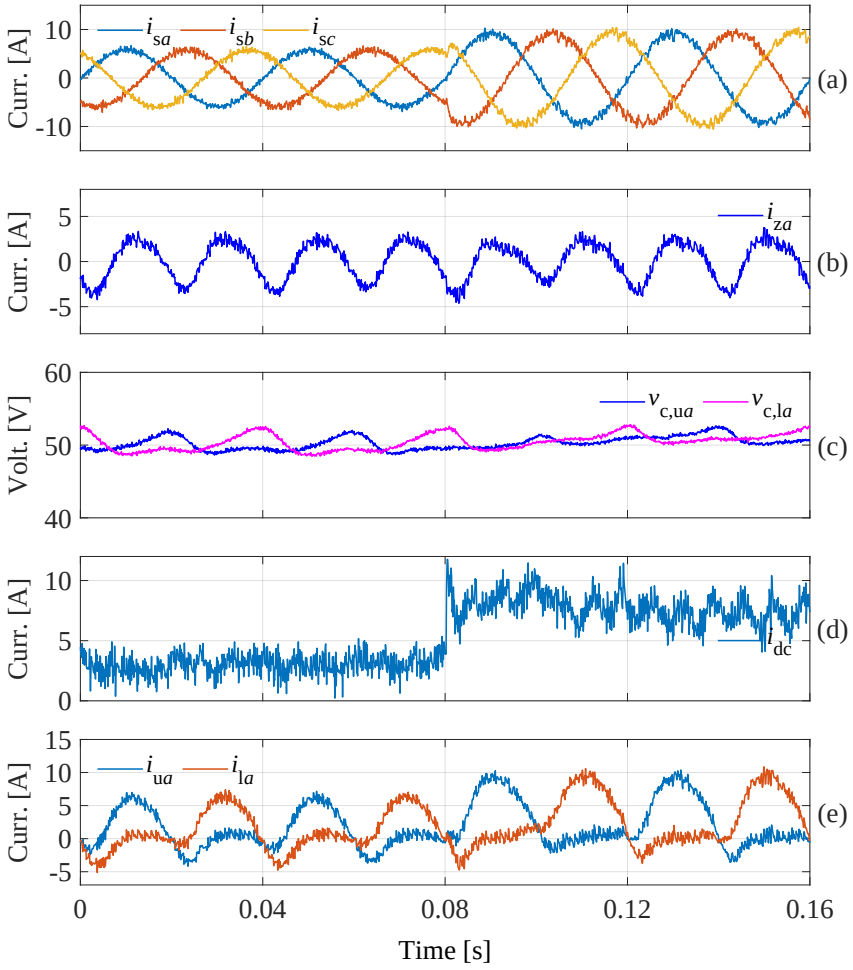

Figure 2.15: Step change in ac currents with per-phase model based MPC at 25 Hz.

These simulation results reveal that using a more accurate MMC model can improve the control performance of ac currents when MPC is applied.

The comparison between per-phase model based MPC and three-phase model based MPC in terms of the transient response of ac currents has been presented in Fig. 2.18. The experimental results show that the three-phase model based MPC method has a fast transient response compared to the per-phase model based MPC method. Besides, ac currents have lesser current ripple with the three-phase model based MPC. Therefore, MPC based on the three-phase model can achieve a better steady-state performance.

The experimental results of the three-phase model based MPC method under the step change in ac currents at nominal frequency are shown in Fig. 2.19. It can be seen that with this method, the dc-link current has less current ripple compared to the per-phase model based MPC. Moreover, when the amplitude of ac currents is 10 A, in which the MMC is operating at high modulation index, the three-phase model based MPC can achieve a better steady-state performance of ac currents (lower THD and smaller current ripple). Also, compared to the per-phase model based method, this three-phase model based method has smaller circulating currents with comparable SM capacitor voltage fluctuations.

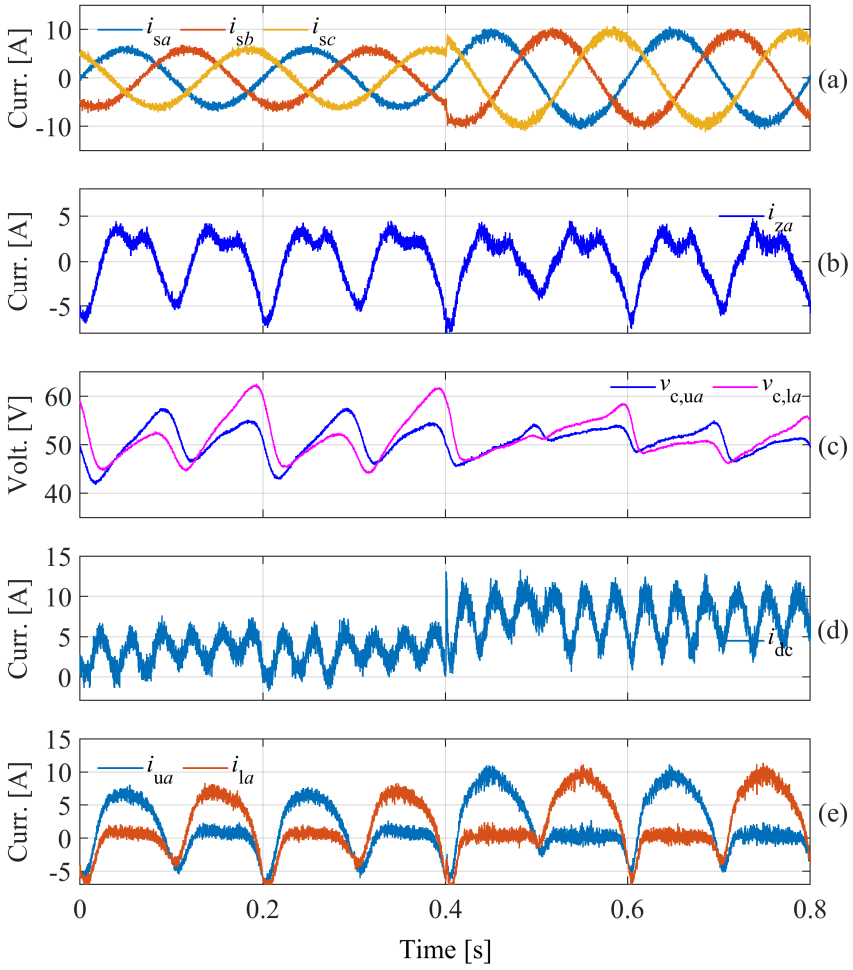

Figure 2.16: Step change in ac currents with per-phase model based MPC at 5 Hz.

Table 2.2: Comparison of THD between per-phase MPC and three-phase MPC

Frequency	Per-phase MPC		Three-phase MPC	
	6 A	10 A	6 A	10 A
50 Hz	4.88%	4.45%	4.24%	3.71%
25 Hz	4.84%	4.50%	4.19%	3.64%
5 Hz	4.99%	4.50%	4.38%	3.71%

The control performance of the three-phase model based MPC method at lower frequencies has been checked, as shown in Fig. 2.20 and Fig. 2.21. Unlike the per-phase method where the dc-link current exhibits large ac component fluctuations at low frequencies, the dc-link current has smaller current ripple and faster dynamic response with the three-phase model based MPC. There is no ac component on the dc side either. In addition, from Fig. 2.21, it can be seen that the three-phase model based MPC can achieve both smaller circulating currents and smaller SM capacitor voltage fluctuations compared to the per-phase method shown in Fig. 2.16. It is also worth noting that the circulating current of both MPC methods has a significant sec-

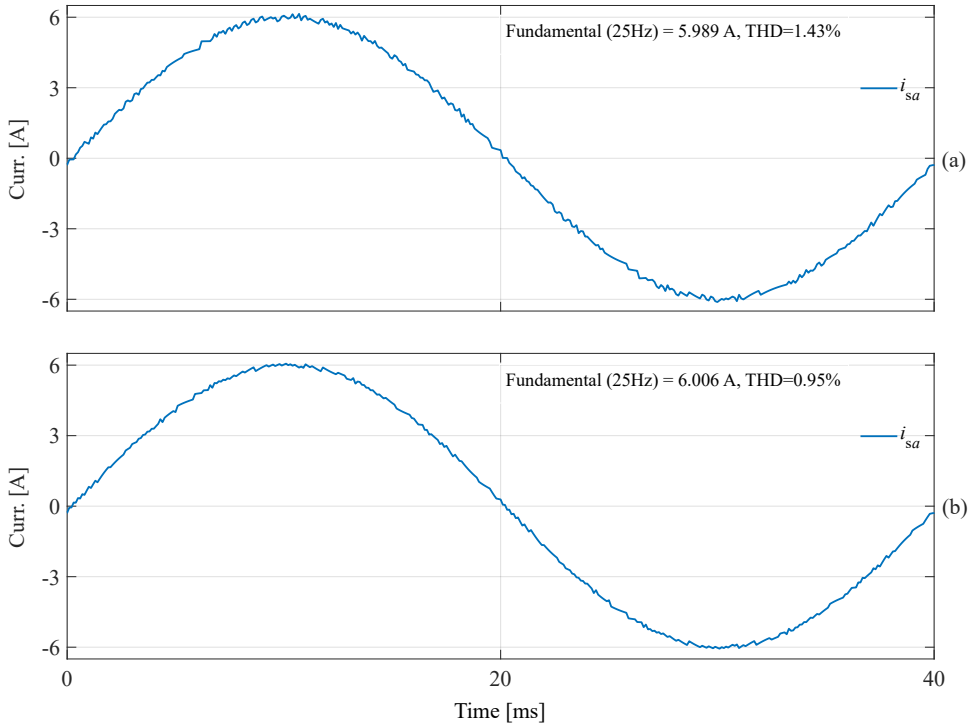

Figure 2.17: Steady-state performance of the ac-side current. (a) Per-phase model based MPC. (b) Three-phase model based MPC.

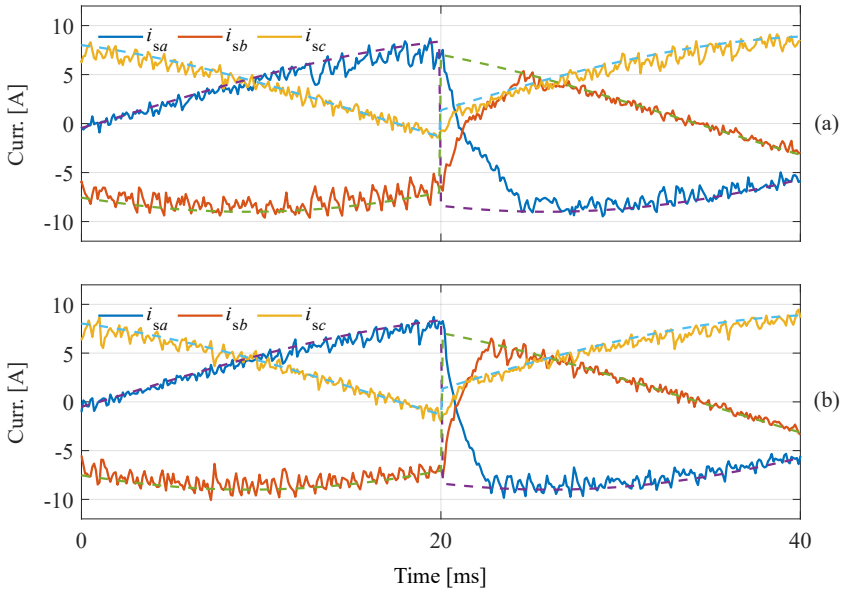

Figure 2.18: Dynamic performance of ac currents. (a) Per-phase model based MPC. (b) Three-phase model based MPC.

ond harmonic component, but in the three-phase method, this second harmonic component is not introduced to the dc-link current. This means that the three-phase model based MPC can

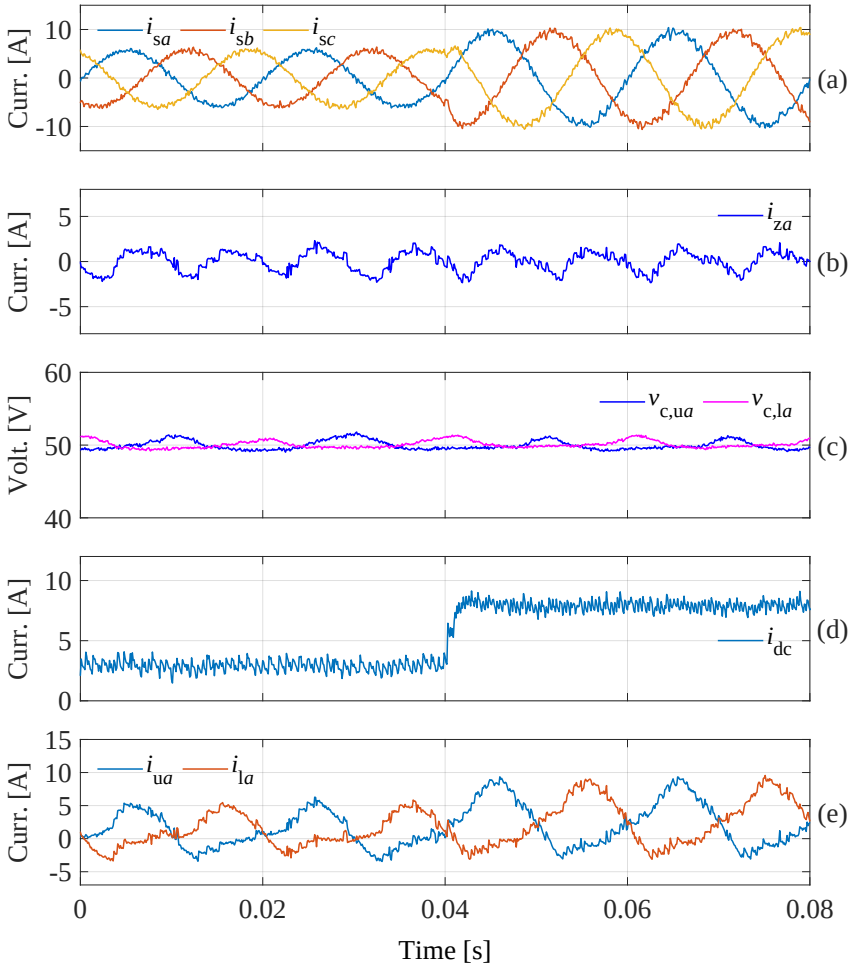

Figure 2.19: Step change in ac currents with per-phase model based MPC at 50 Hz.

fully decouple the ac currents, circulating currents and dc-link current and control these current components independently. The THD for ac currents at different magnitudes and different frequencies has been given in Table 2.2. It can be observed that the three-phase model based MPC has a lower THD compared to the per-phase method. Therefore, it can be concluded that even though the three-phase model based MPC has a higher computational burden, it has better steady-state performance and dynamic response in comparison with per-phase model based MPC.

2.6 Summary

This chapter presents two different mathematical models of the MMC, namely, the per-phase model and the three-phase model. The power analysis based on these two different models has been given, which can be used to analyze the overall energy variation of the MMC, the energy variation from phase to phase, and the energy variation between the upper and lower arms in each phase. Based on the power analysis for each model, different arm-energy control

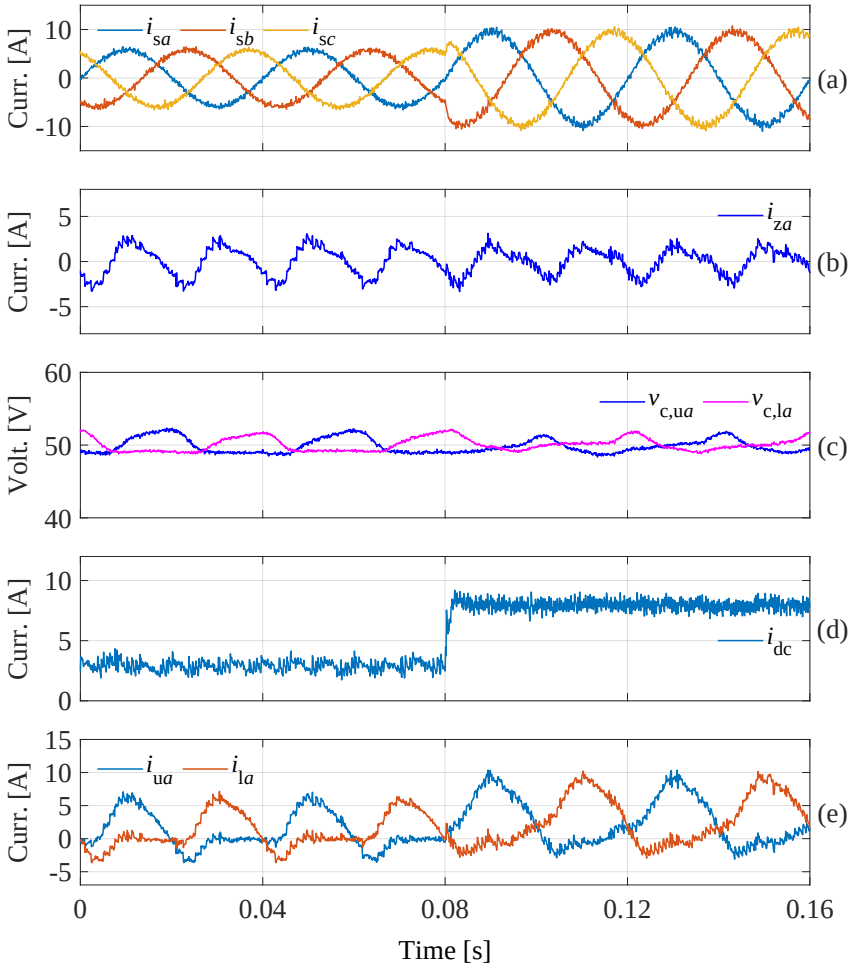

Figure 2.20: Step change in ac currents with per-phase model based MPC at 25 Hz.

approaches can be designed.

Due to the use of different models of the MMC, the MPC scheme for the MMC can be classified into two groups, namely, the per-phase model based MPC and the three-phase model based MPC. These MPC schemes have been presented in this chapter. In addition, these MPC algorithms have been implemented on a practical scaled-down three-phase MMC. The experimental results show that both MPC methods are successful in controlling the MMC. However, consistent with the previous analysis, the per-phase model based MPC performs poorly in terms of dc-link current as it cannot directly control the dc side of the MMC. In some cases, this per-phase method even produces a large ac component on the dc-link current. Instead, the three-phase model based MPC has a smaller current ripple on the dc-link current. Besides, due to the use of a more accurate mathematical model of the MMC, the three-phase model based method can achieve better steady-state performance, lower THDs and faster dynamic response on ac currents. The SM capacitor voltage fluctuations and the circulating currents are also lower with this method at low frequencies.

In overall, the per-phase model based MPC has lighter computational burden and lower control complexity. Besides, this method allows independent regulation for each phase of the

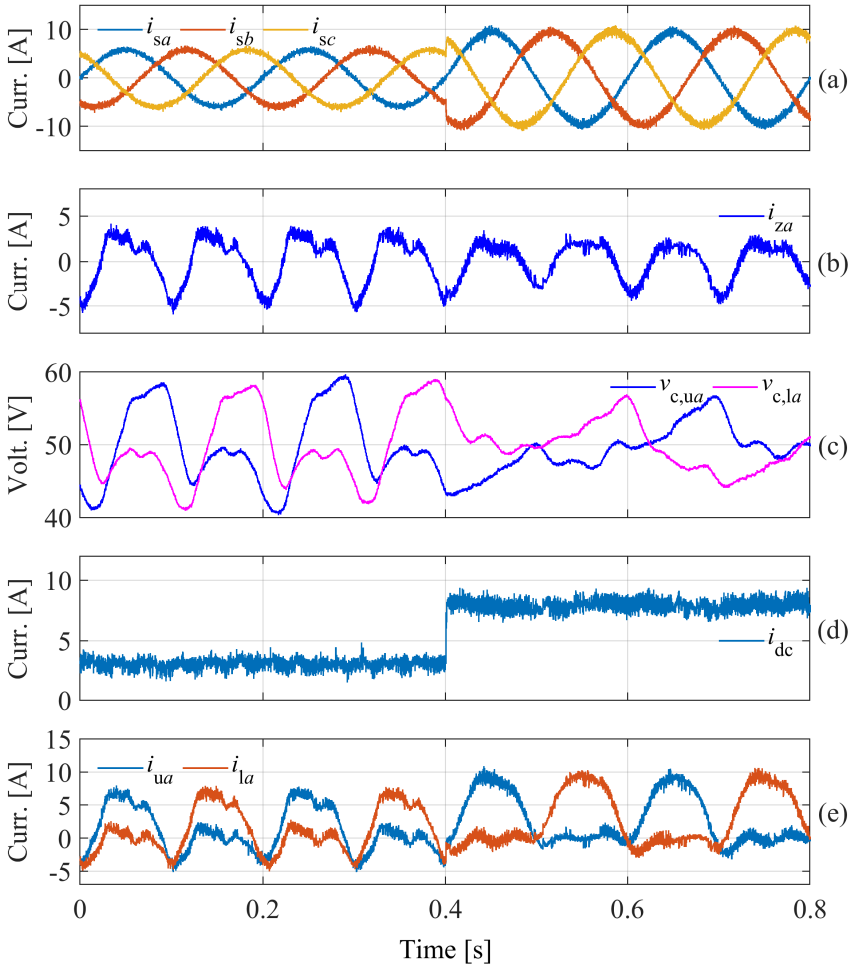

Figure 2.21: Step change in ac currents with per-phase model based MPC at 5 Hz.

MMC. Many efforts have been made in academia to reduce the computational burden of such per-phase based methods and thus this type of method can be easily applied to HVDC applications. However, such a method is difficult to use for medium-voltage (MV) motor drives because the effect of common-mode voltage is neglected. Also, since each phase is controlled individually, the performance of the dc side of the MMC cannot be guaranteed. In contrast, the three-phase model based MPC has a good steady-state performance and a fast transient response for ac currents. Moreover, due to the use of three-phase model of the MMC, the ac currents, circulating currents and dc-link current can be controlled independently. Such a three-phase model based method also achieves better results in the suppression of SM capacitor voltage fluctuations and circulating currents. However, due to its heavy computational burden, the three-phase model based MPC scheme is more suitable for MV motor drives as the number of SMs per arm is low. How to reduce the computational burden of the three-phase model based MPC is still an open issue.

CHAPTER 3

Model predictive control for modular multilevel converters based on bound-constrained quadratic programming

3.1 Introduction

As we know, although MMC has many advantages, its conventional control methods usually bring a complicated control structure, which further increases the difficulty of the control system design. Thus, it is necessary to investigate modern control strategies to simplify the control structure while achieving better control performance. In the past few decades, MPC has emerged as a common and efficient technique in the field of power electronics and motor drives due to its fast dynamic response, capability for the control of multiple variables cases, easy inclusion of non-linearities and constraints. Because of its successful application in other voltage-source converters, MPC has drawn more attention in recent years as an alternative control scheme in MMC systems. As MMC is a multi-input-multi-output (MIMO) system, the MPC method has the advantage of controlling such a system compared to conventional control methods. However, the heavy computational burden of the MPC method prevents it from being widely applied to MMC. Therefore, the existing MPC methods for the MMC system mainly focus on reducing the computational load.

In order to reduce the computational burden, many researchers use the per-phase model of the MMC to realize the MPC control. Based on the per-phase model, a direct FCS-MPC method was first proposed in [32] where the MPC controller has been used to control the output ac currents, SM capacitor voltages, and circulating currents by evaluating all the C_{2N}^{N} possible insertion index combinations per phase, where N is the number of SMs in each arm. However, it can be seen that the number of the evaluated combinations increases significantly when N increases, which leads to a huge computational burden. Besides, with this method, the MMC can only produce $N + 1$ output phase voltage levels. To solve this problem, an indirect FCS-MPC

scheme for MMCs has been proposed in [36]. This method only needs to obtain the number of the inserted SMs in each arm instead of determining the specific SMs that need to be inserted and uses an external voltage sorting algorithm to balance the SM capacitor voltages in the same arm. With this scheme, the computational burden has decreased significantly. In addition, the MMC can generate $2N + 1$ output phase voltage levels. The total number of possible combinations decreases to $(N + 1)^2$ in each phase. The calculation load can be further reduced by reasonably limiting the selection range of the possible voltage levels [37, 39–41]. In [40] and [41], the number of insertion index combinations evaluated in each control cycle only depends on the allowed range of the sum of the upper and lower insertion indices in each phase. The computational burden increases linearly with the number of SMs per arm. Therefore, these methods can reduce the calculation load dramatically. In [37], a fast MPC method for MMCs has been proposed. Only two or three voltage levels need to be evaluated in the optimization process regardless of the number of SMs. However, the dynamic performance of these methods will be influenced by sacrificing a large number of the possible switching combinations. In [52], the proper selection of the insertion index combinations can be determined by solving a quadratic programming problem. Unfortunately, this method is only applicable to the per-phase model based MPC.

Although these per-phase model-based MPC schemes can effectively reduce the computational complexity, the use of inaccurate models of MMC will lead to a degradation of system control performance, which has already been discussed in Chapter 2 in detail. Besides, the dc-link current/voltage and common-mode voltage cannot be regulated directly by using the per-phase model based MPC scheme and these variables, especially the common-mode voltage, are critical in the control of the medium-voltage (MV) motor drives. Therefore, it is necessary to study the implementation of the three-phase model based MPC for the MMC system in some cases.

The research on MPC schemes based on a three-phase model of the MMC can be found in [42, 53]. In [42], a dual-stage MPC method has been proposed to realize the three-phase model based MPC method. This method needs to evaluate $(N + 1)^3$ switching vectors at the first stage and $C_N^{N/2}$ switching states per arm at the second stage. Although it does not solve the problem of the heavy computational load caused by MPC schemes, dividing the control variables into two stages provides a way to reduce the computational burden. When the ac-side output voltage level can be determined in advance, the circulating current control can be achieved by evaluating the rest corresponding combinations at the second stage, which can effectively reduce the number of insertion index combinations to be evaluated. However, such MPC methods will naturally give priority to control objectives in the first stage, but cannot achieve comprehensive consideration of control objectives in the first stage and the second stage at the same time. It can be concluded that how to reduce the computational burden of the FCS-MPC method based on the three-phase model of MMCs is still an open issue.

In addition to the studies on FCS-MPC methods, some researchers began to use the modulated MPC technique for the MMC system to achieve less computational burden and better steady-state performance [45–47, 51]. The method introduced in [45] is similar to the per-phase model based FCS-MPC method. It first selects two optimal adjacent voltage levels based on the cost function. The duty cycles of these two voltage levels can be calculated in each control period. Although the steady-state performance can be improved by using this method, there are still $(N + 1)$ voltage levels per phase that need to be evaluated. Besides, using the per-phase

model of MMC may reduce the control performance compared to using the three-phase model. The modulated MPC methods introduced in [46,47,51] share a similar principle whose essence of these methods is to use the unconstrained solution of the optimal problem, which can also be regarded as the deadbeat control for MMC. The benefit of these methods is that the computational burden is independent of the number of SMs and is extremely low. The steady-state performance of these modulated methods is also improved compared with FCS-MPC methods under the same sampling frequency. However, these methods ignore the role of weighting factors, which affect the control performance when the MMC operates under high modulation index or during transients.

In order to solve the problems mentioned above, an MPC with a bound-constrained quadratic programming solver has been proposed. At first, the control problem for the MMC system based on the MPC method has been formulated as a QP problem with bound constraints. After that, a fast bound-constrained QP method [50] has been employed to obtain the solution to this control problem. Then, this continuous solution can be used to realize the modulated MPC scheme. Moreover, based on this continuous solution, a computationally efficient FCS-MPC method can be achieved. As we know, it is impractical to use an exhaustive way to search all the $(N+1)^6$ insertion index combinations in the control set to find the optimal one. Therefore, the basic idea of the proposed FCS-MPC method is to establish a reduced control set according to the continuous solution obtained by the QP solver. Although the optimal insertion index combination may not always be found, the best one in the reduced control set can also guarantee a good control performance. Besides, the reduced control set only includes 2^6 insertion index combinations and it is independent of the number of SMs per arm. Therefore, the proposed FCS-MPC method is very suitable for HVDC applications, in which N is large. Meanwhile, due to the use of the three-phase model of MMC, the proposed methods can be combined with the circulating current injection technology to realize the control of MV motors.

3.2 Modulated MPC algorithm for MMCs

3.2.1 Existing modulated MPC algorithms for MMCs

As discussed in the introduction, the existing modulated MPC schemes based on different ideas can be divided into two groups. In the first group [45], the two optimal voltage levels are first selected and their duty cycles are calculated by minimizing the cost function. The methods in the other group [46, 47, 51] can be seen as a kind of deadbeat control. From the point of view of solving an optimization problem, the process of these methods to obtain the insertion indices is to solve the unconstrained solution of an optimization problem. As the method introduced in [45] has been fully elaborated and compared in [47], this method will not be discussed in this chapter. Instead, the method in [47] will be introduced and compared as an example to illustrate the limitation of this kind of method and the necessity of using the optimal solution for the modulated MPC algorithm.

3.2.1.1 Problem reformulation

The per-phase model of the MMC has been used in [47]. It should be noted that for such a method based on the three-phase model we can be refer to [51]. For the sake of elucidation, the

method in [47] is used as an example.

According to (2.7), the per-phase model of the MMC can be formed in the compact matrix form of the control variables $v_{\mathrm{l}x}(k)$ and $v_{\mathrm{u}x}(k)$ as

$$\underbrace{\begin{bmatrix} i_{\mathrm{s}x}(k+1) \\ i_{\mathrm{cir}x}(k+1) \end{bmatrix}}_{\boldsymbol{y}} = \underbrace{\begin{bmatrix} -\frac{T_{\mathrm{s}}}{2L_{\mathrm{eq}}} & \frac{T_{\mathrm{s}}}{2L_{\mathrm{eq}}} \\ -\frac{T_{\mathrm{s}}}{2L} & -\frac{T_{\mathrm{s}}}{2L} \end{bmatrix}}_{\boldsymbol{B}} \underbrace{\begin{bmatrix} v_{\mathrm{u}x}(k) \\ v_{\mathrm{l}x}(k) \end{bmatrix}}_{\boldsymbol{u}} + \underbrace{\begin{bmatrix} \left(1 - \frac{R_{\mathrm{s}}T_{\mathrm{s}}}{L_{\mathrm{eq}}}\right) i_{\mathrm{s}x}(k) \\ i_{\mathrm{cir}x}(k) + \frac{T_{\mathrm{s}}}{2L} V_{\mathrm{dc}}(k) \end{bmatrix}}_{\boldsymbol{d}}. \tag{3.1}$$

where $L_{\mathrm{eq}} = L_{\mathrm{s}} + L/2$ and $x = a, b, c$. The cost function defined in (2.29) can be written as

$$J = (\boldsymbol{y}^* - \boldsymbol{y})^{\mathrm{T}} \boldsymbol{W} (\boldsymbol{y}^* - \boldsymbol{y}). \tag{3.2}$$

where $\boldsymbol{y}^* = \begin{bmatrix} i^*_{\mathrm{s}x} & i^*_{\mathrm{cir}x} \end{bmatrix}^{\mathrm{T}}$ and $\boldsymbol{W} = diag(1, w_1)$. Note that $\boldsymbol{W}$ is called weighting matrix. Applying (3.1) into (3.2) and neglecting the constant term in J, the cost function can be rewritten as

$$\tilde{J} = \boldsymbol{u}^{\mathrm{T}} \boldsymbol{B}^{\mathrm{T}} \boldsymbol{W} \boldsymbol{B} \boldsymbol{u} + 2(\boldsymbol{d} - \boldsymbol{y}^*)^{\mathrm{T}} \boldsymbol{W} \boldsymbol{B} \boldsymbol{u}. \tag{3.3}$$

According to (3.3), the unconstrained solution can be derived as

$$\boldsymbol{u}_{\mathrm{unc}} = -(\boldsymbol{B}^{\mathrm{T}} \boldsymbol{W} \boldsymbol{B})^{-1} \Big((\boldsymbol{d} - \boldsymbol{y}^*)^{\mathrm{T}} \boldsymbol{W} \boldsymbol{B} \Big)^{\mathrm{T}} = \boldsymbol{B}^{-1} (\boldsymbol{y}^* - \boldsymbol{d}). \tag{3.4}$$

As $\boldsymbol{B}$ is a two-dimensional matrix, its inverse matrix can be easily obtained as

$$\boldsymbol{B}^{-1} = \begin{bmatrix} -\frac{L_{\mathrm{eq}}}{T_{\mathrm{s}}} & -\frac{L}{T_{\mathrm{s}}} \\ \frac{L_{\mathrm{eq}}}{T_{\mathrm{s}}} & -\frac{L}{T_{\mathrm{s}}} \end{bmatrix}. \tag{3.5}$$

Based on (3.5), the expressions of $v_{\mathrm{l}x}(k)$ and $v_{\mathrm{u}x}(k)$ can be derived as

$$\begin{aligned} v_{\mathrm{u}x}(k) &= -\frac{L_{\mathrm{eq}}}{T_{\mathrm{s}}}(i^*_{\mathrm{s}x} - i_{\mathrm{s}x}(k)) - R_{\mathrm{s}} i_{\mathrm{s}x}(k) - \frac{L}{T_{\mathrm{s}}}(i^*_{\mathrm{cir}x} - i_{\mathrm{cir}x}(k)) + \frac{V_{\mathrm{dc}}(k)}{2} \\ v_{\mathrm{l}x}(k) &= \frac{L_{\mathrm{eq}}}{T_{\mathrm{s}}}(i^*_{\mathrm{s}x} - i_{\mathrm{s}x}(k)) + R_{\mathrm{s}} i_{\mathrm{s}x}(k) - \frac{L}{T_{\mathrm{s}}}(i^*_{\mathrm{cir}x} - i_{\mathrm{cir}x}(k)) + \frac{V_{\mathrm{dc}}(k)}{2} \end{aligned} \tag{3.6}$$

According to the indirect modulation method, the modulation references can be obtained as

$$m_{\mathrm{u}x} = \frac{v_{\mathrm{u}x}(k)}{\sum_{i=1}^{N} v^i_{\mathrm{c,u}x}},\ m_{\mathrm{l}x} = \frac{v_{\mathrm{l}x}(k)}{\sum_{i=1}^{N} v^i_{\mathrm{c,l}x}}. \tag{3.7}$$

The insertion indices are derived as

$$n_{\mathrm{u}x} = N m_{\mathrm{u}x},\ n_{\mathrm{l}x} = N m_{\mathrm{l}x}. \tag{3.8}$$

It should be noted that if we replace the predicted value $\boldsymbol{y}$ with the reference value $\boldsymbol{y}^*$ and solve the control variables $\boldsymbol{u}$ according to (3.1), we can obtain the same expression as (3.4). The control law of the conventional deadbeat control is obtained in this way. From (3.4), it seems that the weighting factor is not required. However, the solution in (3.4) does not take

into account the actual physical constraints. The control variables should naturally satisfy the following constraints:

$$\begin{aligned} 0 \leq v_{\mathrm{u}x}(k) \leq \sum_{i=1}^{N} v_{\mathrm{c,u}x}^{i}, \\ 0 \leq v_{\mathrm{l}x}(k) \leq \sum_{i=1}^{N} v_{\mathrm{c,l}x}^{i}. \end{aligned} \tag{3.9}$$

When the solution obtained by (3.4) does not satisfy these constraints (3.9), the common way is to saturate the solution, which can be expressed as

$$\boldsymbol{u}_{\mathrm{sat}} = \min(\boldsymbol{u}_{\mathrm{b}}, \max(\boldsymbol{l}_{\mathrm{b}}, \boldsymbol{u}_{\mathrm{unc}})), \tag{3.10}$$

where $\boldsymbol{l}_{\mathrm{b}} = [0\ 0]^{\mathrm{T}}$ and $\boldsymbol{u}_{\mathrm{b}} = [\sum_{i=1}^{N} v_{\mathrm{c,u}x}^{i}\ \sum_{i=1}^{N} v_{\mathrm{c,l}x}^{i}]^{\mathrm{T}}$ represent the lower bound and upper bound of the control variable $\boldsymbol{u}$, respectively. This saturation approach is proper when $\boldsymbol{B}^{\mathrm{T}}\boldsymbol{W}\boldsymbol{B}$ is a diagonal matrix with positive elements. However, such a saturation way cannot get the optimal solution in most cases, and thus the effect of the weighting factor is highlighted. To better illustrate the effect of different weighting factors on the optimal solution, a simple example has been given as follows:

$$\boldsymbol{B} = \begin{bmatrix} 1 & 1 \\ -1 & 1 \end{bmatrix}, (\boldsymbol{y}^{*} - \boldsymbol{d}) = \begin{bmatrix} -2 \\ -1 \end{bmatrix}, \boldsymbol{l}_{b} = \begin{bmatrix} 0 \\ 0 \end{bmatrix}, \boldsymbol{u}_{b} = \begin{bmatrix} 1 \\ 1 \end{bmatrix}. \tag{3.11}$$

According to (3.4), the unconstrained solution can be easily obtained, which $\boldsymbol{u}_{\mathrm{unc}} = \begin{bmatrix} 0.5 & 1.5 \end{bmatrix}$. We can obtain different optimal solutions when the weighting factor w_1 is different. Fig. 3.1 is a contour plot of the cost function $\tilde{J}$. It describes the different locations of the optimal solution when the w_1 are 0.3 and 3.0, respectively. Fig. 3.1 shows the influence of different weighting factors on the optimal solution. It can be seen that the unconstrained solutions ($\boldsymbol{u}_{\mathrm{unc}}$) are the same for two different weighting factors and thus the corresponding saturation solutions ($\boldsymbol{u}_{\mathrm{sat}}$) are the same according to (3.10). However, the distribution patterns of contours in Fig. 3.1(a) and (b) are different due to the different weighting factors, leading to different optimal solutions ($\boldsymbol{u}^{*}$).

It can be concluded that the effect of the weighting factor can be neglected when the unconstrained solution satisfies the constraints. However, when the unconstrained solution is not in the feasible region, the impact of the weighting factor should not be ignored and the selection of the weighting factor is necessary. In addition, it is not appropriate to use the per-phase model of the MMC in this situation. This is because the average value of the common-mode voltage is not zero in the sampling interval, which will affect the output ac currents.

3.2.2 Proposed modulated MPC algorithm for MMCs

3.2.2.1 Three-phase model of MMC in the matrix form

In this algorithm, the three-phase model of MMC will be applied to achieve better control performance. According to (2.20), the discrete-time mathematical model in the compact matrix

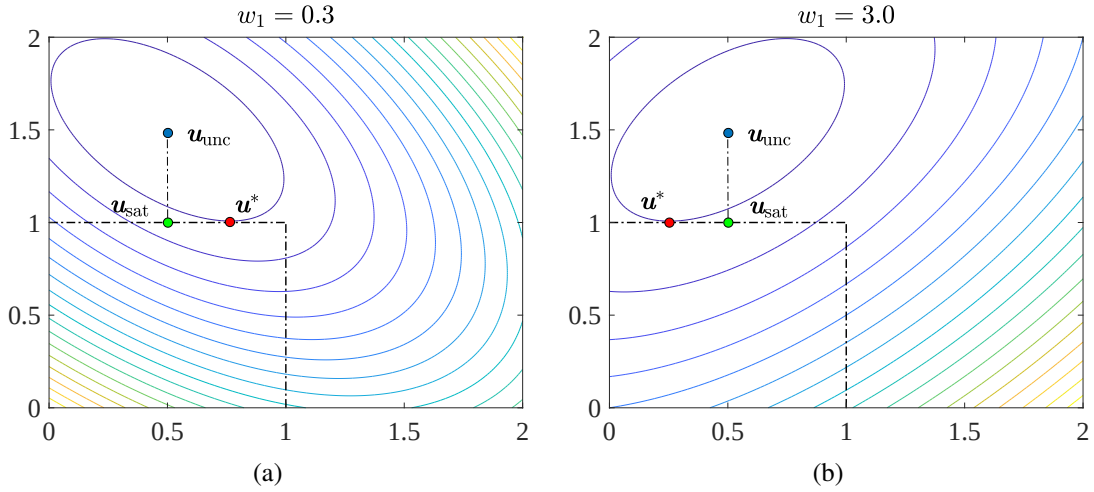

Figure 3.1: Optimal solutions with different w_1

form can be obtained as

$$\boldsymbol{y} = \boldsymbol{A}\boldsymbol{x} + \boldsymbol{b}, \tag{3.12}$$

where

$$\boldsymbol{y} = \begin{bmatrix} i_{sa}(k+1) \\ i_{sb}(k+1) \\ i_{sc}(k+1) \\ i_{za}(k+1) \\ i_{zb}(k+1) \\ i_{zc}(k+1) \end{bmatrix}, \boldsymbol{x} = \begin{bmatrix} x_1 \\ x_2 \\ x_3 \\ x_4 \\ x_5 \\ x_6 \end{bmatrix} = \begin{bmatrix} n_{ua} \\ n_{la} \\ n_{ub} \\ n_{lb} \\ n_{uc} \\ n_{lc} \end{bmatrix}, \boldsymbol{b} = \begin{bmatrix} \alpha_1 i_{sa}(k) \\ \alpha_1 i_{sb}(k) \\ \alpha_1 i_{sc}(k) \\ i_{za}(k) \\ i_{zb}(k) \\ i_{zc}(k) \end{bmatrix},$$

$$\boldsymbol{A} = \frac{T_s}{3} \begin{bmatrix} \frac{-2\bar{v}_{ua}}{L_d} & \frac{2\bar{v}_{la}}{L_d} & \frac{\bar{v}_{ub}}{L_d} & \frac{-\bar{v}_{lb}}{L_d} & \frac{\bar{v}_{uc}}{L_d} & \frac{-\bar{v}_{lc}}{L_d} \\ \frac{\bar{v}_{ua}}{L_d} & \frac{-\bar{v}_{la}}{L_d} & \frac{-2\bar{v}_{ub}}{L_d} & \frac{2\bar{v}_{lb}}{L_d} & \frac{\bar{v}_{uc}}{L_d} & \frac{-\bar{v}_{lc}}{L_d} \\ \frac{\bar{v}_{ua}}{L_d} & \frac{-\bar{v}_{la}}{L_d} & \frac{\bar{v}_{ub}}{L_d} & \frac{-\bar{v}_{lb}}{L_d} & \frac{-2\bar{v}_{uc}}{L_d} & \frac{2\bar{v}_{lc}}{L_d} \\ \frac{-\bar{v}_{ua}}{L} & \frac{-\bar{v}_{la}}{L} & \frac{\bar{v}_{ub}}{2L} & \frac{\bar{v}_{lb}}{2L} & \frac{\bar{v}_{uc}}{2L} & \frac{\bar{v}_{lc}}{2L} \\ \frac{\bar{v}_{ua}}{2L} & \frac{\bar{v}_{la}}{2L} & \frac{-\bar{v}_{ub}}{L} & \frac{-\bar{v}_{lb}}{L} & \frac{\bar{v}_{uc}}{2L} & \frac{\bar{v}_{lc}}{2L} \\ \frac{\bar{v}_{ua}}{2L} & \frac{\bar{v}_{la}}{2L} & \frac{\bar{v}_{ub}}{2L} & \frac{\bar{v}_{lb}}{2L} & \frac{-\bar{v}_{uc}}{L} & \frac{-\bar{v}_{lc}}{L} \end{bmatrix}.$$

In (3.12), $\boldsymbol{y}$ presents the prediction values of ac-side currents and circulating currents at $k+1$ time instant and $\boldsymbol{x}$ is the vector of the insertion indices n_{yx} ($y = u, l$ and $x = a, b, c$). $\bar{v}_{yx} = \frac{1}{N}\sum_{i=1}^{N} v_{c,yx}^i$ is the average voltage in arm y of phase x. $\alpha_1 = 1 - \frac{2R_s T_s}{2L_s + L}$ in $\boldsymbol{b}$ are coefficients. $L_d = 2L_s + L$ is the ac-side equivalent inductance. Here we assume that the capacitor voltage of each SM in the same arm is well balanced due to the voltage sorting algorithm.

Assuming that the grid side is well balanced and thus the sum of the ac-side currents is zero. Based on the definition of the circulating current, the sum of the circulating currents is also

equal to zero. Therefore, the Clarke transformation can be used to reduce the dimension of $\boldsymbol{y}$. The Clarke transformation is given by

$$\boldsymbol{C} = \frac{2}{3}\begin{bmatrix} 1 & -\frac{1}{2} & -\frac{1}{2} \\ 0 & \frac{\sqrt{3}}{2} & -\frac{\sqrt{3}}{2} \end{bmatrix}. \tag{3.13}$$

The augmented Clark matrix is defined as

$$\bar{\boldsymbol{C}} = \begin{bmatrix} \boldsymbol{C} & \boldsymbol{O}_{2\times 3} \\ \boldsymbol{O}_{2\times 3} & \boldsymbol{C} \end{bmatrix}. \tag{3.14}$$

The discrete-time mathematical model in the stationary α-β frame can be expressed as

$$\bar{\boldsymbol{y}} = \bar{\boldsymbol{A}}\boldsymbol{x} + \bar{\boldsymbol{b}}, \tag{3.15}$$

where $\bar{\boldsymbol{y}} = \bar{\boldsymbol{C}}\boldsymbol{y}$, $\bar{\boldsymbol{A}} = \bar{\boldsymbol{C}}\boldsymbol{A}$ and $\bar{\boldsymbol{b}} = \bar{\boldsymbol{C}}\boldsymbol{b}$. Besides, the other two control variables, the MMC equivalent dc-link output voltage $v_{\rm sum}$ and the common mode voltage $v_{\rm NO}$, are required to control the dc-link voltage/current and eliminate the common mode voltage of the grid. They are rewritten as

$$\begin{aligned} v_{\rm sum} &= \underbrace{\frac{1}{3}\begin{bmatrix} \bar{v}_{{\rm u}a} & \bar{v}_{{\rm l}a} & \bar{v}_{{\rm u}b} & \bar{v}_{{\rm l}b} & \bar{v}_{{\rm u}c} & \bar{v}_{{\rm l}c} \end{bmatrix}}_{\boldsymbol{a_1}} \boldsymbol{x}, \\ v_{\rm NO} &= \underbrace{\frac{1}{6}\begin{bmatrix} -\bar{v}_{{\rm u}a} & \bar{v}_{{\rm l}a} & -\bar{v}_{{\rm u}b} & \bar{v}_{{\rm l}b} & -\bar{v}_{{\rm u}c} & \bar{v}_{{\rm l}c} \end{bmatrix}}_{\boldsymbol{a_2}} \boldsymbol{x}. \end{aligned} \tag{3.16}$$

At last, the augmented discrete-time mathematical model can be expressed as

$$\hat{\boldsymbol{y}} = \begin{bmatrix} i_{{\rm s}\alpha}(k+1) \\ i_{{\rm s}\beta}(k+1) \\ i_{{\rm z}\alpha}(k+1) \\ i_{{\rm z}\beta}(k+1) \\ i_{\rm dc}(k+1) \\ v_{\rm NO} \end{bmatrix} = \underbrace{\begin{bmatrix} \bar{\boldsymbol{A}} \\ -\frac{3T_{\rm s}}{2L}\boldsymbol{a_1} \\ \boldsymbol{a_2} \end{bmatrix}}_{\hat{\boldsymbol{A}}} \boldsymbol{x} + \underbrace{\begin{bmatrix} \bar{\boldsymbol{b}} \\ \frac{3T_{\rm s}}{2L}V_{\rm dc} \\ 0 \end{bmatrix}}_{\hat{\boldsymbol{b}}}. \tag{3.17}$$

Note that (3.17)) represents the model of the MMC system operating in the inverter mode. When the MMC system operates in the rectifier mode, $v_{\rm sum}$ should be directly controlled to the desired dc-link voltage $V_{\rm dc}^*$.

The cost function defined in (2.31) can be reformed in α-β frame as

$$\begin{aligned} J = &\left\|\boldsymbol{i}_{{\rm s}\alpha\beta}^* - \boldsymbol{i}_{{\rm s}\alpha\beta}(k+1)\right\|_2^2 + w_1\left\|\boldsymbol{i}_{{\rm z}\alpha\beta}^* - \boldsymbol{i}_{{\rm z}\alpha\beta}(k+1)\right\|_2^2 \\ &+ w_2\left\|i_{\rm dc}^* - i_{\rm dc}(k+1)\right\|_2^2 + w_3\left\|v_{\rm NO}^* - v_{\rm NO}\right\|_2^2. \end{aligned} \tag{3.18}$$

Now the modulated MPC scheme can be equivalent to solving a QP problem as follows:

$$\begin{aligned} &\min_{\boldsymbol{x}}\ J(\boldsymbol{x}) = \frac{1}{2}\boldsymbol{x}^T\boldsymbol{Q}\boldsymbol{x} + \boldsymbol{d}^T\boldsymbol{x} \\ &\text{subject to}\ \ \boldsymbol{0} \preceq \boldsymbol{x} \preceq \boldsymbol{N} \end{aligned} \tag{3.19}$$

where $\boldsymbol{Q} = \hat{\boldsymbol{A}}^T \boldsymbol{W} \hat{\boldsymbol{A}}$, $\boldsymbol{d} = \hat{\boldsymbol{A}}^T \boldsymbol{W}(\hat{\boldsymbol{b}} - \boldsymbol{y}^*)$, with diagonal weighting matrix

$$\boldsymbol{W} = \begin{bmatrix} 1 & & & & & & \\ & 1 & & & & & \\ & & w_1 & & & & \\ & & & w_1 & & & \\ & & & & w_2 & & \\ & & & & & w_3 & \end{bmatrix}, \text{ and } \boldsymbol{y}^* = \begin{bmatrix} i^*_{\mathrm{s}\alpha} \\ i^*_{\mathrm{s}\beta} \\ i^*_{\mathrm{z}\alpha} \\ i^*_{\mathrm{z}\beta} \\ i^*_{\mathrm{dc}} \\ v^*_{\mathrm{NO}} \end{bmatrix}, \boldsymbol{0} = \begin{bmatrix} 0 \\ 0 \\ 0 \\ 0 \\ 0 \\ 0 \end{bmatrix}, \text{ and } \boldsymbol{N} = \begin{bmatrix} N \\ N \\ N \\ N \\ N \\ N \end{bmatrix}.$$

It should be noted that in this case the insertion indices defined in $\boldsymbol{x}$ are selected as control variables. The arm voltage ($\boldsymbol{u} = [v_{\mathrm{u}a}\ v_{\mathrm{l}a}\ v_{\mathrm{u}b}\ v_{\mathrm{l}b}\ v_{\mathrm{u}c}\ v_{\mathrm{l}c}]^T$) can also be applied as the control variable in other cases. The relationship between these two types of control variables is expressed as follows:

$$\boldsymbol{u} = \underbrace{\begin{bmatrix} \bar{v}_{\mathrm{u}a} & & & & & \\ & \bar{v}_{\mathrm{l}a} & & & & \\ & & \bar{v}_{\mathrm{u}b} & & & \\ & & & \bar{v}_{\mathrm{l}b} & & \\ & & & & \bar{v}_{\mathrm{u}c} & \\ & & & & & \bar{v}_{\mathrm{l}c} \end{bmatrix}}_{\bar{\boldsymbol{V}}} \boldsymbol{x} \tag{3.20}$$

As $\bar{\boldsymbol{V}}$ is the diagonal weighting matrix, it is easy to convert (3.19) to the following optimization problem as

$$\begin{aligned} &\min_{\boldsymbol{x}} \ J(\boldsymbol{x}) = \frac{1}{2}\boldsymbol{u}^{\mathrm{T}}\bar{\boldsymbol{Q}}\boldsymbol{u} + \bar{\boldsymbol{d}}^{\mathrm{T}}\boldsymbol{u} \\ &\text{subject to } \ \boldsymbol{l}_{\mathrm{b}} \preceq \ \boldsymbol{u} \preceq \boldsymbol{u}_{\mathrm{b}} \end{aligned} \tag{3.21}$$

where $\bar{\boldsymbol{Q}} = \bar{\boldsymbol{V}}^{-\mathrm{T}}\boldsymbol{Q}\bar{\boldsymbol{V}}^{-1}$, $\bar{\boldsymbol{d}} = \bar{\boldsymbol{V}}^{-\mathrm{T}}\boldsymbol{d}$, $\boldsymbol{l}_{\mathrm{b}} = \boldsymbol{0}$ and $\boldsymbol{u}_{\mathrm{b}} = \bar{\boldsymbol{V}}\boldsymbol{N}$. The benefit of using the arm voltages as control variables is that the $\bar{\boldsymbol{Q}}$ and $\bar{\boldsymbol{d}}$ are constant when the system parameters are known in advance. Thus, the inverse matrix of $\bar{\boldsymbol{Q}}$ can be calculated beforehand, which will be useful for solving the optimization problem online. However, since the value of each control variable in $\boldsymbol{u}$ may be much larger than that of each element in the $\bar{\boldsymbol{Q}}$ matrix, it may lead to the decline of the calculation accuracy. Therefore, when $\boldsymbol{u}$ is selected, the variables and parameters of the MMC system need to be normalized in advance.

The QP problem (3.21) is equivalent to problem (3.19) and thus the following part will focus on solving the optimization problem (3.19) without loss of generality.

3.2.2.2 Bound-constrained quadratic programming

Considering (3.19), the associated Lagrangian function can be constructed as

$$\mathcal{L}(\boldsymbol{x}, \boldsymbol{s}, \boldsymbol{t}) = \frac{1}{2}\boldsymbol{x}^T\boldsymbol{Q}\boldsymbol{x} + \boldsymbol{d}^T\boldsymbol{x} + \boldsymbol{s}^T(\boldsymbol{x} - \boldsymbol{N}) + \boldsymbol{t}^T(\boldsymbol{0} - \boldsymbol{x}), \tag{3.22}$$

where $\boldsymbol{s}$ and $\boldsymbol{t}$ are Lagrange multipliers. The Karush-Kuhn-Tucker (KKT) condition is given by

$$\begin{aligned} \boldsymbol{Q}\boldsymbol{x} + \boldsymbol{d} + \boldsymbol{s} - \boldsymbol{t} &= \boldsymbol{0}, && \text{(3.23a)} \\ s_i(x_i - N) &= 0, \forall i \in \mathcal{C} && \text{(3.23b)} \\ t_i(0 - x_i) &= 0, \forall i \in \mathcal{C} && \text{(3.23c)} \\ \boldsymbol{0} \preceq \boldsymbol{x} \preceq \boldsymbol{N}, \boldsymbol{s} \succeq \boldsymbol{0}, \boldsymbol{t} &\succeq \boldsymbol{0}, && \text{(3.23d)} \end{aligned}$$

where $\mathcal{C} = \{1, 2, ..., n\}$, n is the dimension of $\boldsymbol{x}$. It is well known that the QP problem (3.19) reaches the minimum if and only if $(\boldsymbol{x}, \boldsymbol{s}, \boldsymbol{t})$ satisfies the KKT conditions in (3.23). The crucial point in solving (3.19) is to identify those inequalities which are active. Besides, in practical applications, the speed of finding these active constraints is also important. An infeasible active set method [50] for solving such a QP problem is adopted due to its fast convergence. This method only requires very few iterations to solve a QP problem. In order to describe the algorithm briefly, some working sets ($\mathcal{A}_l$, $\mathcal{A}_u$, and $\mathcal{I}$) are declared in advance. $\mathcal{A}_l$ is the index set for which the lower bound constraint is active. For each $i \in \mathcal{A}_l$, x_i will touch the lower bound, which is $x_i = 0$ in this case. Similarly, $\mathcal{A}_u$ is the index set for which the upper bound constraint is active. For each $i \in \mathcal{A}_u$, there is $x_i = N$. $\mathcal{A}$ is the set for active constraints and it can be expressed as $\mathcal{A} = \mathcal{A}_l \cup \mathcal{A}_u$. Set $\mathcal{I}$ is the complementary set of $\mathcal{A}$ and it can be obtained by $\mathcal{I} = \mathcal{C} \setminus \mathcal{A}$. It assumes that for each $i \in \mathcal{I}$, x_i neither exceeds the lower nor the upper bound. According to the present working sets ($\mathcal{A}_u$, $\mathcal{A}_l$ and $\mathcal{I}$) and KKT conditions (4.20b) and (4.20c), we can easily obtain the following equations as

$$\begin{aligned} \boldsymbol{x}_{\mathcal{A}_l} = \boldsymbol{0},\ \boldsymbol{s}_{\mathcal{A}_l} = \boldsymbol{0}, \\ \boldsymbol{x}_{\mathcal{A}_u} = \boldsymbol{N},\ \boldsymbol{t}_{\mathcal{A}_u} = \boldsymbol{0}, \\ \boldsymbol{s}_{\mathcal{I}} = \boldsymbol{0},\ \boldsymbol{t}_{\mathcal{I}} = \boldsymbol{0}. \end{aligned} \tag{3.24}$$

Now only $\boldsymbol{x}_{\mathcal{I}}$, $\boldsymbol{s}_{\mathcal{A}_u}$ and $\boldsymbol{t}_{\mathcal{A}_l}$ need to be solved. According to (4.20a), these variables can be obtained by solving the following equation as

$$\begin{bmatrix} \boldsymbol{Q}_{\mathcal{A}_u\mathcal{A}_u} & \boldsymbol{Q}_{\mathcal{A}_u\mathcal{A}_l} & \boldsymbol{Q}_{\mathcal{A}_u\mathcal{I}} \\ \boldsymbol{Q}_{\mathcal{A}_l\mathcal{A}_u} & \boldsymbol{Q}_{\mathcal{A}_l\mathcal{A}_l} & \boldsymbol{Q}_{\mathcal{A}_l\mathcal{I}} \\ \boldsymbol{Q}_{\mathcal{I}_I\mathcal{A}_u} & \boldsymbol{Q}_{\mathcal{I}_I\mathcal{A}_l} & \boldsymbol{Q}_{\mathcal{I}\mathcal{I}} \end{bmatrix} \begin{bmatrix} \boldsymbol{x}_{\mathcal{A}_u} \\ \boldsymbol{x}_{\mathcal{A}_l} \\ \boldsymbol{x}_{\mathcal{I}} \end{bmatrix} + \begin{bmatrix} \boldsymbol{d}_{\mathcal{A}_u} \\ \boldsymbol{d}_{\mathcal{A}_l} \\ \boldsymbol{d}_{\mathcal{I}} \end{bmatrix} + \begin{bmatrix} \boldsymbol{s}_{\mathcal{A}_u} \\ \boldsymbol{s}_{\mathcal{A}_l} \\ \boldsymbol{s}_{\mathcal{I}} \end{bmatrix} - \begin{bmatrix} \boldsymbol{t}_{\mathcal{A}_u} \\ \boldsymbol{t}_{\mathcal{A}_l} \\ \boldsymbol{t}_{\mathcal{I}} \end{bmatrix} = \boldsymbol{0}. \tag{3.25}$$

Based on (4.21), $\boldsymbol{x}_{\mathcal{I}}$ can be solved firstly by

$$\boldsymbol{Q}_{\mathcal{I}\mathcal{I}}\boldsymbol{x}_{\mathcal{I}} = -\boldsymbol{d}_{\mathcal{I}} - \boldsymbol{Q}_{\mathcal{I}\mathcal{A}_u}\boldsymbol{x}_{\mathcal{A}_u} - \boldsymbol{Q}_{\mathcal{I}\mathcal{A}_l}\boldsymbol{x}_{\mathcal{A}_l}. \tag{3.26}$$

Here $\boldsymbol{Q}_{\mathcal{I}\mathcal{I}}$ is convex and hence the system (4.23) is solvable. After $\boldsymbol{x}_{\mathcal{I}}$ is solved, the $\boldsymbol{s}_{\mathcal{A}_u}$ and $\boldsymbol{t}_{\mathcal{A}_l}$ can be obtained as

$$\begin{aligned} \boldsymbol{s}_{\mathcal{A}_u} &= -\boldsymbol{Q}_{\mathcal{A}_u\mathcal{A}_u}\boldsymbol{x}_{\mathcal{A}_u} - \boldsymbol{Q}_{\mathcal{A}_u\mathcal{A}_l}\boldsymbol{x}_{\mathcal{A}_l} - \boldsymbol{Q}_{\mathcal{A}_u\mathcal{I}}\boldsymbol{x}_{\mathcal{I}} - \boldsymbol{d}_{\mathcal{A}_u}, \\ \boldsymbol{t}_{\mathcal{A}_l} &= \boldsymbol{Q}_{\mathcal{A}_l\mathcal{A}_u}\boldsymbol{x}_{\mathcal{A}_u} + \boldsymbol{Q}_{\mathcal{A}_l\mathcal{A}_l}\boldsymbol{x}_{\mathcal{A}_l} + \boldsymbol{Q}_{\mathcal{A}_l\mathcal{I}}\boldsymbol{x}_{\mathcal{I}} + \boldsymbol{d}_{\mathcal{A}_l}. \end{aligned} \tag{3.27}$$

All the variables have been solved based on the present active set $\mathcal{A}$. If our guess for the present active set $\mathcal{A}$ is correct, then $\boldsymbol{0} \preceq \boldsymbol{x}_{\mathcal{I}} \preceq \boldsymbol{N}$, $\boldsymbol{s}_{\mathcal{A}_u} \succeq \boldsymbol{0}$ and $\boldsymbol{t}_{\mathcal{A}_l} \succeq \boldsymbol{0}$ will be satisfied. Otherwise, a

new guess for the working sets $\mathcal{A}_l$, $\mathcal{A}_u$ and $\mathcal{A}$ should be made for the next iteration, which we denote by $\mathcal{A}_l^+$, $\mathcal{A}_u^+$ and $\mathcal{A}^+$. Consider the following cases: If $s_i > 0$ ($i \in \mathcal{A}_u$), it indicates that our previous guess $i \in \mathcal{A}_u$ is reasonable. Similarly, if $t_i > 0$ ($i \in \mathcal{A}_l$), the index of t_i should be included in the new working set $\mathcal{A}_l^+$. $\boldsymbol{x}_\mathcal{I}$ should also be checked and thus the guess for the new working sets can be summarized as follows

$$\begin{aligned} \mathcal{A}_l^+ &= \{i : x_i < 0, \text{or } x_i = 0 \ \& \ \mathrm{t_i} > 0\} \\ \mathcal{A}_u^+ &= \{i : x_i > N, \text{or } x_i = N \ \& \ \mathrm{s_i} > 0\} \\ \mathcal{A}^+ &= \mathcal{A}_l^+ \cup \mathcal{A}_u^+ \end{aligned} \tag{3.28}$$

With these new working sets, we can repeat the procedure to get the new solution and check whether the KKT condition is satisfied. The detail of convergence analysis of the algorithm can be found in [50]. An intuitive description about this algorithm are summarized in Algorithm 1.

Algorithm 1 Infeasible Active Set Method

function IAS($\boldsymbol{Q}$,$\boldsymbol{d}$,$\boldsymbol{a}$,$\boldsymbol{b}$)
  $\mathcal{C} \leftarrow \{1, 2, ..., n\}$, $\boldsymbol{a} \leftarrow \mathbf{0}$, $\boldsymbol{b} \leftarrow \boldsymbol{N}$
  $\mathcal{A}_u \leftarrow \emptyset$, $\mathcal{A}_l \leftarrow \emptyset$, $\mathcal{I} \leftarrow \mathcal{C} \setminus \mathcal{A}_u \setminus \mathcal{A}_l$
  Solutionfound $\leftarrow 0$
  while Solutionfound $== 0$ **do**
    $\boldsymbol{x}_{\mathcal{A}_u} \leftarrow \boldsymbol{b}_{\mathcal{A}_u}$
    $\boldsymbol{x}_{\mathcal{A}_l} \leftarrow \boldsymbol{a}_{\mathcal{A}_l}$
    $\boldsymbol{s}_{\mathcal{I}\cup\mathcal{A}_l} \leftarrow \mathbf{0}$
    $\boldsymbol{t}_{\mathcal{I}\cup\mathcal{A}_u} \leftarrow \mathbf{0}$
    Compute $(\boldsymbol{x}_\mathcal{I}, s_{\mathcal{A}_u}, t_{\mathcal{A}_l})$ from (4.23) and (4.24)
    if $\boldsymbol{a} \preceq \boldsymbol{x} \preceq \boldsymbol{b}$ & $\boldsymbol{s} \succeq 0$ & $\boldsymbol{t} \succeq 0$ **then**
      $\boldsymbol{x}^* = \boldsymbol{x}$
      Solutionfound $\leftarrow 1$
    end if
    $\mathcal{A}_u = \mathcal{A}_u^+ \leftarrow \{i : x_i > b_i \parallel s_i > 0\}$
    $\mathcal{A}_l = \mathcal{A}_l^+ \leftarrow \{i : x_i < a_i \parallel t_i > 0\}$
    $\mathcal{I} = \mathcal{I}^+ \leftarrow \mathcal{C} \setminus \mathcal{A}_u^+ \setminus \mathcal{A}_l^+$
  end while
  return $\boldsymbol{x}^*$
end function

Remark 1 *It should be noted that the main calculation load of this method is matrix inversion for $\boldsymbol{Q}$. Due to the relatively small scale of the problem (6 dimensions) and the low number of iterations required to solve the problem, all calculations can be completed within one control period. To further reduce the computational burden, the problem* (3.21) *should be used. As we have mentioned before, for the problem* (3.21)*, the matrix $\bar{\boldsymbol{Q}}$ is constant and its inverse matrix can be calculated in advance. In fact, since the inverse matrix is known, which saves a lot of calculation effort, we can even go through all possible active sets to find the solution to the problem* (3.21)*. Although the computation time increases significantly, for some ill-conditioned problems, this method guarantees that the optimal solution will definitely be found within the*

determined time. The detail of realizing such an exhaustive method will be presented in the next chapter.

So far, after implementing this infeasible active set method, the optimal solution $\boldsymbol{x}^*$, which presents the insertion index of each arm, can be obtained. This solution can be directly applied to the sorting and modulation stage to realize the control of the MMC system. Note that the solution of these methods introduced in [46, 47, 51] can be directly expressed as

$$\boldsymbol{x}_{\mathrm{unc}} = -\boldsymbol{Q}^{-1}\boldsymbol{d}. \tag{3.29}$$

3.2.2.3 Voltage balancing and modulation method

The arm-balancing control introduced in Section 2.3.2.2 can be used to stabilize the MMC operation and generate the reference of the circulating current [27]. The individual balancing of each SM is achieved by the voltage sorting algorithm, which has been presented in Section 2.4.3. However, the insertion indices obtained by the modulated MPC scheme are not integers and thus some modifications have to be made before implementing the sorting algorithm.

According to the optimal solution $\boldsymbol{x}^*$, the number of SMs that remain inserted during one control period can be expressed as

$$n_{yx}^{\mathrm{inf}} = \mathrm{floor}(n_{yx}^*), \tag{3.30}$$

where n_{yx}^* is the element of $\boldsymbol{x}^*$ and the floor function will generate the greatest integer n_{yx}^{inf} which is less than or equal to n_{yx}^*. The fractional part of n_{yx}^*, which represents the duty cycle of the SM operating under the PWM mode, can be calculated as

$$d_{yx} = n_{yx}^* - n_{yx}^{\mathrm{inf}}. \tag{3.31}$$

The maximum number of inserted SMs in a control period can be expressed as

$$n_{yx}^{\mathrm{sup}} = \mathrm{ceil}(n_{yx}^*). \tag{3.32}$$

The ceiling function maps n_{yx}^* to the least integer greater than or equal to n_{yx}^*. n_{yx}^{sup} will be given to the voltage sorting algorithm to determine which SMs need to be inserted. n_{yx}^{inf} SMs will be inserted during the whole control period and the duty cycles of these SMs will be given 1. $N - n_{yx}^{\mathrm{sup}}$ SMs will be bypassed during the whole control period and the duty cycles of these SMs will be given 0. The state of one SM will change according to the duty cycle d_{yx}. When the duty cycle of all SMs is obtained, each SM will complete the modulation process according to its own duty cycle. Fig 3.2 shows the block diagram of the voltage sorting part and modulation part.

3.3 A computationally efficient way to realize FCS-MPC

The FCS-MPC method for the MMC system is essential to solve a QP problem with a discrete solution, which is also called an integer quadratic programming (IQP) problem, in each control period. For this problem, it is impossible to find this discrete solution (or control options) through an exhaustive method in real time. This is because the total number of the possible

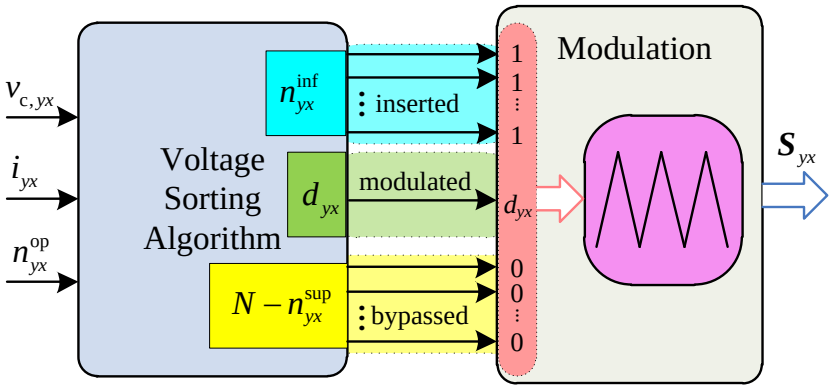

Figure 3.2: Block diagram of the voltage balancing algorithm and modulation method.

insertion index combinations is $(N+1)^6$, which is a big number when N is large. A natural way to reduce the computational burden is to decrease the number of insertion index combinations in the control set that need to be evaluated. Therefore, the basic idea of the proposed method is to find a reduced control set based on the solution of the slack problem of this IQP problem. Note that this slack problem has already been solved in Section 3.2.2. Based on the solution $\boldsymbol{x}^*$, an reduced control set can be constructed as follows:

$$\begin{aligned} &n_{ua} \in \{\lfloor x_1^* \rfloor, \lceil x_1^* \rceil\}, \quad n_{la} \in \{\lfloor x_2^* \rfloor, \lceil x_2^* \rceil\}, \\ &n_{ub} \in \{\lfloor x_3^* \rfloor, \lceil x_3^* \rceil\}, \quad n_{lb} \in \{\lfloor x_4^* \rfloor, \lceil x_4^* \rceil\}, \\ &n_{uc} \in \{\lfloor x_5^* \rfloor, \lceil x_5^* \rceil\}, \quad n_{lc} \in \{\lfloor x_6^* \rfloor, \lceil x_6^* \rceil\}, \end{aligned} \tag{3.33}$$

where $\lfloor x \rfloor$ taking the nearest integer that is less than x and $\lceil x \rceil$ takes the smallest integer which is greater than x. Note that there are two special cases, i.e. $x = N$ and $x = 0$. If $x = N$, then $\lceil x \rceil = N$ and $\lfloor x \rfloor = N - 1$. If $x = 0$, then $\lceil x \rceil = 1$ and $\lfloor x \rfloor = 0$.

In this method, the insertion indices will not take values from 0 to N, but will select values from this reduced control set. Thus, the cost function only needs to evaluate 2^6 possible combinations to find the best combination of insertion indices. Moreover, the calculation load of this method is no longer related to the number of SMs in each arm.

Remark 2 *It should be noted that we can also use the unconstrained solution $\boldsymbol{x}_{\text{unc}}$ instead of using the optimal solution $\boldsymbol{x}^*$ to establish a similar reduced control set. However, such a method has its own limitations in some cases. For example, when the MMC operates in the high modulation index condition or during transients, the performance of this method will deteriorate.*

Compared with other existing FCS-MPC methods with reduced calculation complexity [40, 41], the proposed approach is a more general solution. Existing methods are roughly based on the information about the ac output voltage level and the desired change direction of the circulating current to narrow the range of the insertion indices. Therefore, these methods have great limitations. If the form of the cost function changes, such as there is no circulating current

term [36,52], the control performance of these methods will deteriorate or even fail. In contrast, the proposed method does not have these limitations.

3.4 Validations

The parameters of the MMC system with RL load have been given in Section 2.5. The sampling interval of both modulated MPC scheme and FCS-MPC scheme is 100 µs. In this section, the experimental results of both the modulated MPC and FCS-MPC will be presented to verify the effectiveness of the proposed method.

3.4.1 Validation of the modulated MPC

In this section, the conventional modulated MPC method [47,51] and the proposed method will be compared in the experiment.

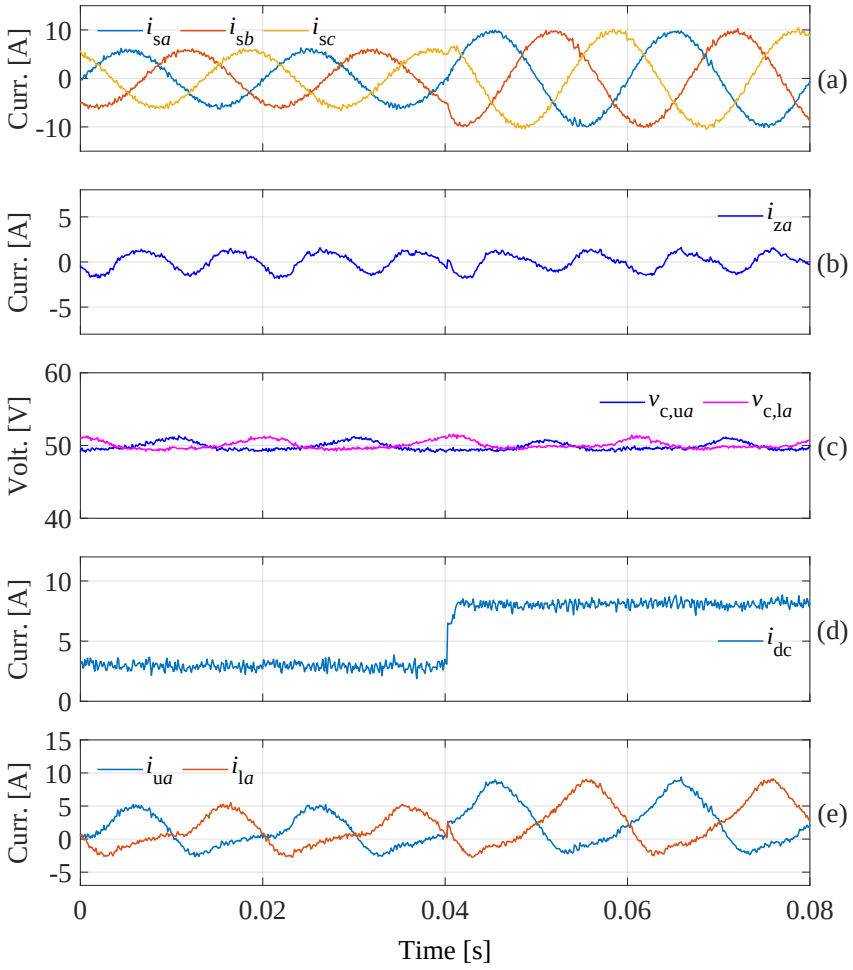

Figure 3.3: Step change in ac currents with the proposed modulated MPC at 50 Hz.

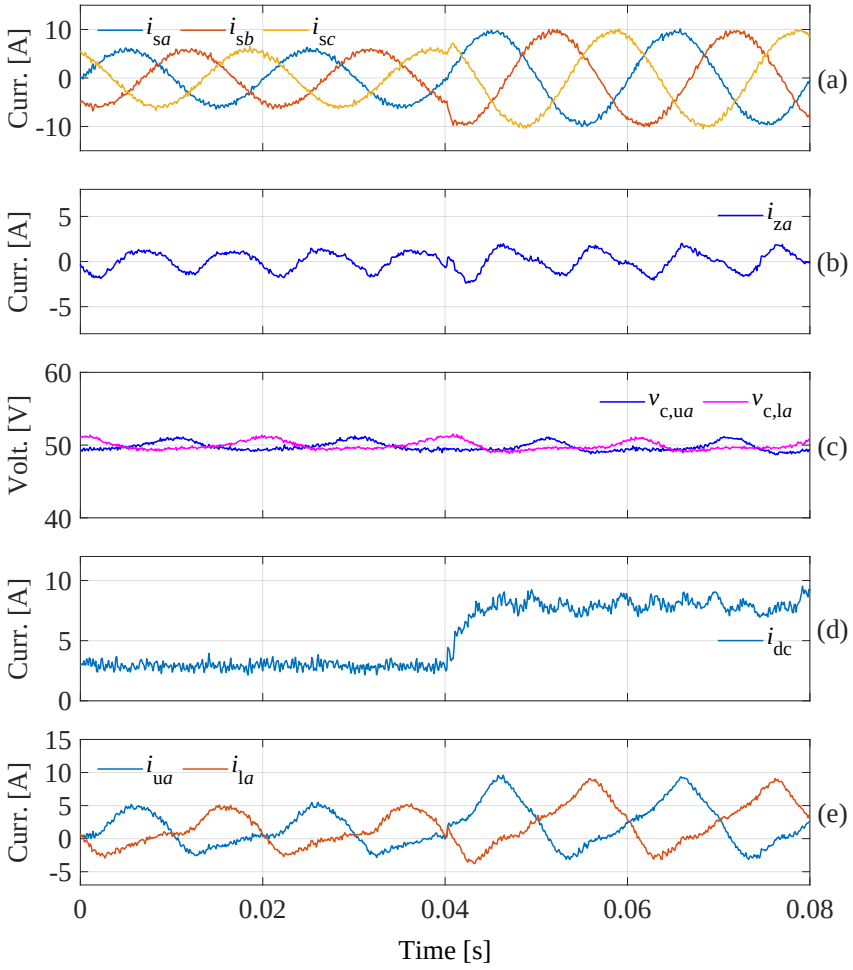

Figure 3.4: Step change in ac currents with the conventional modulated MPC at $50\,\mathrm{Hz}$.

The experimental results of the proposed method under the step change in the amplitude (from $6\,\mathrm{A}$ to $10\,\mathrm{A}$) of the ac output currents are shown in Fig. 3.3. Fig. 3.3(a) presents the three-phase ac-side currents (i_{sa}, i_{sb} and i_{sc}) under such a related change. Fig. 3.3(b) shows the circulating current of phase a (i_{za}). As the low-pass/notch filters are not applied in the energy control part, an obvious second-order component appears in the circulating current. The capacitor voltages of the upper and lower arm in leg a ($v_{\mathrm{c,ua}}$ and $v_{\mathrm{c,la}}$) is shown in Fig. 3.3(c). It can be seen that the SM capacitor voltages in both the upper and lower arms are well balanced and the ripple magnitude of all the capacitor voltages is small, which is less than 10% of the reference value. Fig. 3.3(d) shows the dc-link current (i_{dc}). Since the circulating current and dc-link current are decoupled, the fluctuation in the circulating current does not appear in the dc-link current. At last, the arm currents are presented in Fig. 3.3(e).

From Fig. 3.3, it can be seen that the dynamic response of ac-side currents, circulating currents and the dc-link current is very fast. In addition, the response rate of these variables is different. This is because these control variables are decoupled due to the use of the three-phase model of the MMC. In this way, the MMC can be seen as a buffer between the ac side and the dc side.

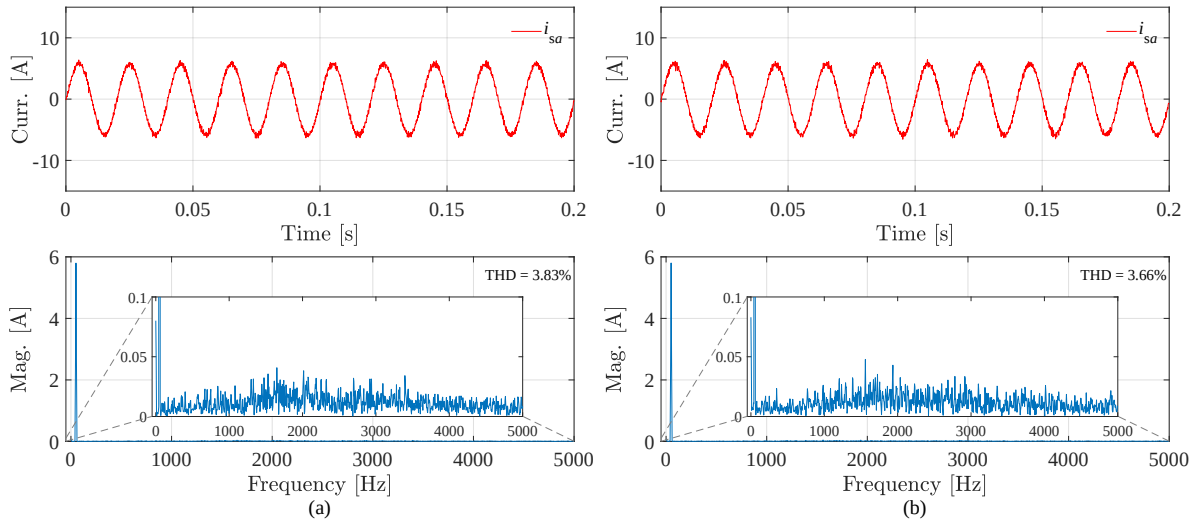

Figure 3.5: FFT analysis of the output current i_{sa} when the amplitude is 6 A. (a) Conventional method. (b) Proposed method.

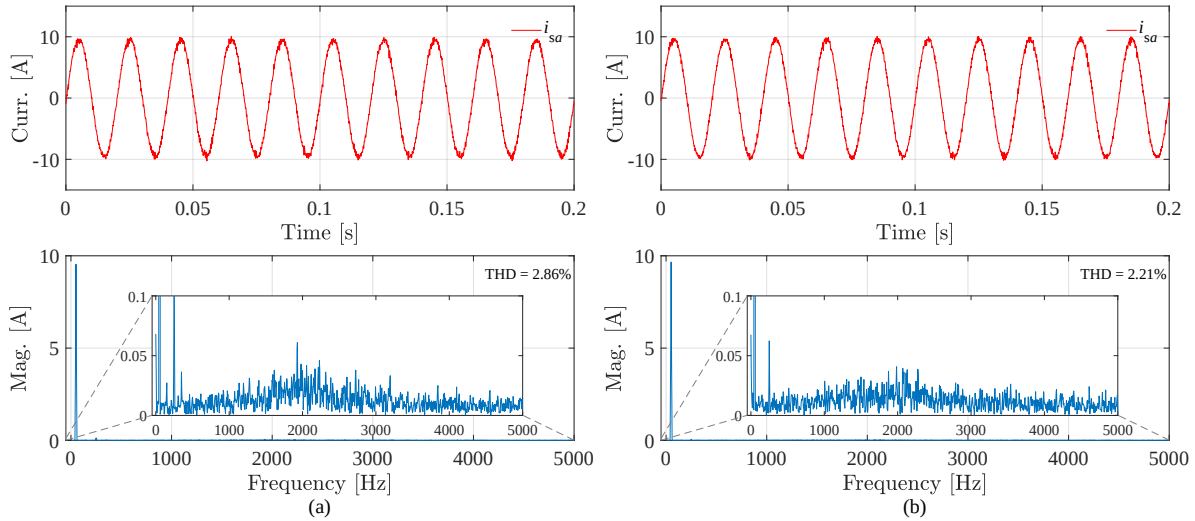

Figure 3.6: FFT analysis of the output current i_{sa} when the amplitude is 10 A. (a) Conventional method. (b) Proposed method.

The dynamic performance of the conventional modulated MPC scheme has been provided in Fig. 3.4. It can be seen that a comparable steady-state performance can be achieved by using the conventional modulated MPC method when the amplitude of the ac-side currents is 6 A. However, the poor dynamic response is observed in both ac-side currents and dc-link current during transients ($t = 0.04$ s). Besides, there are obvious fluctuations in the dc-link current when the amplitude of the ac-side currents is 10 A. Both the transient performance and the steady-state performance under high modulation index can indicate that the proposed modulated MPC method is superior to the conventional method, which validates the analysis in Section 3.2.1.

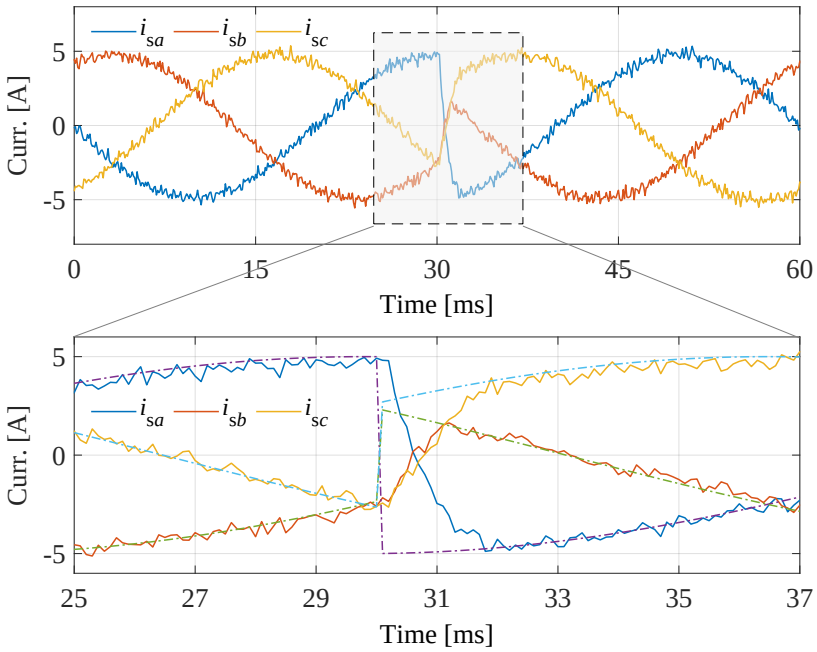

Figure 3.7: Dynamic performance in the three-phase currents of the conventional method when the phase angle changes by $180°$.

Fig. 3.5 and 3.6 show the output current i_{sa} and its spectrum under different load conditions. FFT results can be used to evaluate the steady-state performance in the output current of these two methods. From Fig. 3.5, it can be seen that both the conventional method and the proposed method show similar performance in the output current at $6\,\mathrm{A}$. However, when the amplitude increases to $10\,\mathrm{A}$ in Fig. 3.6, which means that the MMC operates under the high modulation index, the spectrum and THD results show that the proposed method is better than the conventional method, which is consistent with the previous analysis in 3.2.1. The THD result of the proposed method is only 2.21%, which is an improvement of nearly 23% compared to the THD of 2.86% for the conventional method. It should be noted that an obvious 5^{th} harmonic component can be found in Fig. 3.6(a), which represents that the conventional method cannot fully utilize the output voltage of the MMC. This is due to the saturation of the unconstrained solution. Instead, because the proposed method uses the optimal solution, the 5^{th} harmonic component in the output current is not as pronounced as in the conventional method.

The experiments of the step change in the phase angle of the ac currents have also been designed to test the dynamic performance of these two methods. The phase angle will change by $180°$ at $30\,\mathrm{ms}$ and the three-phase output currents of the conventional and proposed methods are shown in Fig. 3.7 and 3.8, respectively. The dynamic response of the output currents is almost the same for both methods. However, the dc-link current of these two methods has different performance under such a transient process, which is shown in Fig. 3.9. It can be seen from Fig. 3.9(a) that the dc-link current with the conventional method has a considerable drop in the transient process. Instead, we cannot observe such a drop in the dc-link current for the proposed method from Fig. 3.9(b). The experimental results verify the effectiveness and superiority of the proposed method.

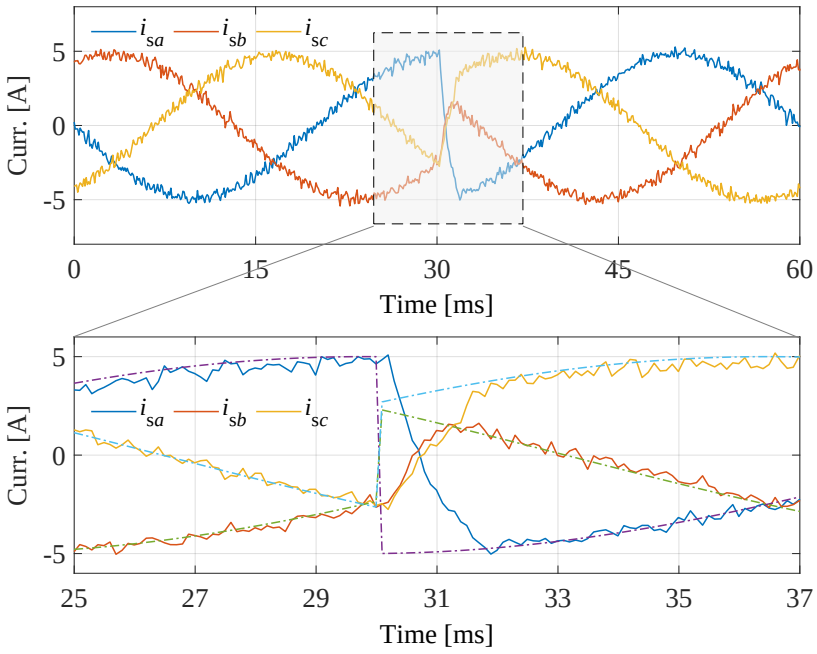

Figure 3.8: Dynamic performance in the three-phase currents of the proposed method when the phase angle changes by 180°.

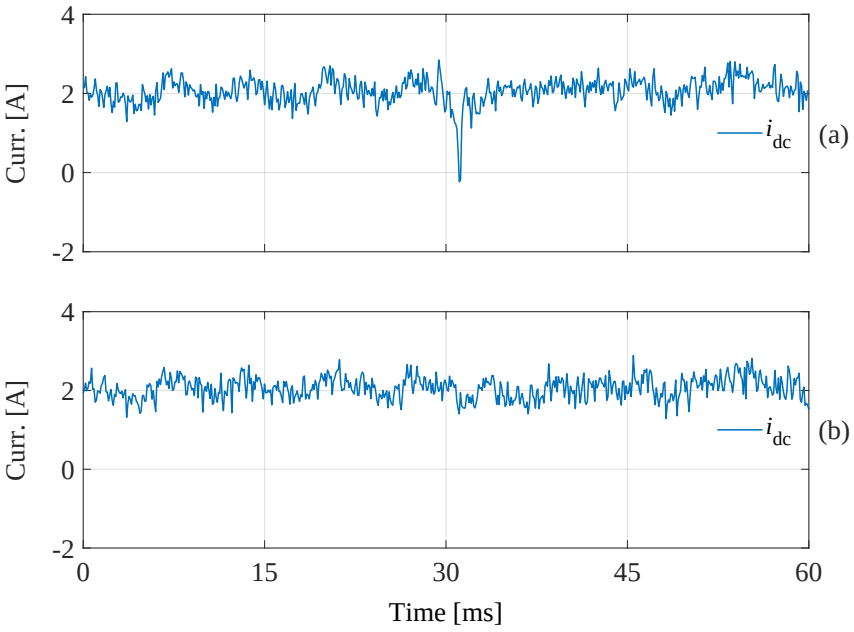

Figure 3.9: Dynamic performance in the dc-link current of the conventional method and the proposed method when the phase angle changes by 180°. (a) Conventional method. (b) Proposed method.

In conclusion, when the MMC operates under the low modulation index condition, the conventional modulated MPC method and the proposed method present similar steady-state per-

formance. This is because under this condition, the unconstrained solution is equivalent to the optimal solution in problem (3.19) in most cases. Therefore, in this case, the effect of weighting factors and the common-mode voltage can be neglected. However, when the MMC system is in transient or high modulation index, the performance of the conventional method is poor. This is because the conventional approach does not consider the actual limitations of the control system, but assumes that the system can regulate all control variables to their desired values in one step. The role of weighting factors and the effect of the common-mode voltage cannot be ignored in this case. Due to the comprehensive consideration of these effects, the proposed modulated MPC method can achieve both steady-state and dynamic performance improvements.

3.4.2 Validation of FCS-MPC

In this part, the proposed FCS-MPC method in Section 3.3 will be verified from simulation and experimental results. Moreover, the FCS-MPC scheme with the unconstrained solution, namely the simplified FCS-MPC in this part, is also tested as a comparison.

3.4.2.1 Simulation results for the MMC operating in the rectifier mode

Table 3.1: Parameters for the simulation

Parameter	Symbol	Value
DC link voltage	V_{dc}	$1.5\,\mathrm{kV}$
AC source voltage	e_g	$700\,\mathrm{V}$
Number of Model on each Arm	N	10
SM Capacitance	C_{ci}	$1.867\,\mathrm{mF}$
Arm Inductance	L	$5\,\mathrm{mH}$
AC-side Resistance	R_s	$0.2\,\Omega$
AC-side Inductance	L_s	$2\,\mathrm{mH}$

A three-phase MMC system is constructed on MATLAB/Simulink to verify the proposed FCS-MPC method. The simulation results of the MMC operating in the rectifier mode are shown in this subsection. The parameters are listed in Table 3.1.

The simulation results of the dc-link voltage reference stepping of the proposed FCS-MPC method and the simplified FCS-MPC method are shown in Fig. 3.10 and Fig. 3.11, respectively. Fig. 3.10(a) and 3.11(a) show the three-phase ac-side currents under such a related change. Fig. 3.10(b) and 3.11(b) present the circulating current of leg a, which follows its reference during the steady and transient state. The capacitor voltages of the upper and lower arm in leg a for both methods are shown in Fig. 3.10(c) and 3.11(c). Fig. 3.10(d) and 3.11(d) give the dc-link voltage waveform. Accordingly, the dc-link current is presented in Fig. 3.10(e) and 3.11(e). At last, the iterations of the proposed method and the simplified method are shown in Fig. 3.10(f) and 3.11(f).

It can be seen that the performance on ac-side currents, circulating currents, dc-link current and dc-link voltage of the proposed MPC is superior to the simplified MPC when V_{dc} decreases from $1.5\,\mathrm{kV}$ to $1.2\,\mathrm{kV}$. As it has been mentioned in Section 3.3, the performance of the simplified method will deteriorate when the MMC operates at a high modulation index. In this case,

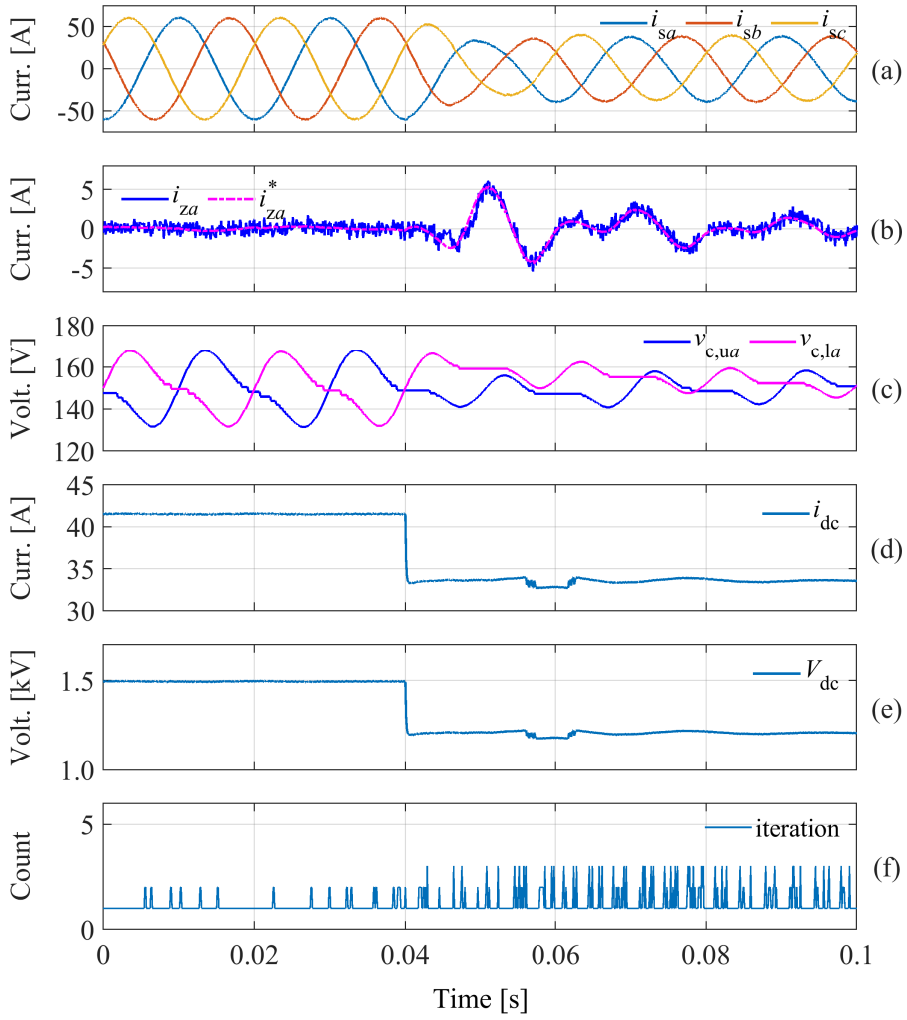

Figure 3.10: Step changes in V^*_{dc} with proposed MPC.

the ac-side currents have been significantly distorted. Besides, the circulating current cannot follow its reference perfectly. Instead, it oscillated around the reference. Also, some spikes appear on the dc-link voltage and dc-link current at a steady state. This is because the unconstrained solution does not consider the different weights among these control objectives. Without considering the actual meaning of the insertion index (it should be less than N and larger than 0), these control variables would reach their reference values in one control period by applying the unconstrained solution. It means that the simplified MPC does not put more weight on the more important control objectives to achieve better performance. Therefore, when the dc-link voltage has become $1.2\,\mathrm{kV}$, the performance of the simplified method is not ideal.

3.4.2.2 Experimental results for the MMC operating in the inverter mode

The calculation time and computational burden of the proposed method and simplified method are presented in Table 3.2. It can be seen that the calculation time of the proposed method only increases 1µs compared with the simplified method in our platform. The experimental results

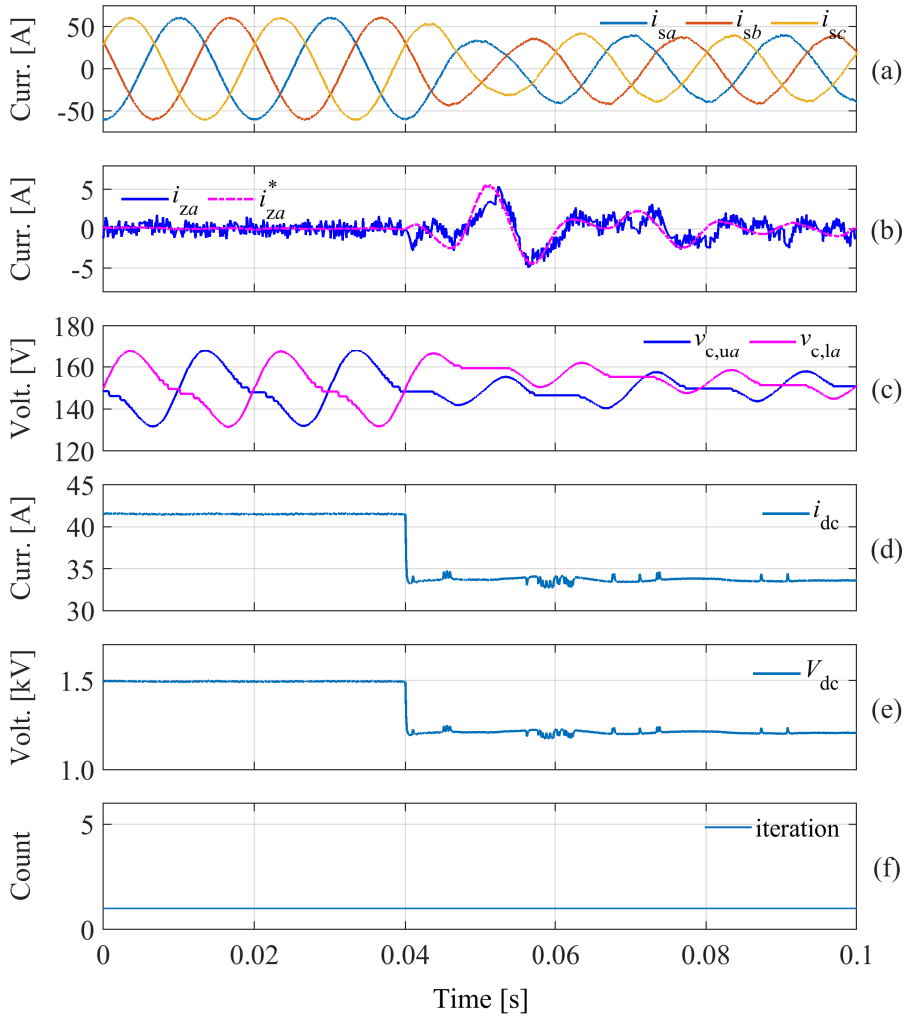

Figure 3.11: Step changes in V^*_{dc} with simplified MPC.

Table 3.2: Calculation time of MPC methods

Method	Calculation time (Maximum)	Computational burden (Maximum)
Proposed MPC	19.5µs	6 iterations + 64 combinations
Simplified MPC	18.5µs	1 iteration + 64 combinations

of the proposed method and the simplified method under the step change in the amplitude of the ac-side currents (from $6\,\mathrm{A}$ to $10\,\mathrm{A}$) are shown in Fig. 3.12 and Fig. 3.13, respectively. The THD results of the output currents for the proposed method are 4.17% at $6\,\mathrm{A}$ and 3.38% at $10\,\mathrm{A}$, while the THD of the simplified method is 4.21% at $6\,\mathrm{A}$ and 3.46% at $10\,\mathrm{A}$. The experimental results show a comparable performance for the proposed method and the simplified method. In fact, due to the small number of SMs in the experimental platform ($N = 2$), the comparison of

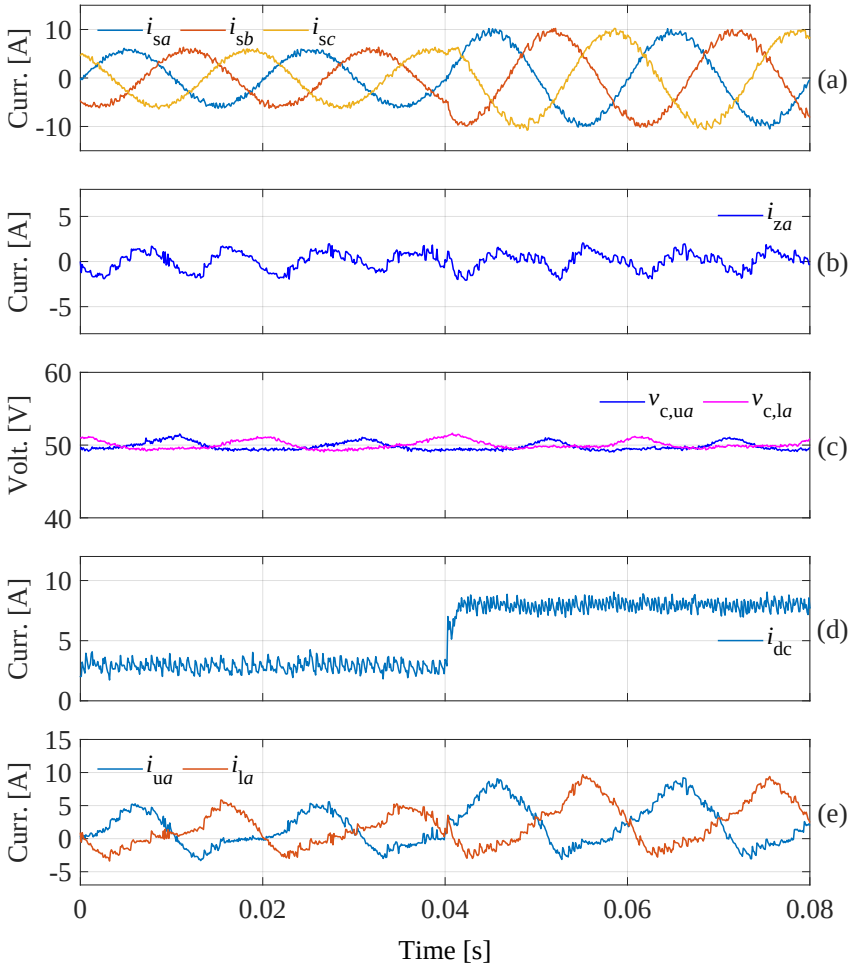

Figure 3.12: Step change in output currents with proposed MPC.

these methods is not prominent.

It should be noted that the performance of the simplified method slightly deteriorates when the amplitude of the output currents is $10\,\mathrm{A}$ due to the high modulation index. This is consistent with the previous analysis. Besides, the simulation and experimental results verify that a computationally efficient FCS-MPC scheme can be achieved by evaluating a reduced control set, which can be established by using the discrete solution around the optimal solution. The experimental results also show that the steady-state performance of the MMC system with the FCS-MPC scheme is inferior to that with the modulated MPC scheme under the same sampling frequency. However, the switching frequency of the FCS-MPC method is much lower than that of the modulated MPC method. For example, when the output currents are $10\,\mathrm{A}$, the average switching frequency of the MMC with the modulated MPC scheme is about $8.6\,\mathrm{kHz}$, while that of the FCS-MPC scheme is only $1.8\,\mathrm{kHz}$. Therefore, the switching losses of FCS-MPC are much lower than that of the modulated MPC, which is a very good characteristic for high-power converters. In fact, the main benefit of FCS-MPC compared to the modulated method is that it can achieve a low average switching frequency under the relatively high sampling frequency and thus it can achieve a better control performance and lower power losses.

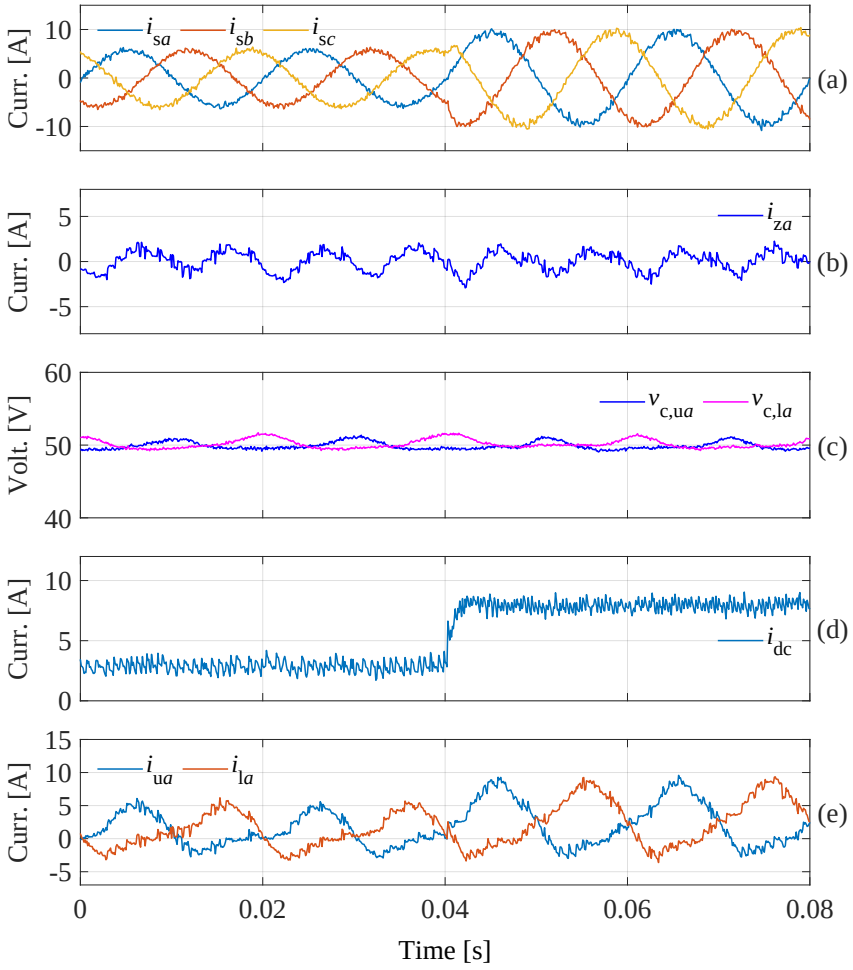

Figure 3.13: Step change in output currents with simplified MPC.

3.5 Summary

In this chapter, the existing modulated MPC method has been first discussed. It is pointed out that the essence of such methods is to solve the unconstrained solution of an optimization problem. Thus, the limitations of the existing method are obvious. That is when the MMC operates in the high modulation index or transient state, this unconstrained solution cannot fully consider the importance of different control variables. In order to solve the problems brought by the existing methods, the modulated MPC method with a bound-constrained QP solver has been proposed. Compared with the existing methods, the proposed method performs better in the case of transients and high modulation index due to the use of an optimal solution, which considers the effect of different weights on different control objectives. Meanwhile, this optimal solution obtained by the proposed modulated MPC method can be used to establish a reduced control set to realize the FCS-MPC scheme. It can be seen that instead of evaluating all the possible $(N+1)^6$ insertion index combinations, the proposed FCS-MPC scheme only needs to evaluate 2^6 insertion index combinations and the calculation load of this method is no longer related to the number of SMs per arm. Thus, it can be said that the proposed method is a

promising solution for the three-phase model based FCS-MPC scheme. At last, the effectiveness and superiority of the proposed methods are verified by simulation and experimental results.

CHAPTER 4

Model predictive control for modular multilevel converters operating in a wide frequency range

4.1 Introduction

The modular multilevel converter (MMC) has become one of the most promising converter topologies in medium/high voltage applications over the past decades [8]. In comparison with other multilevel converters, MMC shows better modularity and scalability [54]. It employs a cascaded connection of sub-modules (SMs) to achieve the desired output voltage while producing a high-quality multilevel output voltage waveform. With such a modularity structure, a very low total harmonic distortion (THD) of grid currents and switching frequency can be achieved [55]. Due to these excellent features, it has been widely used in high-voltage direct current transmission (HVDC) [10,11] and static synchronous compensator (STACOM) [14,15].

Although MMC has these outstanding advantages, the applications of MMC-based medium-voltage (MV) motor drives [12, 13] are less popular due to the unavoidable fluctuation of the SM capacitor voltage, especially under low-frequency conditions. Without some special control methods, the voltage fluctuation is directly proportional to the load currents and inversely proportional to the output frequency, which has been well-discussed in [56, 57]. This inherent drawback hinders the widespread application of MMC in MV motor drives.

To deal with this problem, many efforts have been made and the measures can be roughly divided into three groups. The first one is called the high-frequency circulating current injection method [58–61]. A first attempt to deal with the low output frequency operation of the MMC has been proposed in [58]. In this method, the amplitude of the arm energy ripple depends on the frequency of the injected common-mode voltage instead of the output current frequency. In [59], a square-wave common-mode voltage and a sinusoidal circulating current associated with a third harmonic component have been proposed to reduce the peak value of the circulating current and the SM capacitor voltage ripple. In [60], the square-wave circulating currents combined with a square-wave common-mode voltage have been used to refrain the low-frequency

fluctuation. An improved circulating current injection method has been proposed in [56]. In this method, the capacitor voltage ripple is maintained at a reasonable range and thus the circulating currents can be further reduced. However, these injection methods require a trade-off between the performance of the output currents (an adequate modulation range should be maintained) and the suppression of the capacitor voltage ripple (the injected common-mode voltage should be as high as possible to avoid a large circulating current). Thus, the steady-state performance of the output current may deteriorate especially at high modulation indices. Besides, for the injection method, an additional switching process between the low-frequency operation mode and the high-frequency operation mode should be considered, which increases the complexity of the control structure.

The second approach is the quasi-two-level mode operation [62–65]. This method mimics the standard two-level voltage source inverter (VSI) to reduce the charging or discharging time of the MMC branches/arms. Therefore, the quasi-two-level mode operation can achieve low branch energy variations and thus it becomes a suitable option for MV low-speed motor drive applications [65]. In [62], an high-frequency (HF) modulator is added to control the circulating current and balance the branch energy. A delay control method to balance branch energy and achieve the quasi-two-level mode operation is proposed in [63]. The authors in [64] propose an arm current commutation control method to achieve the balance control of the branch energy during the commutation process for the MMC operating at quasi-two-level mode. However, these methods sacrifice the multilevel voltage waveform for the MMC, which will lead to high torque ripples for the MV motors. In addition, these methods are more suitable for the low-frequency operation mode of MMC and thus the switching process is also required.

The last category is to use a modified MMC topology to decrease the voltage ripple of SM capacitors [13, 66, 67]. The idea behind these methods is to introduce new current paths [66] or reduce the dc-link voltage [13, 67]. However, these methods will significantly increase the costs of switching devices.

In recent years, the MPC method as an alternative control scheme for the MMC system has drawn more attention due to its prominent features, such as its straightforward implementation, ability to control multiple objectives in a single cost function, excellent dynamic response and easy handling of nonlinearities and constraints. In addition, compared with modulation-based methods, MPC can achieve a lower average switching frequency at the same sampling frequency, which is very suitable in high power applications. Most of the research studies focus on reducing the computational complexity of MPC for the MMC [36, 37, 41]. However, due to the lack of the common-mode voltage in the model of MMC, these methods cannot use the common-mode voltage to reduce the capacitor voltage ripple like the injection methods. The MPC method considering the effect of common-mode voltage can be found in [42, 43, 53]. Using the MPC scheme with the common-mode voltage to reduce the capacitor voltage ripple has been proposed in [53]. This paper reveals that a small capacitor voltage ripple and circulating current can be achieved by considering the common-mode voltage in the prediction model of the output current. However, this method is difficult to achieve low-speed/zero-speed control for the MMC-based motor drive system. In fact, to the best of the author's knowledge, little or no effort has been made to develop an MPC method for the MMC operating over a wide frequency range.

In this chapter, an FCS-MPC method for the MMC operating in a wide frequency range has been proposed first. Unlike the cost function used in conventional FCS-MPC methods [25,36], a

novel cost function has been designed to realize the output current control, dc-link current control, and voltage balancing control over a wide frequency range. The proposed method not only achieves satisfactory performance at low frequencies but also works effectively at high frequencies and thus it is particularly suitable for MMC-based motor drive applications. In contrast, the previous MPC methods introduced in [25, 36] cannot realize the low/zero frequency motor control driven by MMC. Besides, unlike the high-frequency injection method, which requires complicated consideration of the modulation range and the injected common-mode voltage, the proposed method can easily guarantee the performance of output currents and the suppression of capacitor voltage ripples. Moreover, in comparison with these injection methods, the proposed method does not require the division to obtain the magnitude of the injected circulating currents, but directly adjusts the instantaneous power to regulate the arm energy. Thus, even if the MMC operates at low frequencies with a relatively high modulation index, the amplitude of the circulating current can be limited while the suppression of the capacitor voltage can be guaranteed. Also, the control structure of the proposed method is simple as the switching process between different control schemes is not required. The experimental results validate the effectiveness and superiority of the proposed FCS-MPC method with the novel cost function. In addition, as the FCS-MPC method often brings a heavy computational burden, the modulated MPC method based on this novel cost function has also been developed in this chapter. In this modulated MPC method, an exhaustive active set method has been proposed to obtain the optimal insertion index. Although the proposed method will take a longer time compared with the traditional active set method or infeasible active set method introduced in Chapter 3, it guarantees that the optimal solution can always be obtained and the worst calculation step/time can be determined. Moreover, this method is a kind of parallel algorithm and some calculations can be taken offline to further reduce the computational load. It can be concluded that by using this method, the worst calculation time can be determined and it is independent of the number of SMs per arm. At last, comparative experimental results have been provided to verify the superiority of this proposed modulated MPC method.

4.2 MPC with a newly designed cost function for MMCs

The mathematical model and power analysis of the MMC can be found in Section 2.3.2. The principle of the MPC method for MMCs has also been discussed in Section 2.4. As analyzed in Section 2.3.2.2, the energy response caused by $v_{x\mathrm{N}}i_{zx}$ is slow due to the long fundamental period and the fundamental-frequency component in the SM capacitor voltages is inversely proportional to the output frequency when the conventional energy balancing control scheme is applied. Therefore, the conventional MPC method with the energy balancing controller is not suitable for the MMC driving MV motors.

An alternative way to regulate the arm energy is to directly control the corresponding instantaneous power and the proposed method is based on this principle. When the instantaneous power P_x^{Δ} (2.26) can be controlled, the differential energy between the upper and lower arms can be regulated indirectly. It can be seen that when the energy of the upper arm $E_{\mathrm{u}x}$ is greater than the energy of the lower arm $E_{\mathrm{l}x}$, the instantaneous power in (2.26) could be regulated less than 0 so that the energy of the lower arm increases faster or decreases slower than the energy of the upper arm and finally catches up with the energy of the upper arm, that is, in case

$E_{\mathrm{u}x} - E_{\mathrm{l}x} > 0$, then $P_x^{\Delta} < 0$.

In order to realize the above-mentioned idea, the cost function is designed as follows:

$$\begin{aligned} J =& w_1 \left\| \boldsymbol{i}_{\mathrm{s}}^* - \boldsymbol{i}_{\mathrm{s}}(k+1) \right\|_2^2 + w_3 \left\| i_{\mathrm{dc}}^* - i_{\mathrm{dc}}(k+1) \right\|_2^2 \\ & + w_2 \left\| \boldsymbol{i}_{\mathrm{z}}(k+1) \right\|_2^2 + \boldsymbol{w}_{\mathrm{t}}^{\mathrm{T}} \boldsymbol{i}_{\mathrm{z}}(k+1) + w_{\mathrm{com}} p_{\mathrm{com}} + \boldsymbol{w}_{\mathrm{d}}^{\mathrm{T}} \boldsymbol{p}_{\mathrm{d}} \end{aligned} \tag{4.1}$$

where

$$\boldsymbol{i}_{\mathrm{s}}(k+1) = \begin{bmatrix} i_{\mathrm{s}a}(k+1) & i_{\mathrm{s}b}(k+1) & i_{\mathrm{s}c}(k+1) \end{bmatrix}^{\mathrm{T}};$$

$$\boldsymbol{i}_{\mathrm{z}}(k+1) = \begin{bmatrix} i_{\mathrm{z}a}(k+1) & i_{\mathrm{z}b}(k+1) & i_{\mathrm{z}c}(k+1) \end{bmatrix}^{\mathrm{T}};$$

$$\boldsymbol{w}_{\mathrm{t}} = \begin{bmatrix} w_{\mathrm{t}a} & w_{\mathrm{t}b} & w_{\mathrm{t}c} \end{bmatrix}^{\mathrm{T}} \text{ with } w_{\mathrm{t}x} = c_1(v_{\mathrm{u}x}^{\Sigma} + v_{\mathrm{l}x}^{\Sigma} - v_{\mathrm{ave}}^{\Sigma}),$$

$$v_{\mathrm{ave}}^{\Sigma} = \sum_{x=a,b,c} \frac{v_{\mathrm{u}x}^{\Sigma} + v_{\mathrm{l}x}^{\Sigma}}{3}, \quad v_{\mathrm{u}x}^{\Sigma} = \sum_{i=1}^{N} v_{\mathrm{c,u}x}^{i}, \quad v_{\mathrm{l}x}^{\Sigma} = \sum_{i=1}^{N} v_{\mathrm{c,l}x}^{i};$$

$$w_{\mathrm{com}} = c_2 v_{\mathrm{com}} \text{ with } v_{\mathrm{com}} = \sum_{x=a,b,c} \frac{v_{\mathrm{u}x}^{\Sigma} - v_{\mathrm{l}x}^{\Sigma}}{3};$$

$$p_{\mathrm{com}} = \sum_{x=a,b,c} \left(v_{\mathrm{u}x}(k) - v_{\mathrm{l}x}(k) \right) i_{\mathrm{z}x}(k+1) - 2 v_{\mathrm{NO}}(k) i_{\mathrm{dc}}(k);$$

$$\boldsymbol{w}_{\mathrm{d}} = \begin{bmatrix} w_{\mathrm{d}a} & w_{\mathrm{d}b} & w_{\mathrm{d}c} \end{bmatrix}^{\mathrm{T}} \text{ with } w_{\mathrm{d}x} = c_3(v_{\mathrm{u}x}^{\Sigma} - v_{\mathrm{l}x}^{\Sigma} - v_{\mathrm{com}});$$

$$\boldsymbol{p}_{\mathrm{d}} = \begin{bmatrix} p_{\mathrm{d}a} & p_{\mathrm{d}b} & p_{\mathrm{d}c} \end{bmatrix}^{\mathrm{T}} \text{ with}$$

$$p_{\mathrm{d}x} = \frac{V_{\mathrm{dc}} i_{\mathrm{s}x}(k)}{2} - \left(v_{\mathrm{l}x}(k) - v_{\mathrm{u}x}(k) \right) \left(\frac{i_{\mathrm{dc}}(k)}{3} + i_{\mathrm{z}x}(k+1) \right).$$

x represents the phase a, b or c. w_1, w_2 and w_3 are weighting factors. c_1, c_2 and c_3 are adjustable coefficients. $\boldsymbol{i}_{\mathrm{s}}^* = \begin{bmatrix} i_{\mathrm{s}a}^* & i_{\mathrm{s}b}^* & i_{\mathrm{s}c}^* \end{bmatrix}^{\mathrm{T}}$ is the reference of ac-sie currents. The first term in the cost function (4.1) represents the tracking error of the output currents. The second term is used to control the dc-link current and its reference can be obtained in Fig. 2.6. The third term is used to penalize the circulating currents. It should be noted that this term in the proposed method is necessary. It can not only suppress circulating currents but also restrain the last three terms. Without this term, the last three terms will lead to an unbounded circulating current, which results in an unstable system.

In the fourth term, $w_{\mathrm{t}x}$ is not a constant value. It is related to the difference between the average phase energy of the MMC ($v_{\mathrm{ave}}^{\Sigma}$) and the total energy of the phase x ($v_{\mathrm{u}x}^{\Sigma} + v_{\mathrm{l}x}^{\Sigma}$). As it has been discussed in (2.25), the circulating current $i_{\mathrm{z}x}$ can be used to control the energy in phase x when $i_{\mathrm{z}x}$ has the dc component. For example, $w_{\mathrm{t}x} < 0$ indicates that the total energy/voltage in phase x is less than the average energy/voltage of MMC. In this case, more power should flow into phase x, that is $P_x^{\Sigma} > 0$ in (2.25). As we know, the MPC method tends to choose the control option which minimizes the cost function. In this case ($w_{\mathrm{t}x} < 0$), in order to minimize the cost function, the algorithm tends to choose the control option which makes the term $w_{\mathrm{t}x} i_{\mathrm{z}x}(k+1) < 0$, which means $i_{\mathrm{z}x}(k+1) > 0$. In fact, $i_{\mathrm{z}x}(k+1) > 0$ cannot completely ensure $P_x^{\Sigma} > 0$. If $P_x^{\Sigma} < 0$, $w_{\mathrm{t}x}$ will become more negative and the term $w_{\mathrm{t}x} i_{\mathrm{z}x}(k+1)$ will be more important in the cost function, which implies that the more positive $i_{\mathrm{z}x}(k+1)$ is, the smaller the cost function will be. Thus, in this case, the circulating current will continue to increase. When $i_{\mathrm{z}x}(k+1)$ is large enough, P_x^{Σ} will be greater than 0 and the total energy/voltage in phase x will approach the average energy/voltage of the MMC.

Similarly, p_{com} in the cost function represents the instantaneous power equivalent to (2.28). Thus, the term $w_{\mathrm{com}}p_{\mathrm{com}}$ can eliminate the overall errors between the upper and lower arm energy. $\boldsymbol{p}_{\mathrm{d}x}$ represents the differential power, which is corresponding to (2.26). Therefore, the last term $\boldsymbol{w}_{\mathrm{d}x}^{\mathrm{T}}\boldsymbol{p}_{\mathrm{d}x}$ is used to regulate the differential energy between the upper arm and lower arm. These two terms ($w_{\mathrm{com}}p_{\mathrm{com}}$ and $\boldsymbol{w}_{\mathrm{d}x}^{\mathrm{T}}\boldsymbol{p}_{\mathrm{d}x}$) are designed based on the same principle as $w_{\mathrm{t}x}i_{\mathrm{z}x}(k+1)$.

Remark 3 *It is worth noting that the proposed method also allows the following case to exist, that is* $w_{\mathrm{t}x}i_{\mathrm{z}x}(k+1) > 0$, $w_{\mathrm{com}}p_{\mathrm{com}} > 0$ *and* $\boldsymbol{w}_{\mathrm{d}x}^{\mathrm{T}}\boldsymbol{p}_{\mathrm{d}x} > 0$. *This is because there are multiple control objectives in the cost function, and thus it is difficult to guarantee that these terms will always be less than* 0. *Take the last term* $\boldsymbol{w}_{\mathrm{d}x}^{\mathrm{T}}\boldsymbol{p}_{\mathrm{d}x}$ *as an example. As* $\boldsymbol{w}_{\mathrm{d}x}^{\mathrm{T}}\boldsymbol{p}_{\mathrm{d}x} > 0$, *the absolute value of* $\boldsymbol{w}_{\mathrm{d}x}$ *will increase, which will result in a larger penalty for* $\boldsymbol{p}_{\mathrm{d}x}$. *Therefore, the magnitude of* $\boldsymbol{p}_{\mathrm{d}x}$ *will decrease, which means that the power that causes the differential energy* ($v_{\mathrm{u}x}^{\Sigma} - v_{\mathrm{l}x}^{\Sigma} - v_{\mathrm{com}}$) *change has been compensated partly or completely. In fact, the last three terms can be regarded as the form of* $e\dot{e}$, *where* e *represents the error and* $\dot{e}$ *is the derivative of* e. *In this application,* e *represents energy/voltage error and* $\dot{e}$ *is the corresponding power.*

In the proposed cost function, there are 6 coefficients (w_1, w_2, w_3, c_1, c_2, c_3) that need to be adjusted. They can be selected by trial and error method. From the authors' experience, the coefficients (c_1, c_2, c_3) can be first adjusted to keep these terms ($\boldsymbol{w}_{\mathrm{t}x}^{\mathrm{T}}\boldsymbol{i}_{\mathrm{z}x}(k+1)$, $w_{\mathrm{com}}p_{\mathrm{com}}$, $\boldsymbol{w}_{\mathrm{d}x}^{\mathrm{T}}\boldsymbol{p}_{\mathrm{d}x}$) at the same order of magnitude. The tuning of w_2 is also important in this method. Its value will affect the rate of change in the circulating current. When the MMC operates at low frequency, a smaller value of w_2 can be selected appropriately to make the circulating current change more rapidly to counteract the energy difference between the upper and lower arms. When the MMC operates at high frequency, w_2 can be increased appropriately as the differential energy of the upper and lower arms will not be large under this condition. In this way, the selection process of these coefficients can be completed quickly.

At last, by applying this novel cost function to the MPC method, the system will achieve satisfactory performance in terms of both output currents and voltage balancing at the whole frequency range. In addition, the switching process for different control methods from low frequency to high frequency is not required. The effectiveness of the proposed method has been verified by the experimental results.

4.3 Using an exhaustive active-set method to realize the modulated MPC algorithm

Although the MMC can achieve satisfactory results over a wide frequency range by using the MPC scheme with the novel cost function, the heavy computational burden brought by the FCS-MPC method makes the proposed method difficult to be implemented in practice. The three-phase model of the MMC has been used in the proposed MPC method and thus there are $(N+1)^6$ insertion index combinations to be evaluated. In addition, as the new cost function is different from the conventional square-error one, most of the FCS-MPC methods with computational burden reduction techniques cannot be applied. The most promising approach is to implement the FCS-MPC method in two stages. The ac-side output voltage level and/or

dc-link output voltage level can be determined in the first stage. The internal control of the MMC can be realized by evaluating the rest insertion index combinations that satisfy the output level determined in the first stage. This method can effectively reduce the number of insertion index combinations to be evaluated by the FCS-MPC scheme, especially when the output voltage level can be easily or directly determined in the first stage. Although FCS-MPC with such a technique can reduce the computational burden to some extent, it is still computationally intensive when the number of SMs is large.

In order to reduce the computational load brought by FCS-MPC and improve the steady-state performance of the control variables, a modulated MPC algorithm has been proposed in this section. Firstly, the control problem of the MPC scheme with a new cost function has been formulated as a QP problem. As the control problem is ill-conditioned, traditional active-set methods or gradient-based methods cannot guarantee that the optimal solution can be found every time due to the degeneracy. Therefore, an exhaustive active-set method has been proposed to solve this kind of problem. The proposed method guarantees that the optimal solution will definitely be found. Moreover, the worst-case calculation step of this method is determined and thus the maximum computation time of this method can be determined. Besides, a large part of the calculations in the algorithm can be done offline in advance. In addition, each step for solving the problem is independent, so this method is a parallel algorithm. Overall, the proposed modulated MPC scheme can be completed within a certain time, which is independent of the number of SMs per arm in the MMC. Therefore, this method is not only suitable for MV motor control, but also for the application of an HVDC system, in which the number of SMs is large.

4.3.1 Problem reformulation

In order to facilitate the optimal solution, the control problem will be formulated as a QP problem.

According to (2.20), the discrete-time mathematical model of ac-side output currents in the matrix form of the control variable $\boldsymbol{x} = [v_{\mathrm{u}a}(k)\ v_{\mathrm{l}a}(k)\ v_{\mathrm{u}b}(k)\ v_{\mathrm{l}b}(k)\ v_{\mathrm{u}c}(k)\ v_{\mathrm{l}c}(k)]^{\mathrm{T}}$ is

$$\boldsymbol{i}_{\mathrm{s}} = \boldsymbol{A}_{\mathrm{s}}\boldsymbol{x} + \boldsymbol{b}_{\mathrm{s}}. \tag{4.2}$$

where

$$\boldsymbol{i}_{\mathrm{s}} = \begin{bmatrix} i_{\mathrm{sa}}(k+1) \\ i_{\mathrm{sb}}(k+1) \\ i_{\mathrm{sc}}(k+1) \end{bmatrix}, \boldsymbol{b}_{\mathrm{s}} = \begin{bmatrix} \alpha_1 i_{\mathrm{sa}}(k) - i^*_{\mathrm{sa}} \\ \alpha_1 i_{\mathrm{sb}}(k) - i^*_{\mathrm{sb}} \\ \alpha_1 i_{\mathrm{sc}}(k) - i^*_{\mathrm{sc}} \end{bmatrix}, \text{and } \boldsymbol{A}_{\mathrm{s}} = \frac{T_{\mathrm{s}}}{3L_d} \begin{bmatrix} -2 & 2 & 1 & -1 & 1 & -1 \\ 1 & -1 & -2 & 2 & 1 & -1 \\ 1 & -1 & 1 & -1 & -2 & 2 \end{bmatrix}.$$

Similarly, the discrete-time mathematical model of circulating currents can be written as

$$\boldsymbol{i}_{\mathrm{z}} = \boldsymbol{A}_{\mathrm{z}}\boldsymbol{x} + \boldsymbol{b}_{\mathrm{z}}. \tag{4.3}$$

where

$$\boldsymbol{i}_{\mathrm{z}} = \begin{bmatrix} i_{\mathrm{za}}(k+1) \\ i_{\mathrm{zb}}(k+1) \\ i_{\mathrm{zc}}(k+1) \end{bmatrix}, \boldsymbol{b}_{\mathrm{z}} = \begin{bmatrix} i_{\mathrm{za}}(k) \\ i_{\mathrm{sb}}(k) \\ i_{\mathrm{sc}}(k) \end{bmatrix}, \text{and } \boldsymbol{A}_{\mathrm{z}} = \frac{T_{\mathrm{s}}}{6L} \begin{bmatrix} -2 & -2 & 1 & 1 & 1 & 1 \\ 1 & 1 & -2 & -2 & 1 & 1 \\ 1 & 1 & 1 & 1 & -2 & -2 \end{bmatrix}.$$

The discrete-time mathematical model of dc-link current can be rewritten as

$$i_{\mathrm{dc}} = \boldsymbol{A}_{\mathrm{dc}}\boldsymbol{x} + b_{\mathrm{dc}}. \tag{4.4}$$

where $\boldsymbol{A}_{\mathrm{dc}} = \frac{-T_{\mathrm{s}}}{2L}\begin{bmatrix}1 & 1 & 1 & 1 & 1 & 1\end{bmatrix}$ and $b_{\mathrm{dc}} = i_{\mathrm{dc}}(k) + \frac{3T_{\mathrm{s}}}{2L}V_{\mathrm{dc}} - i^{*}_{\mathrm{dc}}$. The common-mode voltage can be expressed as

$$v_{\mathrm{NO}} = \boldsymbol{A}_{\mathrm{NO}}\boldsymbol{x}. \tag{4.5}$$

where $\boldsymbol{A}_{\mathrm{NO}} = \frac{1}{6}\begin{bmatrix}-1 & 1 & -1 & 1 & -1 & 1\end{bmatrix}$.

Recall the differential power (P_x^{Δ}) expression (2.26) from the previous Section 2.3.2.2 and redefine $p_{\mathrm{d}x}$ for the modulated MPC scheme as

$$p_{\mathrm{d}x} = V_{\mathrm{dc}}i_{\mathrm{s}x}(k)/2 - (v_{x\mathrm{N}} + 2v_{\mathrm{NO}}(k))(i_{\mathrm{z}x}(k+1) + i_{\mathrm{dc}}(k+1)/3), \tag{4.6}$$

where $v_{x\mathrm{N}}$ can be seen as twice the output phase voltage. In this method, it will use the value of a previous moment, that is $v_{x\mathrm{N}} = v_{\mathrm{l}x}(k-1) - v_{\mathrm{u}x}(k-1) - 2v_{\mathrm{NO}}(k-1)$. According to (4.6), the differential power ($p_{\mathrm{d}a}$, $p_{\mathrm{d}b}$ and $p_{\mathrm{d}c}$) in the matrix form can be written as

$$\begin{aligned} p_{\mathrm{d}a} &= \boldsymbol{x}^{\mathrm{T}}\boldsymbol{Q}_{\mathrm{d}a}\boldsymbol{x} + \boldsymbol{d}_{\mathrm{d}a}^{\mathrm{T}}\boldsymbol{x} + \mathrm{C}_{\mathrm{d}a}, \\ p_{\mathrm{d}b} &= \boldsymbol{x}^{\mathrm{T}}\boldsymbol{Q}_{\mathrm{d}b}\boldsymbol{x} + \boldsymbol{d}_{\mathrm{d}b}^{\mathrm{T}}\boldsymbol{x} + \mathrm{C}_{\mathrm{d}b}, \\ p_{\mathrm{d}c} &= \boldsymbol{x}^{\mathrm{T}}\boldsymbol{Q}_{\mathrm{d}c}\boldsymbol{x} + \boldsymbol{d}_{\mathrm{d}c}^{\mathrm{T}}\boldsymbol{x} + \mathrm{C}_{\mathrm{d}c}, \end{aligned} \tag{4.7}$$

where

$$\boldsymbol{Q}_{\mathrm{d}a} = \frac{T_{\mathrm{s}}}{L}\begin{bmatrix}\boldsymbol{A}_{\mathrm{NO}} \\ \boldsymbol{A}_{\mathrm{NO}} \\ \boldsymbol{O}_{4\times 6}\end{bmatrix}, \quad \boldsymbol{d}_{\mathrm{d}a} = (i_{\mathrm{z}a}(k) + \frac{i_{\mathrm{dc}}(k)}{3} + \frac{T_{\mathrm{s}}}{2L}V_{\mathrm{dc}})\boldsymbol{A}_{\mathrm{NO}} + \frac{T_{\mathrm{s}}}{2L}v_{a\mathrm{N}}\begin{bmatrix}1 \\ 1 \\ \boldsymbol{O}_{4\times 1}\end{bmatrix},$$

$$\boldsymbol{Q}_{\mathrm{d}b} = \frac{T_{\mathrm{s}}}{L}\begin{bmatrix}\boldsymbol{O}_{2\times 6} \\ \boldsymbol{A}_{\mathrm{NO}} \\ \boldsymbol{A}_{\mathrm{NO}} \\ \boldsymbol{O}_{2\times 6}\end{bmatrix}, \quad \boldsymbol{d}_{\mathrm{d}b} = (i_{\mathrm{z}b}(k) + \frac{i_{\mathrm{dc}}(k)}{3} + \frac{T_{\mathrm{s}}}{2L}V_{\mathrm{dc}})\boldsymbol{A}_{\mathrm{NO}} + \frac{T_{\mathrm{s}}}{2L}v_{b\mathrm{N}}\begin{bmatrix}\boldsymbol{O}_{2\times 1} \\ 1 \\ 1 \\ \boldsymbol{O}_{2\times 1}\end{bmatrix},$$

$$\boldsymbol{Q}_{\mathrm{d}c} = \frac{T_{\mathrm{s}}}{L}\begin{bmatrix}\boldsymbol{O}_{4\times 6} \\ \boldsymbol{A}_{\mathrm{NO}} \\ \boldsymbol{A}_{\mathrm{NO}}\end{bmatrix}, \quad \boldsymbol{d}_{\mathrm{d}c} = (i_{\mathrm{z}c}(k) + \frac{i_{\mathrm{dc}}(k)}{3} + \frac{T_{\mathrm{s}}}{2L}V_{\mathrm{dc}})\boldsymbol{A}_{\mathrm{NO}} + \frac{T_{\mathrm{s}}}{2L}v_{c\mathrm{N}}\begin{bmatrix}\boldsymbol{O}_{4\times 1} \\ 1 \\ 1\end{bmatrix},$$

and $\mathrm{C}_{\mathrm{d}x} = \frac{V_{\mathrm{dc}}i_{\mathrm{s}x}(k)}{2} - v_{x\mathrm{N}}(i_{\mathrm{z}x}(k) + \frac{i_{\mathrm{dc}}(k)}{3})$, $x = a, b, c$. According to (2.28), the common differential power for the three phase p_{com} can be rewritten as

$$p_{\mathrm{com}} = -2i_{\mathrm{dc}}(k)v_{\mathrm{NO}} + \sum_{x=a,b,c}(v_{\mathrm{u}x}(k) - v_{\mathrm{l}x}(k))i_{\mathrm{z}x}(k) = \boldsymbol{d}_{\mathrm{com}}^{\mathrm{T}}\boldsymbol{x}, \tag{4.8}$$

where $\boldsymbol{d}_{\mathrm{com}}$ can be expressed as

$$\boldsymbol{d}_{\mathrm{com}} = \begin{bmatrix} i_{\mathrm{z}a}(k) + i_{\mathrm{dc}}(k)/3 \\ -i_{\mathrm{z}a}(k) - i_{\mathrm{dc}}(k)/3 \\ i_{\mathrm{z}b}(k) + i_{\mathrm{dc}}(k)/3 \\ -i_{\mathrm{z}b}(k) - i_{\mathrm{dc}}(k)/3 \\ i_{\mathrm{z}c}(k) + i_{\mathrm{dc}}(k)/3 \\ -i_{\mathrm{z}c}(k) - i_{\mathrm{dc}}(k)/3 \end{bmatrix}. \tag{4.9}$$

The cost function for the modulated MPC scheme is defined as

$$\begin{aligned} J =& w_1 \left\| \boldsymbol{i}_{\mathrm{s}}^{*} - \boldsymbol{i}_{\mathrm{s}}(k+1) \right\|_2^2 + w_2 \left\| \boldsymbol{i}_{\mathrm{z}}(k+1) \right\|_2^2 + w_3 \left\| i_{\mathrm{dc}}^{*} - i_{\mathrm{dc}}(k+1) \right\|_2^2 \\ &+ \boldsymbol{w}_{\mathrm{t}}^{\mathrm{T}} \boldsymbol{i}_{\mathrm{z}}(k+1) + w_{\mathrm{com}} p_{\mathrm{com}} + \boldsymbol{w}_{\mathrm{d}}^{\mathrm{T}} \boldsymbol{p}_{\mathrm{d}} + w_4 \left\| \boldsymbol{i}_{\mathrm{z}}(k+1) - \boldsymbol{i}_{\mathrm{z}}(k) \right\|_2^2 + w_5 v_{\mathrm{NO}}^2. \end{aligned} \tag{4.10}$$

Different from (4.1), two terms have been added in this new cost function (4.10). The term $\left\| \boldsymbol{i}_{\mathrm{z}}(k+1) - \boldsymbol{i}_{\mathrm{z}}(k) \right\|_2^2$ can be used to limit the change rate of the circulating currents and the last term v_{NO}^2 is to limit the magnitude of common-mode voltage.

Now the modulated MPC method with the new cost function (4.10) can be formulated as a QP problem as

$$\begin{aligned} \min_{\boldsymbol{x}} \ & J(\boldsymbol{x}) = \frac{1}{2} \boldsymbol{x}^{\mathrm{T}} \boldsymbol{Q} \boldsymbol{x} + \boldsymbol{d}^{\mathrm{T}} \boldsymbol{x} \\ \text{subject to} \quad & \boldsymbol{l} \preceq \boldsymbol{x} \preceq \boldsymbol{u} \end{aligned} \tag{4.11}$$

$\boldsymbol{l}$ and $\boldsymbol{u}$ represent the lower bound and upper bound of the control variable $\boldsymbol{x}$ and they can be written as

$$\begin{aligned} \boldsymbol{l} &= \begin{bmatrix} 0 & 0 & 0 & 0 & 0 & 0 \end{bmatrix}^{\mathrm{T}}, \\ \boldsymbol{u} &= \begin{bmatrix} \sum_{i=1}^{N} v_{\mathrm{c,u}a}^{i} & \sum_{i=1}^{N} v_{\mathrm{c,l}a}^{i} & \sum_{i=1}^{N} v_{\mathrm{c,u}b}^{i} & \sum_{i=1}^{N} v_{\mathrm{c,l}b}^{i} & \sum_{i=1}^{N} v_{\mathrm{c,u}c}^{i} & \sum_{i=1}^{N} v_{\mathrm{c,l}c}^{i} \end{bmatrix}^{\mathrm{T}}. \end{aligned} \tag{4.12}$$

According to (4.2) - (4.8), the matrix $\boldsymbol{Q}$ can be expressed as

$$\boldsymbol{Q} = \boldsymbol{Q}_{\mathrm{c}} + \boldsymbol{a}\boldsymbol{b}^{\mathrm{T}}, \tag{4.13}$$

where

$$\boldsymbol{Q}_{\mathrm{c}} = w_1 \boldsymbol{A}_{\mathrm{s}}^{\mathrm{T}} \boldsymbol{A}_{\mathrm{s}} + w_2 \boldsymbol{A}_{\mathrm{z}}^{\mathrm{T}} \boldsymbol{A}_{\mathrm{z}} + w_3 \boldsymbol{A}_{\mathrm{dc}}^{\mathrm{T}} \boldsymbol{A}_{\mathrm{dc}} + w_4 \boldsymbol{A}_{\mathrm{z}}^{\mathrm{T}} \boldsymbol{A}_{\mathrm{z}} + w_5 \boldsymbol{A}_{\mathrm{NO}}^{\mathrm{T}} \boldsymbol{A}_{\mathrm{NO}}, \tag{4.14}$$

$$\boldsymbol{a} = \begin{bmatrix} w_{\mathrm{d}a} & w_{\mathrm{d}a} & w_{\mathrm{d}b} & w_{\mathrm{d}b} & w_{\mathrm{d}c} & w_{\mathrm{d}c} \end{bmatrix}, \tag{4.15}$$

$$\boldsymbol{b} = \frac{T_{\mathrm{s}}}{L} \boldsymbol{A}_{\mathrm{NO}}. \tag{4.16}$$

It should be noted that when the parameters of the MMC system are known and the weighting factors are selected in advance, $\boldsymbol{Q}_{\mathrm{c}}$ is a constant matrix. Thus, its inverse matrix can be calculated offline. According to the Sherman–Morrison formula, the inverse matrix of $\boldsymbol{Q}$ can be easily obtained as

$$\boldsymbol{Q}^{-1} = \left(\boldsymbol{Q}_{\mathrm{c}} + \boldsymbol{a}\boldsymbol{b}^{\mathrm{T}} \right)^{-1} = \boldsymbol{Q}_{\mathrm{c}}^{-1} - \frac{\boldsymbol{Q}_{\mathrm{c}}^{-1} \boldsymbol{a} \boldsymbol{b}^{\mathrm{T}} \boldsymbol{Q}_{\mathrm{c}}^{-1}}{1 + \boldsymbol{b}^{\mathrm{T}} \boldsymbol{Q}_{\mathrm{c}}^{-1} \boldsymbol{a}}. \tag{4.17}$$

In this way, the computational burden of the inverse of matrix $\boldsymbol{Q}$ on line can be reduced greatly.

The vector $\boldsymbol{d}$ in (4.11) can be written as

$$\begin{aligned} \boldsymbol{d} = w_1 \boldsymbol{A}_{\mathrm{s}}^{\mathrm{T}} \boldsymbol{b}_{\mathrm{s}} + w_2 \boldsymbol{A}_{\mathrm{z}}^{\mathrm{T}} \boldsymbol{b}_{\mathrm{z}} + & w_3 \boldsymbol{A}_{\mathrm{dc}}^{\mathrm{T}} b_{\mathrm{dc}} + \frac{w_{\mathrm{d}a}}{2} \boldsymbol{d}_{\mathrm{d}a} + \frac{w_{\mathrm{d}b}}{2} \boldsymbol{d}_{\mathrm{d}b} + \frac{w_{\mathrm{d}c}}{2} \boldsymbol{d}_{\mathrm{d}c} \\ & + \frac{w_{\mathrm{com}}}{2} \boldsymbol{d}_{\mathrm{com}} + w_{\mathrm{t}a} \boldsymbol{A}_{\mathrm{z1}} + w_{\mathrm{t}b} \boldsymbol{A}_{\mathrm{z2}} + w_{\mathrm{t}c} \boldsymbol{A}_{\mathrm{z3}}, \end{aligned} \tag{4.18}$$

where $\boldsymbol{A}_{\mathrm{z1}}$, $\boldsymbol{A}_{\mathrm{z2}}$ and $\boldsymbol{A}_{\mathrm{z3}}$ represent the first, second and third rows of the matrix $\boldsymbol{A}_{\mathrm{z}}$, respectively.

4.3.2 Using an exhaustive active-set method to obtain the optimal solution

The basic idea of this exhaustive active-set method is to evaluate all possible active sets until the KKT condition is satisfied. In this way, the optimal solution can be obtained.

Considering (4.11), the associated Lagrangian function can be constructed as

$$\mathcal{L}(\boldsymbol{x}, \boldsymbol{s}, \boldsymbol{t}) = \frac{1}{2}\boldsymbol{x}^{\mathrm{T}}\boldsymbol{Q}\boldsymbol{x} + \boldsymbol{d}^{\mathrm{T}}\boldsymbol{x} + \boldsymbol{s}^{\mathrm{T}}(\boldsymbol{x} - \boldsymbol{u}) + \boldsymbol{t}^{\mathrm{T}}(\boldsymbol{l} - \boldsymbol{x}), \tag{4.19}$$

where $\boldsymbol{s}$ and $\boldsymbol{t}$ are Lagrange multipliers. The KKT condition is given by

$$\boldsymbol{Q}\boldsymbol{x} + \boldsymbol{d} + \boldsymbol{s} - \boldsymbol{t} = \boldsymbol{0}, \tag{4.20a}$$
$$s_i(x_i - u_i) = 0, \forall i \in \mathcal{C} \tag{4.20b}$$
$$t_i(l_i - x_i) = 0, \forall i \in \mathcal{C} \tag{4.20c}$$
$$\boldsymbol{l} \preceq \boldsymbol{x} \preceq \boldsymbol{u}, \boldsymbol{s} \succeq \boldsymbol{0}, \boldsymbol{t} \succeq \boldsymbol{0}, \tag{4.20d}$$

where $\mathcal{C} = \{1, 2, ..., n\}$ and the subscript i represents the i_{th} element of the vector. As we can easily design the cost function such that the matrix $\boldsymbol{Q}$ is positive definite. Therefore, the QP problem (4.11) can achieve the minimum when $(\boldsymbol{x}, \boldsymbol{s}, \boldsymbol{t})$ satisfies the KKT conditions in (3.23). Because of the small scale of our problem, the dimension of the problem is 6, we can evaluate all the possible active sets to obtain the optimal solution. In order to describe the method briefly, some working sets ($\mathcal{A}_l$, $\mathcal{A}_u$, and $\mathcal{I}$) are declared in advance. $\mathcal{A}_l$ is the lower bound subset of $\mathcal{C}$. It indicates that for each $i \in \mathcal{A}_l$, x_i will touch the lower bound, which is $x_i = l_i$. Similarly, upper bound subset $\mathcal{A}_u$ includes the indices i, which indicates $x_i = u_i$ for each $i \in \mathcal{A}_u$. Set $\mathcal{I}$ can be obtained by $\mathcal{C} \setminus (\mathcal{A}_l \cup \mathcal{A}_u)$. It assumes that for each $i \in \mathcal{I}$, x_i neither exceeds the lower nor the upper bound. Based on $\mathcal{A}_u$, $\mathcal{A}_l$ and $\mathcal{I}$, the bound constrained problem in (4.11) will be converted into the equality-constrained QP (EQP) problem. Again, since it is a bound constrained problem, we can easily obtain the following equation according to the current working sets ($\mathcal{A}_u$, $\mathcal{A}_l$ and $\mathcal{I}$) as

$$\begin{aligned} \boldsymbol{x}_{\mathcal{A}_l} &= \boldsymbol{l}_{\mathcal{A}_l},\ \boldsymbol{s}_{\mathcal{A}_l} = \boldsymbol{0}, \\ \boldsymbol{x}_{\mathcal{A}_u} &= \boldsymbol{u}_{\mathcal{A}_u},\ \boldsymbol{t}_{\mathcal{A}_u} = \boldsymbol{0}, \\ \boldsymbol{s}_{\mathcal{I}} &= \boldsymbol{0},\ \boldsymbol{t}_{\mathcal{I}} = \boldsymbol{0}. \end{aligned} \tag{4.21}$$

Now only $\boldsymbol{x}_{\mathcal{I}}$, $\boldsymbol{s}_{\mathcal{A}_u}$ and $\boldsymbol{t}_{\mathcal{A}_l}$ need to be solved. According to (4.20a), these variables can be obtained by solving the following equation as

$$\begin{bmatrix} \boldsymbol{Q}_{\mathcal{A}_u\mathcal{A}_u} & \boldsymbol{Q}_{\mathcal{A}_u\mathcal{A}_l} & \boldsymbol{Q}_{\mathcal{A}_u\mathcal{I}} \\ \boldsymbol{Q}_{\mathcal{A}_l\mathcal{A}_u} & \boldsymbol{Q}_{\mathcal{A}_l\mathcal{A}_l} & \boldsymbol{Q}_{\mathcal{A}_l\mathcal{I}} \\ \boldsymbol{Q}_{\mathcal{I}_I\mathcal{A}_u} & \boldsymbol{Q}_{\mathcal{I}_I\mathcal{A}_l} & \boldsymbol{Q}_{\mathcal{I}\mathcal{I}} \end{bmatrix} \begin{bmatrix} \boldsymbol{x}_{\mathcal{A}_u} \\ \boldsymbol{x}_{\mathcal{A}_l} \\ \boldsymbol{x}_{\mathcal{I}} \end{bmatrix} + \begin{bmatrix} \boldsymbol{d}_{\mathcal{A}_u} \\ \boldsymbol{d}_{\mathcal{A}_l} \\ \boldsymbol{d}_{\mathcal{I}} \end{bmatrix} + \begin{bmatrix} \boldsymbol{s}_{\mathcal{A}_u} \\ \boldsymbol{s}_{\mathcal{A}_l} \\ \boldsymbol{s}_{\mathcal{I}} \end{bmatrix} - \begin{bmatrix} \boldsymbol{t}_{\mathcal{A}_u} \\ \boldsymbol{t}_{\mathcal{A}_l} \\ \boldsymbol{t}_{\mathcal{I}} \end{bmatrix} = \boldsymbol{0}. \tag{4.22}$$

Based on (4.21), $\boldsymbol{x}_{\mathcal{I}}$ can be solved firstly by

$$\boldsymbol{Q}_{\mathcal{I}\mathcal{I}}\boldsymbol{x}_{\mathcal{I}} = -\boldsymbol{d}_{\mathcal{I}} - \boldsymbol{Q}_{\mathcal{I}\mathcal{A}_u}\boldsymbol{x}_{\mathcal{A}_u} - \boldsymbol{Q}_{\mathcal{I}\mathcal{A}_l}\boldsymbol{x}_{\mathcal{A}_l}. \tag{4.23}$$

Note that the inverse matrix of $\boldsymbol{Q}_{\mathcal{I}\mathcal{I}}$ can be easily obtained according to (4.17). After $\boldsymbol{x}_{\mathcal{I}}$ is solved, the $\boldsymbol{s}_{\mathcal{A}_u}$ and $\boldsymbol{t}_{\mathcal{A}_l}$ can be obtained as

$$\begin{aligned} \boldsymbol{s}_{\mathcal{A}_u} &= -\boldsymbol{Q}_{\mathcal{A}_u\mathcal{A}_u}\boldsymbol{x}_{\mathcal{A}_u} - \boldsymbol{Q}_{\mathcal{A}_u\mathcal{A}_l}\boldsymbol{x}_{\mathcal{A}_l} - \boldsymbol{Q}_{\mathcal{A}_u\mathcal{I}}\boldsymbol{x}_{\mathcal{I}} - \boldsymbol{d}_{\mathcal{A}_u}, \\ \boldsymbol{t}_{\mathcal{A}_l} &= \boldsymbol{Q}_{\mathcal{A}_l\mathcal{A}_u}\boldsymbol{x}_{\mathcal{A}_u} + \boldsymbol{Q}_{\mathcal{A}_l\mathcal{A}_l}\boldsymbol{x}_{\mathcal{A}_l} + \boldsymbol{Q}_{\mathcal{A}_l\mathcal{I}}\boldsymbol{x}_{\mathcal{I}} + \boldsymbol{d}_{\mathcal{A}_l}. \end{aligned} \tag{4.24}$$

So far, all the variables have been solved based on the present working sets. As the proposed method needs to evaluate all possible active sets, the possible cases will be discussed below.

It is easy to conclude that there are only three possible cases for each element x_i in the vector $\boldsymbol{x}$: the lower bound is an active constraint ($x_i = l_i$), the upper bound is an active constraint ($x_i = u_i$) or neither the upper nor lower bound is the active constraint ($l_i < x_i < u_i$). The state of the working sets ($\mathcal{A}_u$, $\mathcal{A}_l$ and $\mathcal{I}$) corresponding to the above case can be expressed as $i \in \mathcal{A}_l$ or $i \in \mathcal{A}_u$ or $i \in \mathcal{I}$. Since the dimension of the problem is 6, there will be a total of 3^6 possible combinations of active sets. So by solving these 3^6 EQP equations in (4.23) and (4.24), we can always get the optimal solution.

To reduce the computational burden of the proposed method, the solution process for Equation (4.23) has been studied. It can be seen that although Equation (4.23) needs to be solved 3^6 times according to different conditions, there are only 2^6 cases of matrix $\boldsymbol{Q}_{\mathcal{I}\mathcal{I}}$ in (4.23) according to all possible cases of the set $\mathcal{I}$. Therefore, we can reduce a large computational burden by simply computing, storing and calling only 2^6 cases of the inverse matrix of $\boldsymbol{Q}_{\mathcal{I}\mathcal{I}}$ during 3^6 times of solving (4.23).

Once $\boldsymbol{x}_i$, $\boldsymbol{s}_{\mathcal{A}_u}$ and $\boldsymbol{t}_{\mathcal{A}_l}$ have been solved, the KKT condition (4.20d) should be checked. If (4.20d) is satisfied, the optimal solution is found. Otherwise, another iteration with a new working sets ($\mathcal{A}_u$, $\mathcal{A}_l$ and $\mathcal{I}$) will be executed until the solution ($\boldsymbol{x}_i$, $\boldsymbol{s}_{\mathcal{A}_u}$ and $\boldsymbol{t}_{\mathcal{A}_l}$) satisfies (4.20d). After enumerating all the possible combinations of active sets, the optimal solution $\boldsymbol{x}^*$, which presents the reference voltage for each arm, can be obtained.

Although the proposed method requires longer computation time compared to the traditional active-set methods/gradient-based methods, it guarantees that the optimal solution can definitely be found. It is worth noting that for the QP problem in (4.11), traditional active set methods or gradient-based methods cannot guarantee that the optimal solution can be found every time due to degeneracy. Thus, it is necessary to use this exhaustive active-set method to obtain the optimal solution for the proposed control scheme. Moreover, the worst calculation time (or iteration step) of the method is deterministic, which means that the calculation time for the control system is determinable and is no longer affected by the number of SMs per arm and the convergence speed of the optimization algorithm.

According to the indirect modulation method, the insertion/modulation index for each arm can be obtained as

$$\boldsymbol{n} = N\mathrm{diag}(\boldsymbol{u})^{-1}\boldsymbol{x}^*,\ \boldsymbol{m} = \mathrm{diag}(\boldsymbol{u})^{-1}\boldsymbol{x}^*, \tag{4.25}$$

where $\boldsymbol{n}$ represents the insertion index and $\boldsymbol{m}$ represents the modulation index. $\boldsymbol{u}$ is the upper bound of (4.11) and $\mathrm{diag}(\boldsymbol{u})$ is the abbreviated form of the diagonal matrix $\mathrm{diag}(u_1, ..., u_\mathrm{n})$. At last, the insertion/modulation index can be directly applied to the sorting and modulation stage to realize the control of the MMC system. The implementation of the modulation method and voltage sorting algorithm can be found in Section 3.2.2.3.

4.4 Experimental validations

Comparative experiments for both the FCS-MPC scheme and modulated MPC scheme will be carried out to verify that the proposed methods allow the MMC to operate over a wide frequency range. In addition, the experimental results of the MMC driving a permanent magnet

synchronous motor (PMSM) are provided to further demonstrate the effectiveness of the proposed FCS-MPC method. The sampling interval for the proposed FCS-MPC scheme is 100 µs. As the proposed modulated MPC scheme with the novel cost function requires an exhaustive active-set method, the calculation time of this method will be longer. Therefore, the control period of the modulated MPC scheme is set to 150 µs. In this section, the experimental results for both FCS-MPC and modulated MPC will be presented to verify the effectiveness of the proposed methods.

4.4.1 Comparative study of circulating current injection method and proposed method at low frequency

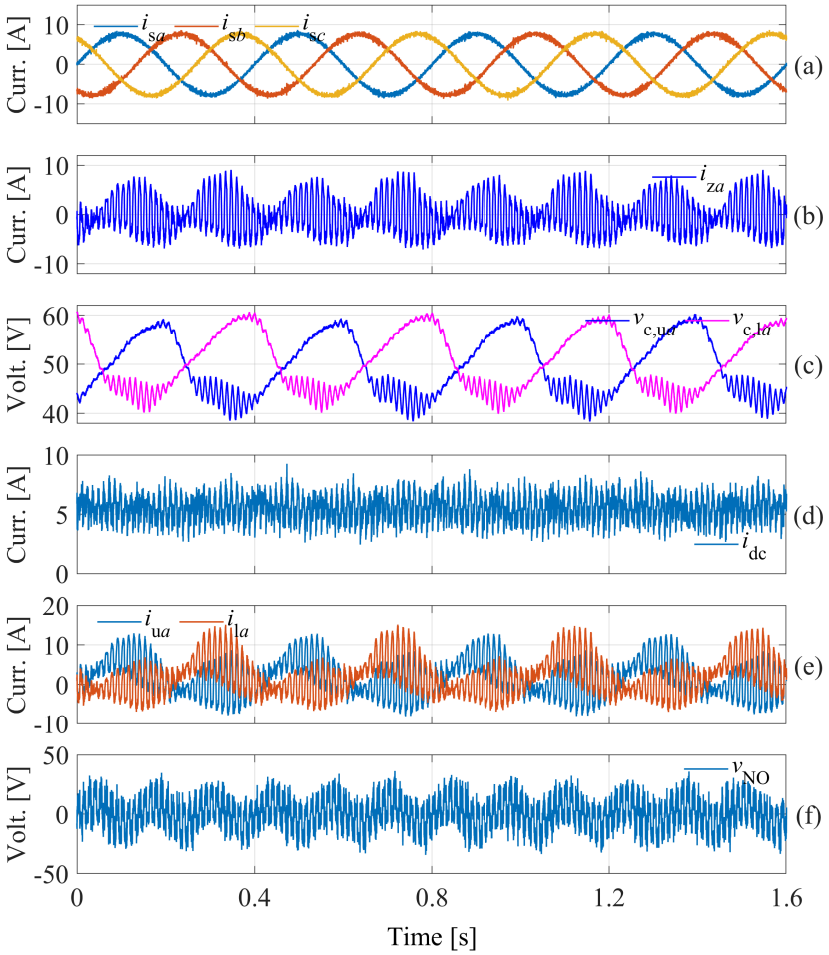

Figure 4.1: Steady-state performance of MMC with the circulating current injection method at 2.5 Hz.

In this section, a brief comparison has been made between the proposed method and the high-frequency injection method in the case of MMC operating at extremely low frequency with RL load. The steady-state performance of the MMC operating at 2.5 Hz controlled by the high-frequency circulating current injection method introduced in [56] has been given as

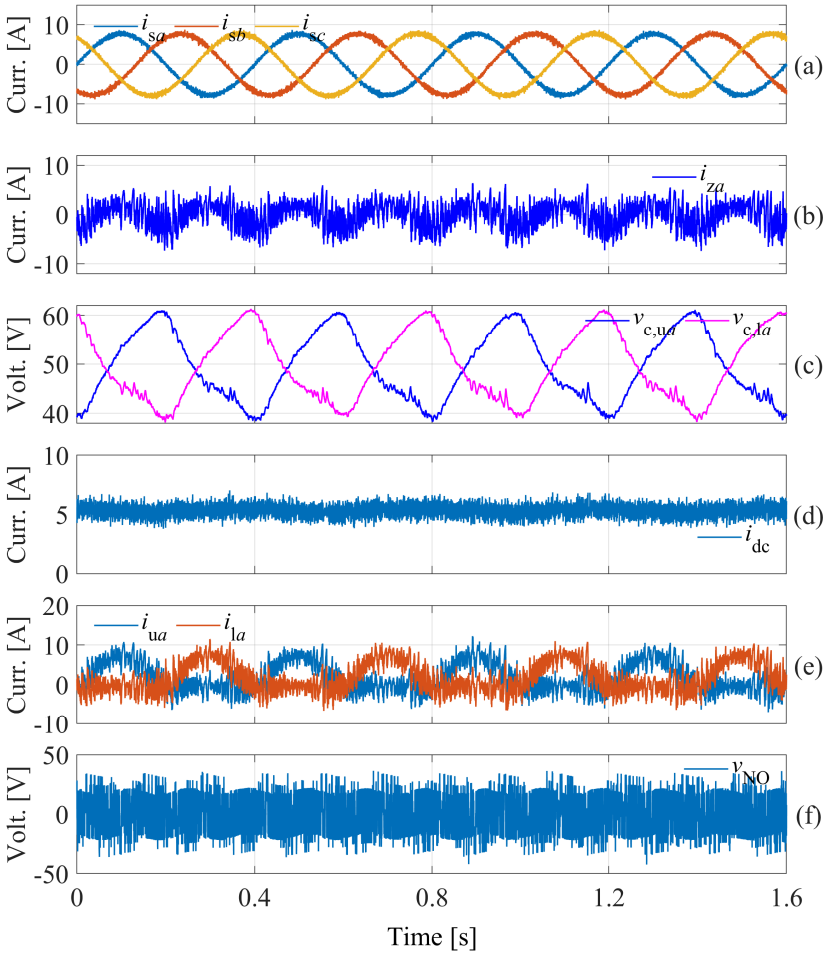

Figure 4.2: Steady-state performance of MMC with the proposed FCS-MPC method at 2.5 Hz.

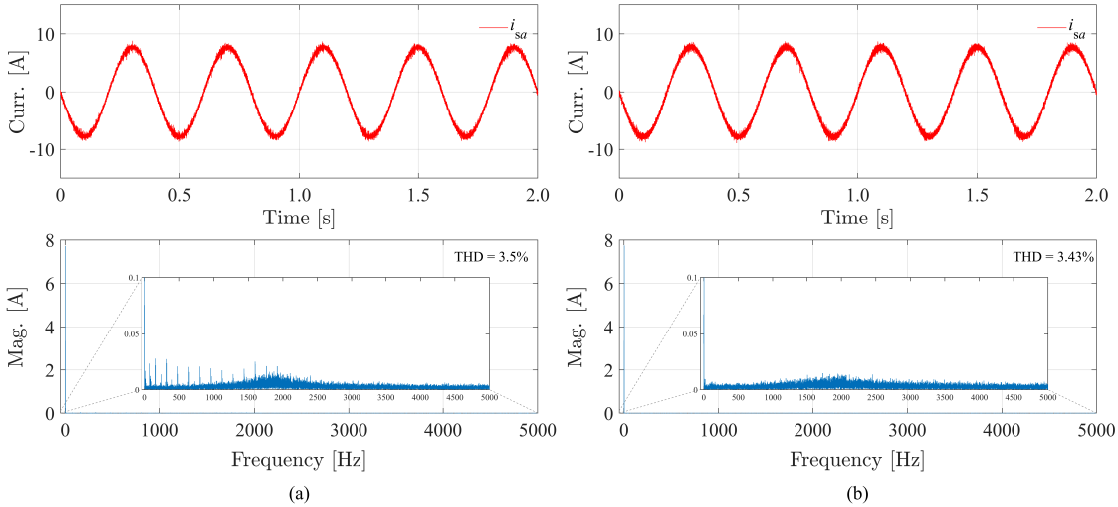

Figure 4.3: FFT analysis of the output current i_{sa} when the amplitude is 8 A. (a) Injection method. (b) Proposed method.

a comparison shown in Fig. 4.1. The amplitude of the output currents is set to $8\,\mathrm{A}$. From up to down the waveforms of output currents (i_{sa}, i_{sb} and i_{sc}), the circulating current in phase a (i_{za}), SM capacitor voltages of the upper and lower arms ($v_{c,ua}$ and $v_{c,la}$), the dc-link current (i_{dc}), upper and lower arm currents (i_{ua} and i_{la}) and the equivalent common-mode voltage in one control period (v_{NO}) are presented. As depicted in Fig. 4.1, the injection method can provide a satisfactory steady-state performance of the output currents, and the SM capacitor voltages between the upper and lower arms are well balanced. In addition, the ripples of SM capacitor voltages are well maintained. However, with the injection method, the magnitude of the circulating current and arm currents is large. As we know, the circulating current is obtained by dividing the compensated power by the common-mode voltage in the injection method. The common-mode voltage shown in Fig. 4.1(f) is small in this case, and thus the magnitude of the circulating current is large, which increases the current stress on the switching devices. Besides, many spikes can be observed on the dc-link current, which are caused by the injected circulating current and common-mode voltage.

It can be seen that the proposed FCS-MPC method can also provide a satisfactory steady-state performance of the output currents. Moreover, with the proposed method, smaller circulating current and arm currents can be achieved while the capacitor voltage ripple is comparable to that of the injection method. The ripple of the dc-link current shown in Fig. 4.2(d) is also small. It should be noted that the circulating current not only has high-frequency components but also has an obvious second harmonic component. This second harmonic component is involved in the power compensation along with the output voltage. From Fig. 4.2(f), we can find that the proposed method can fully utilize the common-mode voltage of the MMC system.

Fast Fourier transform (FFT) analysis and total harmonic distortion (THD) results can be used to evaluate the steady-state performance of the injection method and the proposed method which has been provided in Fig. 4.3. As shown in Fig. 4.3, these two methods have similar performance, where the THD result of the proposed method is 3.43%, while the THD result of the injection method is 3.5%. It is worth noting that the switching frequency of the proposed MPC method is only $2.9\,\mathrm{kHz}$, which is much lower than the switching frequency of the injection method. Thus, lower power losses can be achieved by the proposed method. Besides, the harmonic components of the injected frequency and its integer multiples can be observed in the spectrum shown in Fig. 4.3(a), which means that the output current will be affected by the injected common-mode voltage and circulating current in this case.

4.4.2 Comparative study of conventional MPC method and proposed MPC method with RL load

The parameters of the MMC system with RL load can be found in Section 2.5. In the following section, the conventional FCS-MPC method described in Section 2.4.2 and the proposed FCS-MPC method will be compared in the experiments.

The experimental results of the proposed FCS-MPC method under the step change in the amplitude (from $6\,\mathrm{A}$ to $10\,\mathrm{A}$) of the ac output currents at $50\,\mathrm{Hz}$ are shown in Fig. 4.4.

From Fig. 3.3, it can be seen that the dynamic response of ac-side currents, circulating currents and the dc-link current is fast. With the proposed method, the SM capacitor voltages of the upper and lower arms are well balanced. Different from the conventional FCS-MPC method shown in Fig. 2.19, the circulating current of the proposed method is smaller than that of the

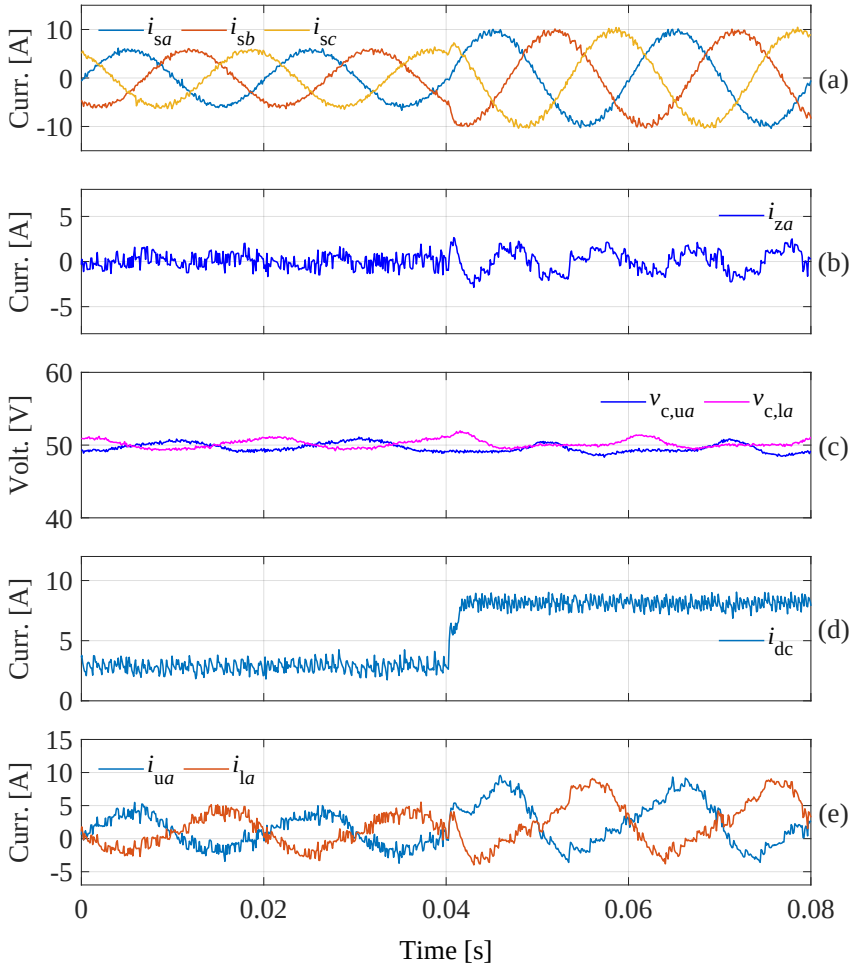

Figure 4.4: Step change in ac currents with the proposed FCS-MPC at 50 Hz.

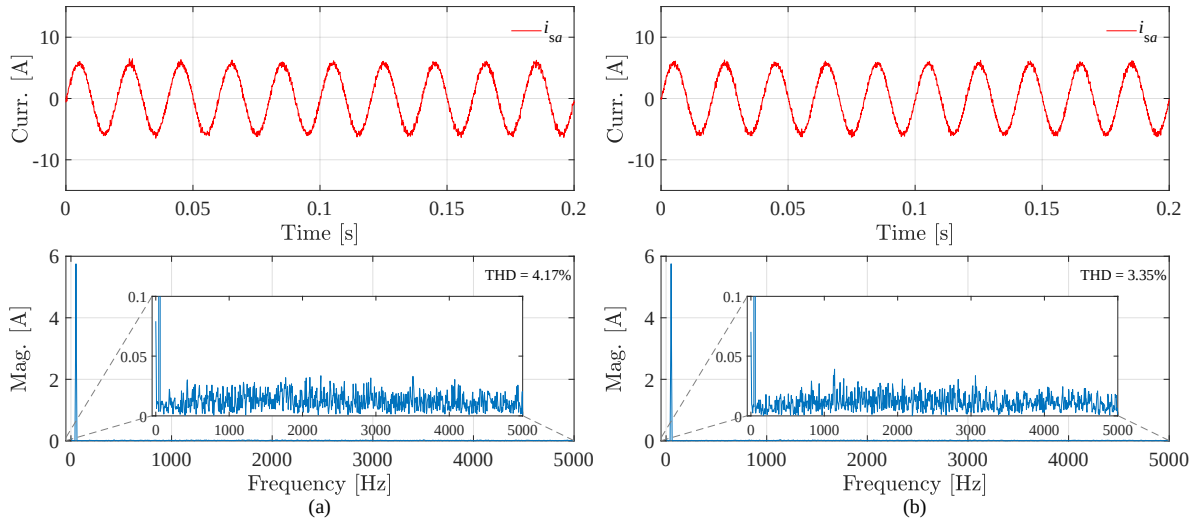

Figure 4.5: FFT analysis of the output current i_{sa} when the amplitude is 6 A at 50 Hz. (a) Conventional method. (b) Proposed method.

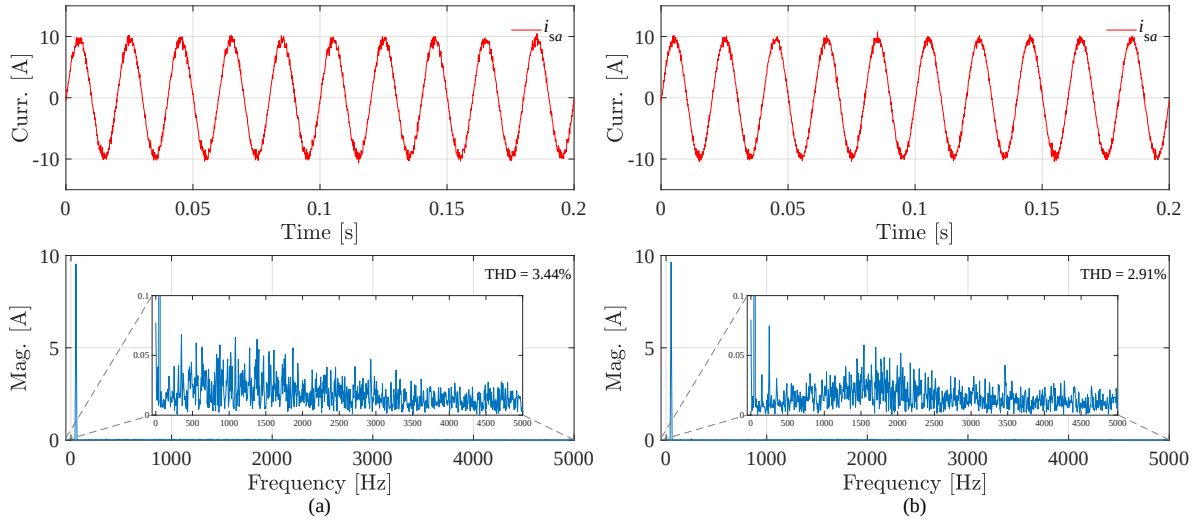

Figure 4.6: FFT analysis of the output current i_{sa} when the amplitude is 10 A at 50 Hz. (a) Conventional method. (b) Proposed method.

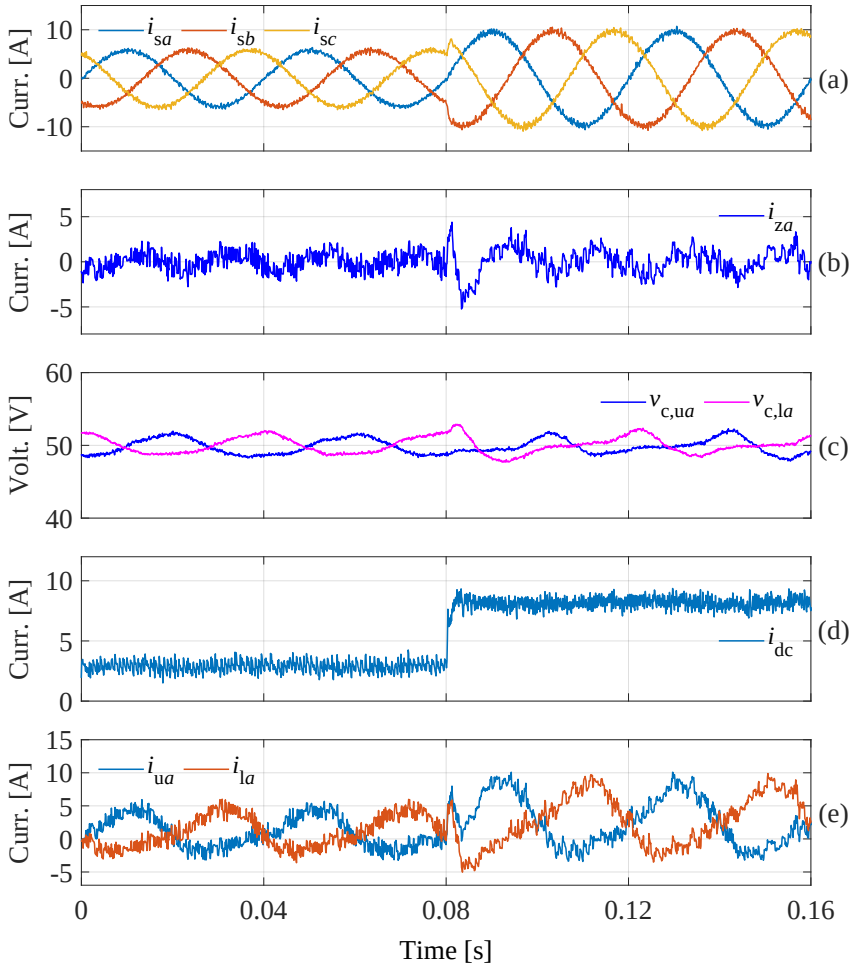

Figure 4.7: Step change in ac currents with the proposed FCS-MPC at 25 Hz.

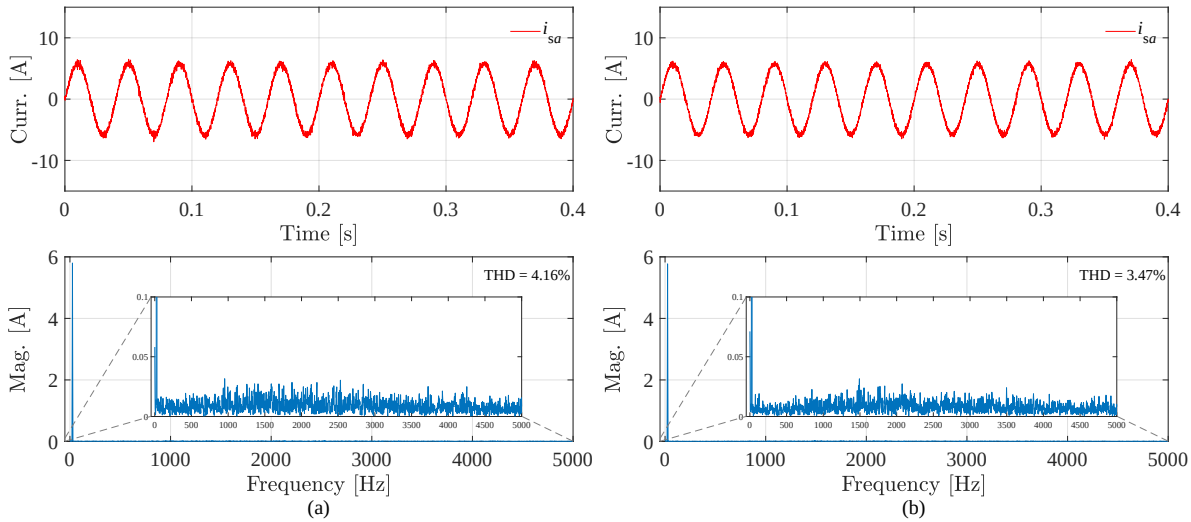

Figure 4.8: FFT analysis of the output current i_{sa} when the amplitude is 6 A at 25 Hz. (a) Conventional method. (b) Proposed method.

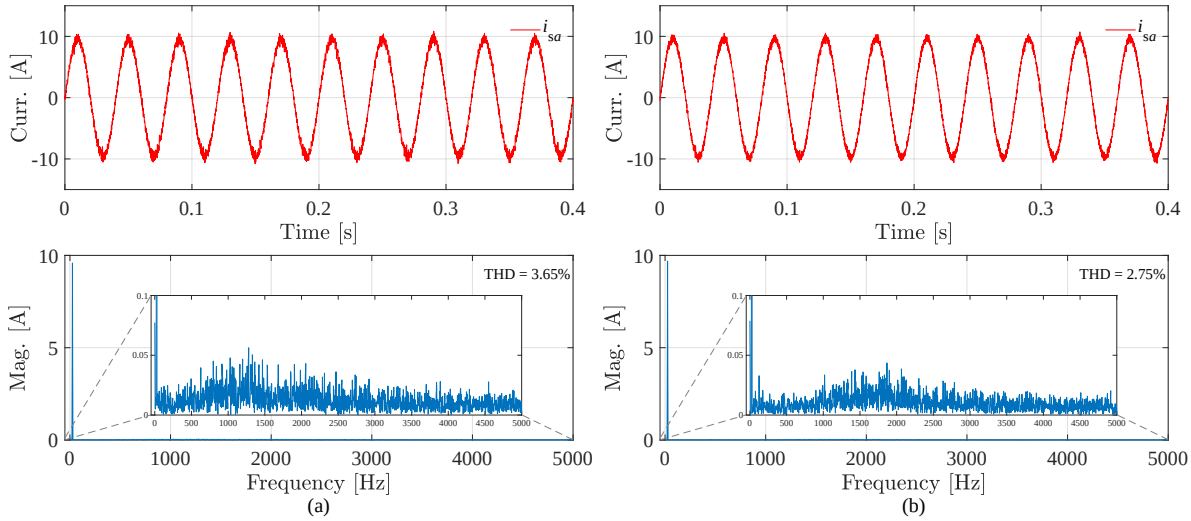

Figure 4.9: FFT analysis of the output current i_{sa} when the amplitude is 10 A at 25 Hz. (a) Conventional method. (b) Proposed method.

conventional method when the amplitude of ac currents is 6 A. Moreover, in this case, the circulating current of the proposed method does not show a significant second harmonic component compared to the conventional method. When the amplitude of ac currents increases to 10 A, the circulating currents for both methods present obvious second harmonic components, which can be used to regulate the energy between each phase. Note that the proposed method performs better in terms of ac currents at a steady state compared to the conventional method. The FFT analysis and THD results for both methods under different conditions are shown in Fig. 4.5 and Fig. 4.6, respectively.

As it is shown in Fig. 4.5, when the amplitude of ac currents is 6 A, the THD result of the

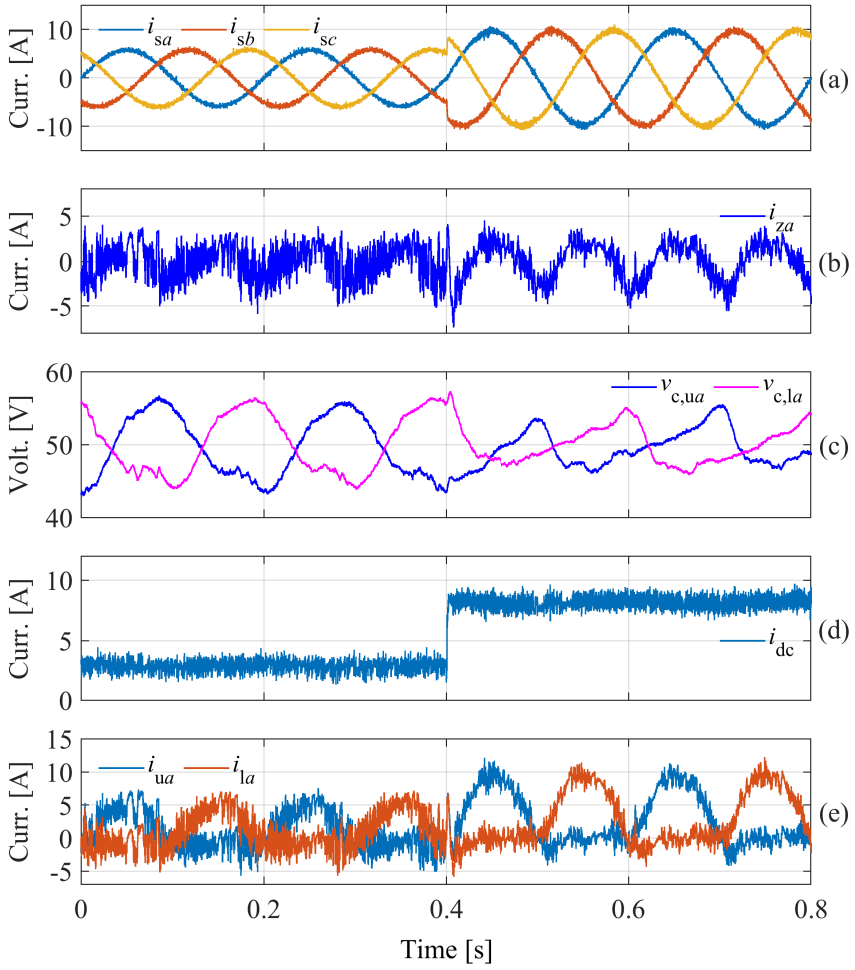

Figure 4.10: Step change in ac currents with the proposed FCS-MPC at 5 Hz.

proposed method is only 3.35%, which is an improvement of nearly 20% compared to the THD of 4.17% for the conventional method. When the amplitude of ac currents increases to 10 A, the THD result of the proposed method becomes 2.91%, while the THD of the conventional method is 3.44%. Therefore, we can conclude that the proposed method performs better in terms of output currents at a steady state compared to the conventional method.

The similar conclusion drawn from the experimental results at 50 Hz can also be extended to the case of MMC operating at 25 Hz, as shown in Fig. 4.7. Another point to emphasize is that the arm currents (i_{ua} and i_{la}) of the proposed method at 25 Hz and 50 Hz is approximately sinusoidal when the amplitude of ac currents is 6 A. It can be seen that the arm currents in this pattern are able to eliminate or suppress circulating currents. The reason why arm currents can present this pattern is that the ripple of SM capacitor voltage is small at medium and high frequencies (25 Hz and 50 Hz), so large circulating currents are not required to regulate the SM capacitor voltage.

The FFT analysis and THD results of MMC operating at 25 Hz are given in Fig. 4.8 and Fig. 4.9, respectively. It can be seen that better steady-state performance of ac currents can be achieved by using the proposed method.

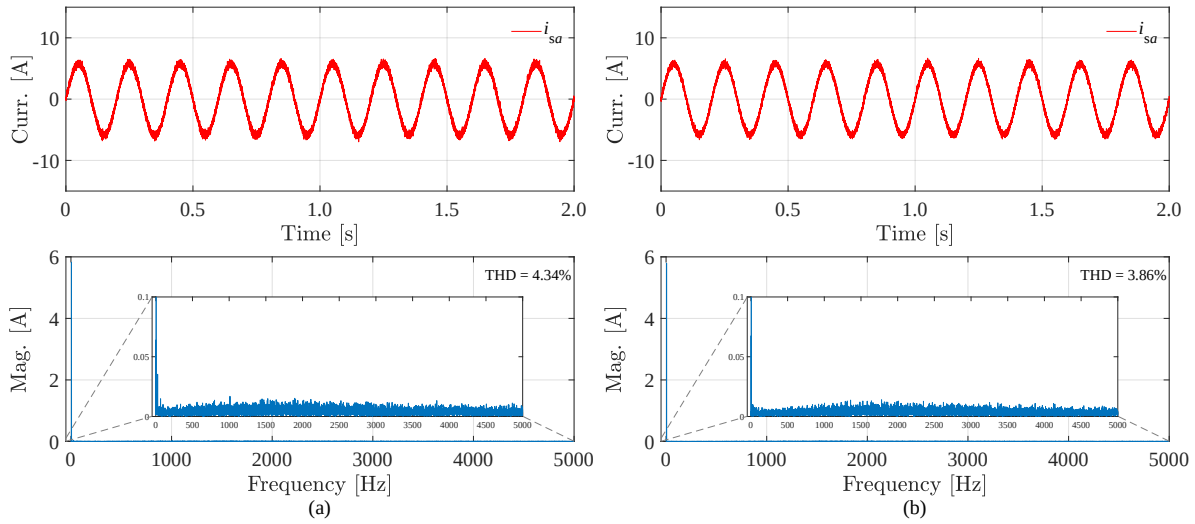

Figure 4.11: FFT analysis of the output current i_{sa} when the amplitude is $6\,\mathrm{A}$ at $5\,\mathrm{Hz}$. (a) Conventional method. (b) Proposed method.

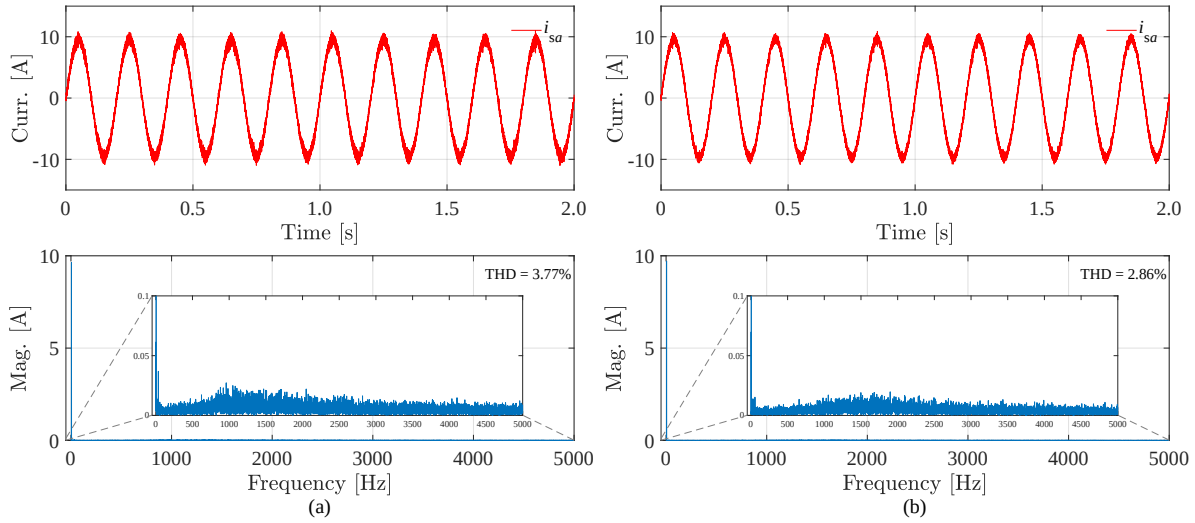

Figure 4.12: FFT analysis of the output current i_{sa} when the amplitude is $10\,\mathrm{A}$ at $5\,\mathrm{Hz}$. (a) Conventional method. (b) Proposed method.

The experimental results of the proposed method under the step change in the amplitude of ac currents at low frequency ($5\,\mathrm{Hz}$) are shown in Fig. 4.10. From Fig. 4.10(c), it can be observed that the maximum ripple magnitude of the SM capacitor voltages is about $12\,\mathrm{V}$, which is much smaller compared to the $19\,\mathrm{V}$ of the conventional method shown in 2.21(c). Moreover, the dynamic response of the SM capacitor voltage with the conventional method is slower than that of the proposed method. As we have discussed in Section 2.3.2.2, the arm energy response caused by $v_{x\mathrm{N}}i_{zx}$ is slow due to the long fundamental period when MMC operates at low frequency. Instead, the proposed method adapts the instantaneous power to adjust the arm energy (capacitor voltage) so that the dynamic response of the SM capacitor voltage is faster and the

ripple magnitude of the capacitor voltage becomes smaller.

Another phenomenon that needs to be noted is the pattern of arm currents shown in Fig. 4.10(e), which is different from the pattern exhibited by the MMC operating at medium and high frequencies in Fig. 4.7(e) and Fig. 4.4(e). The pattern of the upper and lower arm currents at low frequency is interesting. The maximum value of these arm currents is close to the peak value of the related ac current and the minimum value is close to zero. Besides, these arm currents reach the maximum value alternately in the positive and negative half cycles of the corresponding ac current i_{sa}. It is not difficult to find that arm currents operating in this pattern is helpful for the suppression of capacitor voltage fluctuations. These two patterns of arm currents can reveal that the proposed method can automatically present different control modes according to different working conditions. For example, when the MMC operates at medium/high frequencies, in which case the ripple of the SM capacitor voltage is small, the proposed method mainly focuses on suppressing the circulating current. When the MMC works at low frequencies, as the ripple magnitude of SM capacitor voltage increases, the proposed method will mainly suppress the capacitor voltage ripple rather than eliminating the circulating current.

The spectrum and THD results of ac current i_{sa} at low frequency ($5\,\mathrm{Hz}$) are presented in Fig. 4.11 and Fig. 4.12, respectively. Not surprisingly, the proposed method still keeps a superior steady-state performance of the ac current, where the THD results are 3.86% and 2.86% for the proposed method compared to 4.37% and 3.77% for the conventional method.

4.4.3 Proposed FCS-MPC for MMC driving synchronous machine

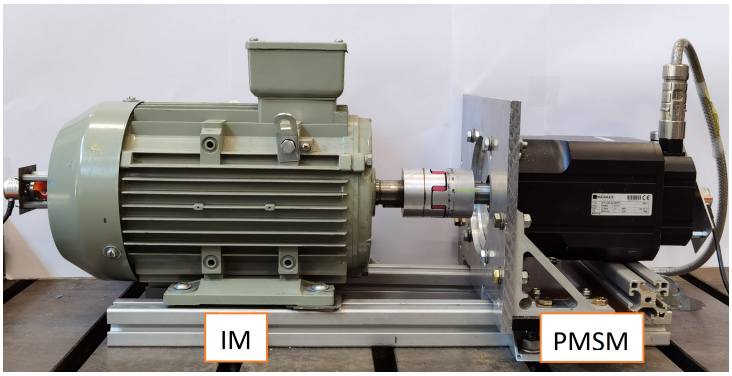

Figure 4.13: Setup of motor drive testbench. PMSM is driven by the MMC; induction machine (IM) works as a load and is driven by a commercial inverter.

To further evaluate the proposed FCS-MPC algorithm, the experimental results of the MMC driving a PMSM, shown in Fig. 4.13, has been given in this part. The parameters for the PMSM are listed in Table 4.1.

The experimental results of the MMC driving a PMSM at zero speed under the step change in torque ($2\,\mathrm{N\,m}$ to $3\,\mathrm{N\,m}$) are shown in Fig. 4.14. Since it is $0\,\mathrm{Hz}$, long-time ($30\,\mathrm{s}$) experimental results have been given to demonstrate the effectiveness of the proposed method. From Fig. 4.14, it can be seen that the SM capacitor voltages are well balanced at $0\,\mathrm{Hz}$ in both steady state and transient state. The circulating current shown in Fig. 4.14(b) oscillates with a relatively

Table 4.1: PMSM parameters

Name	Symbol	Value
Rated power	p_{rated}	2.76 kW
Rated stator line-line voltage	$u_{s,rated}$	400 V
DC-link voltage	u_{dc}	100 V
Rated mechanical angular speed	$\omega_{m,rated}$	314 rad/s
Stator resistance	R_s	0.95 Ω
Stator inductance	L_s	9.6 mH
Permanent-magnet flux linkage	ψ_{pm}	0.26 Wb
Pole pairs	n_p	3

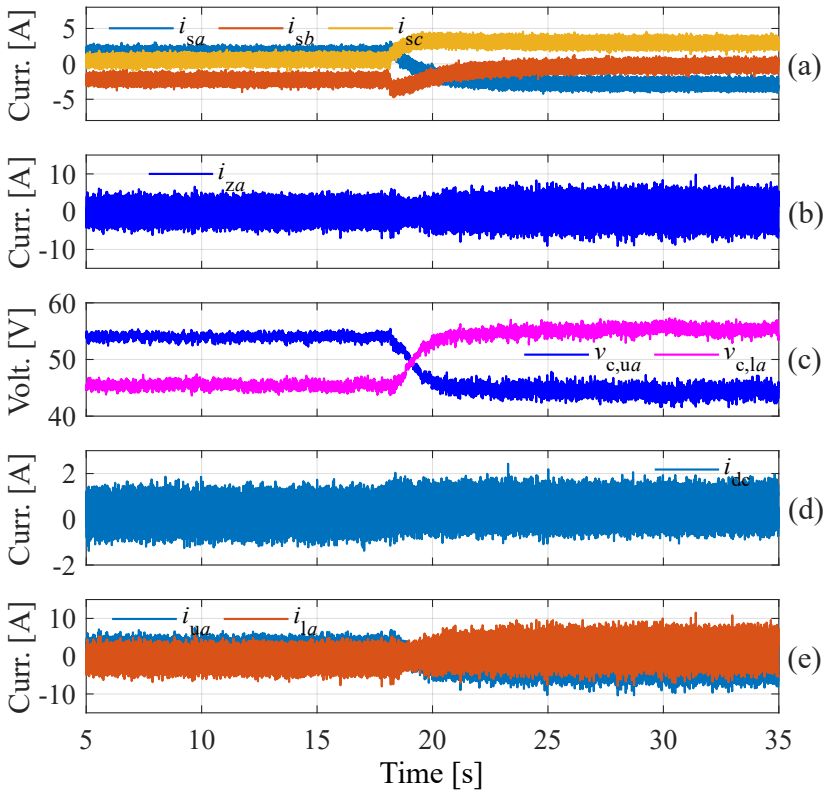

Figure 4.14: Performance of MMC driving a PMSM at zero speed under the step change in load torque condition (from 2 N m to 3 N m at 13 s).

high frequency around zero. In this way, neither the upper arm nor the lower arm of the MMC will keep accumulating power in the same direction. It should be noted that the operation mode of the proposed method in this case is similar to some control schemes with the circulating current injection technique. The pattern of the arm currents shown in Fig. 4.14(e) also verifies this point of view. A similar phenomenon can be found in Fig. 4.15.

Fig. 4.15 shows the results of the MMC driving a PMSM at extremely low frequency (1.5 Hz). The load torque in this case is 3 N m. From Fig. 4.15(a), it can be seen that the output currents are smooth and sinusoidal with the proposed method. The circulating current in Fig. 4.15(b) exhibits a similar pattern to that of the high-frequency circulating current injection method. It

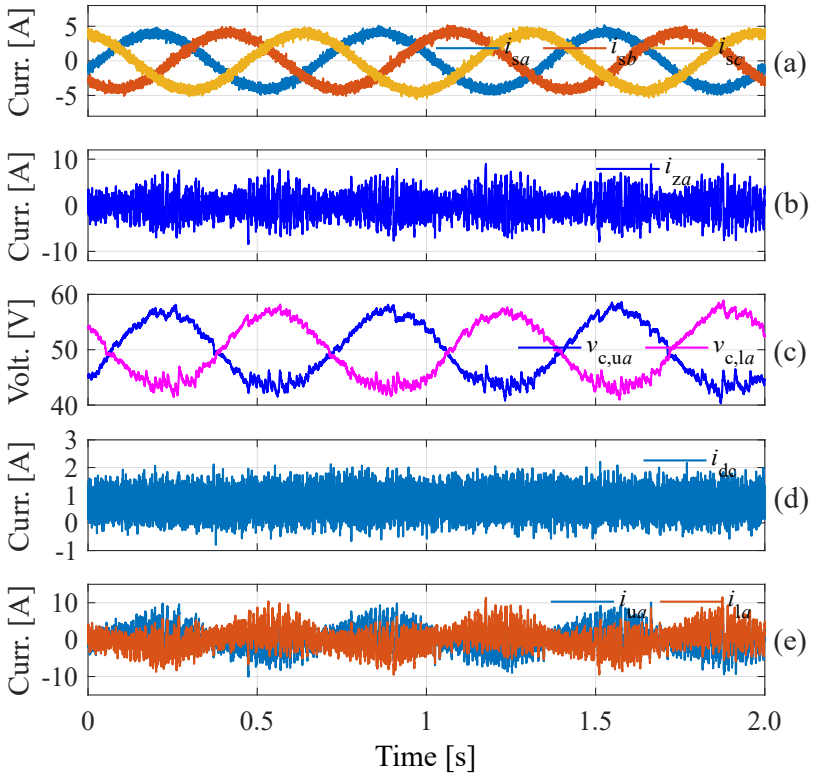

Figure 4.15: Steady-state performance of MMC driving a PMSM at low speed condition (1.5 Hz) with 3 N m load torque.

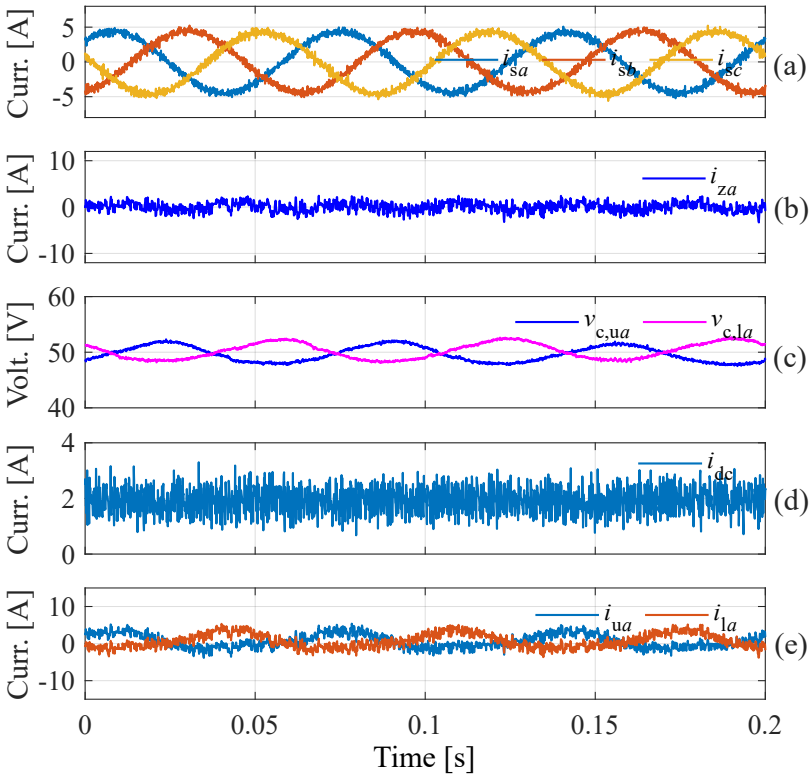

Figure 4.16: Steady-state performance of MMC driving a PMSM at high speed condition (15 Hz) with 3 N m load torque.

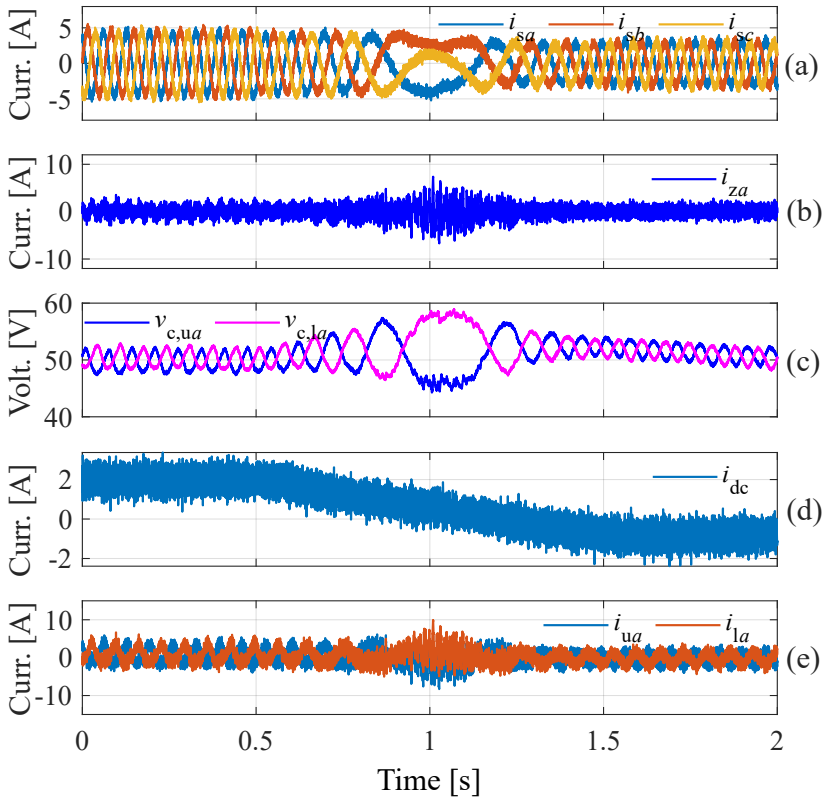

Figure 4.17: Performance of MMC driving a PMSM under speed reversal condition with $3\,\mathrm{N\,m}$ load torque (from $15\,\mathrm{Hz}$ to $-15\,\mathrm{Hz}$).

should be noted that this pattern presented from the circulating current and arm currents shown in Fig. 4.15(b) and (e) is not the same as any of the patterns in the previous experiments of MMC with RL load. In this pattern, the circulating current changes its direction many times within an output current cycle so that the low-frequency pulsating power present on MMC arms is converted into high-frequency power and thus the fluctuation of the SM capacitor voltage will be suppressed.

The experimental results of the MMC driving a PMSM at 300 rpm ($15\,\mathrm{Hz}$) are shown in Fig. 4.16. Note that the modulation index in this case is high. It can be seen that as the output frequency increases, the ripples of SM capacitor voltages are reduced. The arm currents shown in Fig. 4.16(e) exhibit a pattern similar to Fig. 4.7(e), but are different from those shown in Fig. 4.15. We can find that the proposed method can automatically exhibit different patterns according to the output frequency and modulation index to achieve the control of MMC, so the control of MMC at different frequencies no longer requires switching between different control methods.

At last, the speed reversal experiment over a large range of frequencies is presented in Fig. 4.17. It can be seen that as the speed decreases, the ripples of SM capacitor voltages, circulating current and arm currents will increase. The arm currents in Fig. 4.17(e) also present two different patterns during the speed reversal and it indicates that the proposed method can automatically generate different patterns to achieve the voltage balancing control of the SM capacitors in different cases. Therefore, no additional effort is required to use different control

schemes and/or to design the switching process for these different control schemes. The trade-off between the performance of the output currents and the suppression of the capacitor voltage ripple under different conditions can be guaranteed easily by using the proposed method.

4.4.4 Comparative experimental results of modulated MPC methods for MMC with RL load

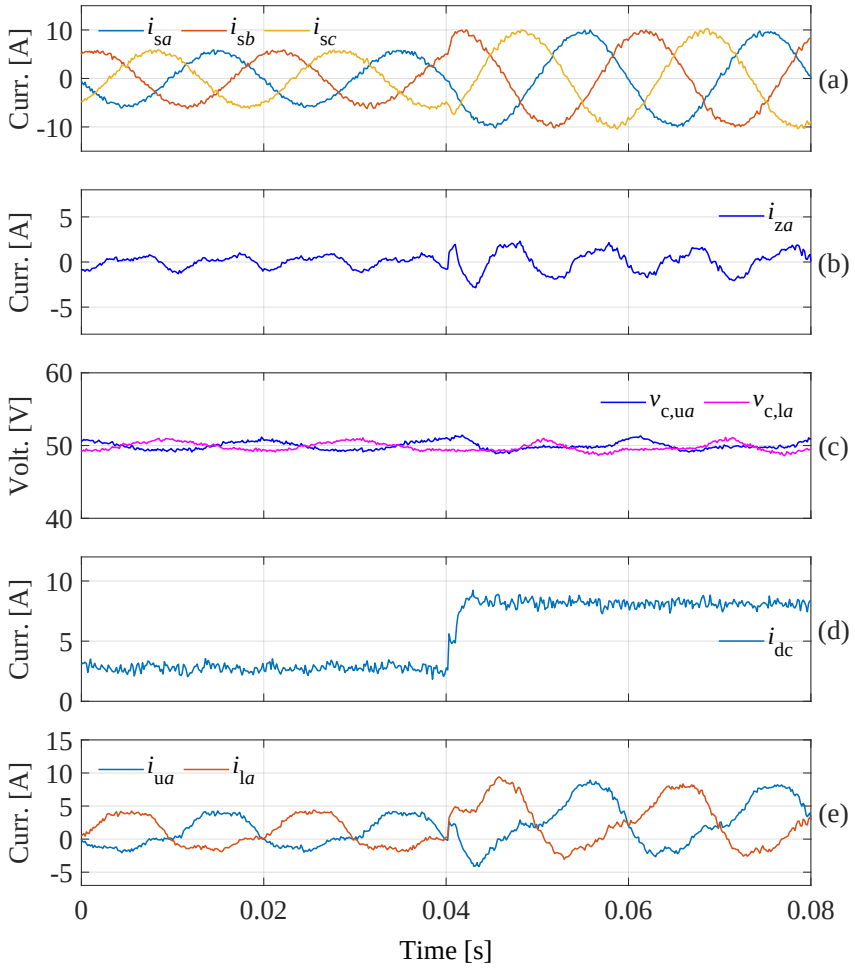

Figure 4.18: Step change in ac currents with the proposed modulated MPC at $50\,\mathrm{Hz}$.

In this section, the proposed modulated MPC scheme with a novel cost function will be compared with the conventional modulated MPC scheme which has been presented in Section 3.2.2. The sampling interval for both methods is set to 150 µs.

The experimental results of the proposed modulated MPC method under the step change in the amplitude (from $6\,\mathrm{A}$ to $10\,\mathrm{A}$) of the ac output currents at $50\,\mathrm{Hz}$ are shown in Fig. 4.18. Fig. 4.18(a) presents three-phase ac-side currents (i_{sa}, i_{sb} and i_{sc}) under such a related change. Fig. 4.18(b) shows the circulating current of phase a (i_{za}). The capacitor voltages of the upper and lower arms in leg a ($v_{c,ua}$ and $v_{c,la}$) is shown in Fig. 4.18(c). Fig. 4.18(d) shows the dc-link current (i_{dc}). At last, the arm currents are presented in Fig. 4.18(e).

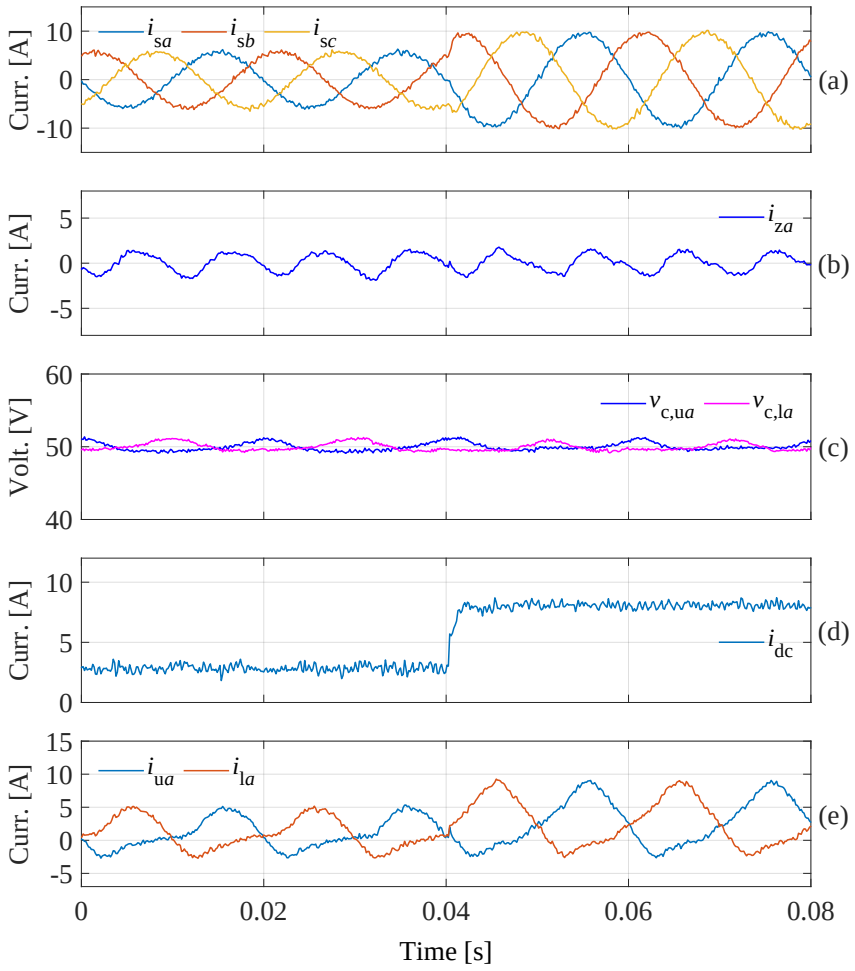

Figure 4.19: Step change in ac currents with the conventional modulated MPC at 50 Hz.

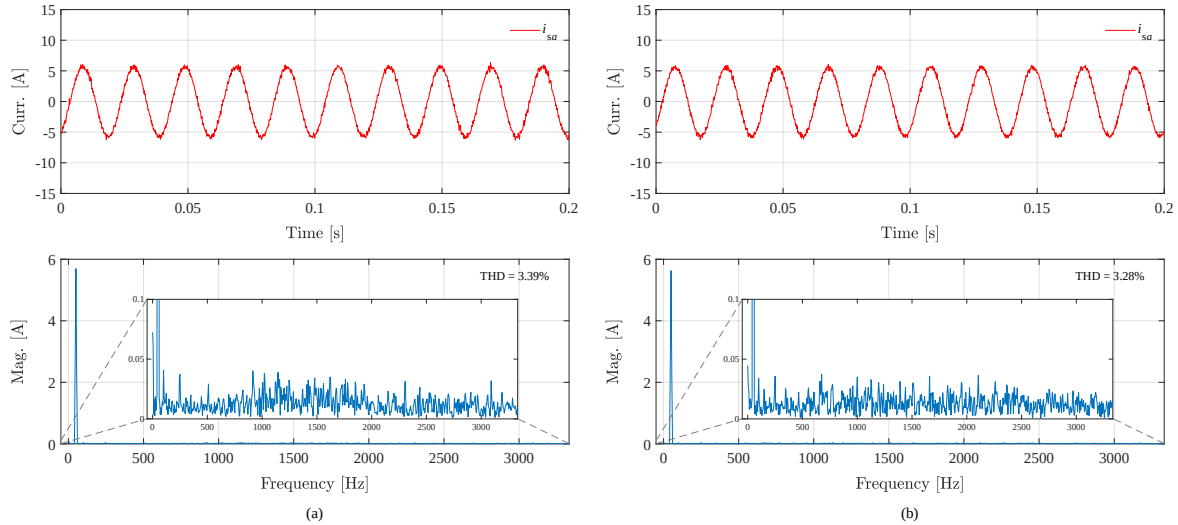

Figure 4.20: FFT analysis of the output current i_{sa} when the amplitude is 6 A at 50 Hz. (a) Conventional method. (b) Proposed method.

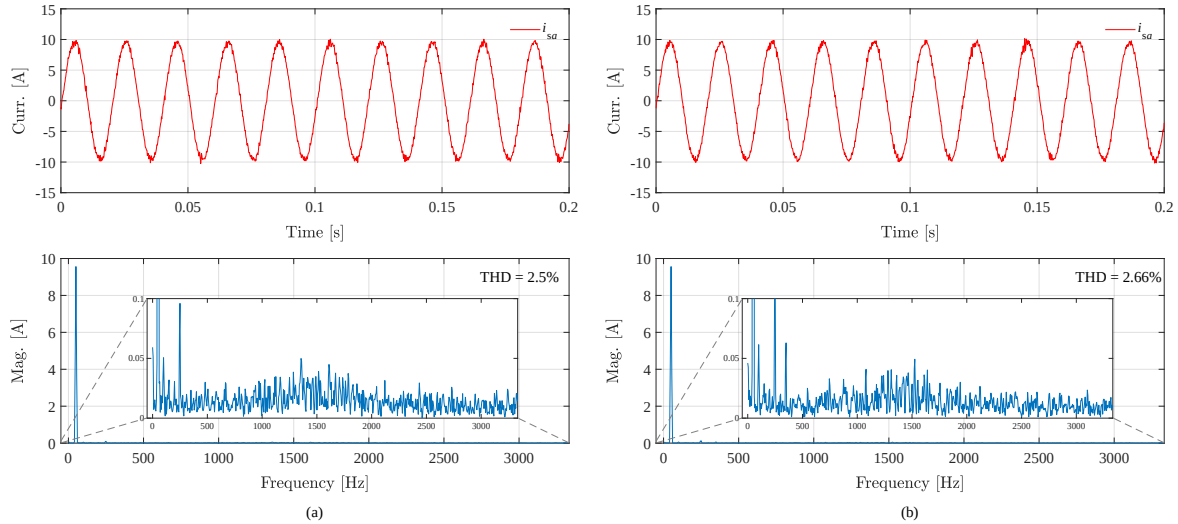

Figure 4.21: FFT analysis of the output current i_{sa} when the amplitude is 10 A at 50 Hz. (a) Conventional method. (b) Proposed method.

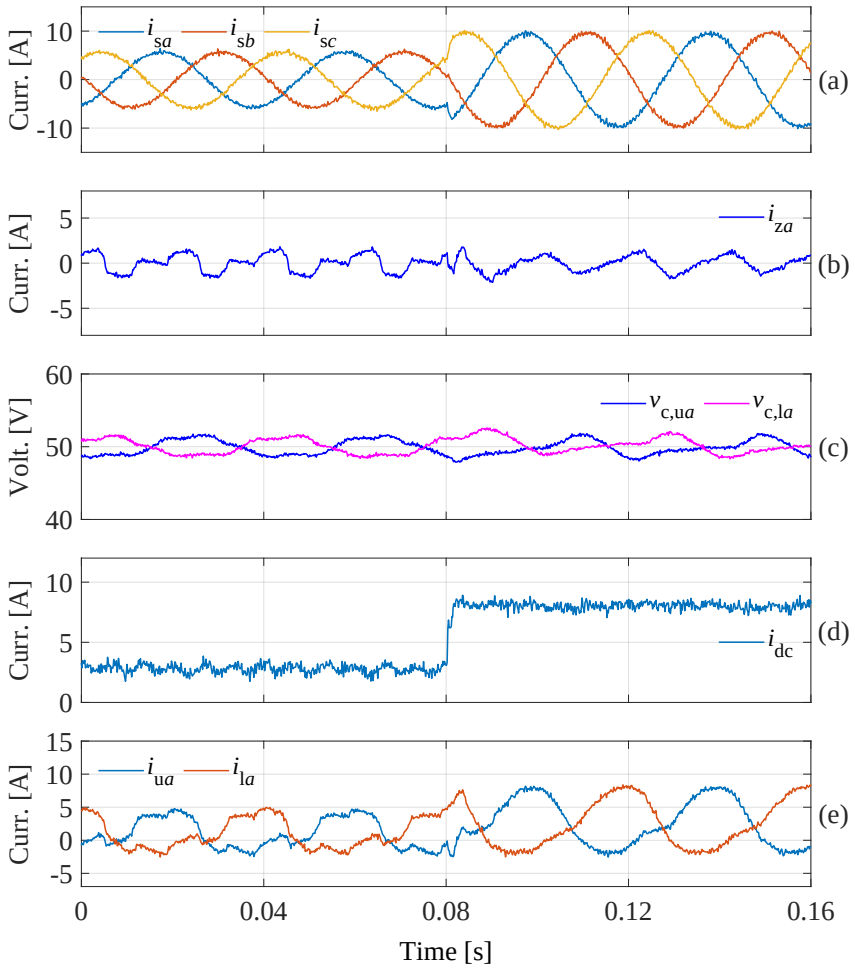

Figure 4.22: Step change in ac currents with the proposed modulated MPC at 25 Hz.

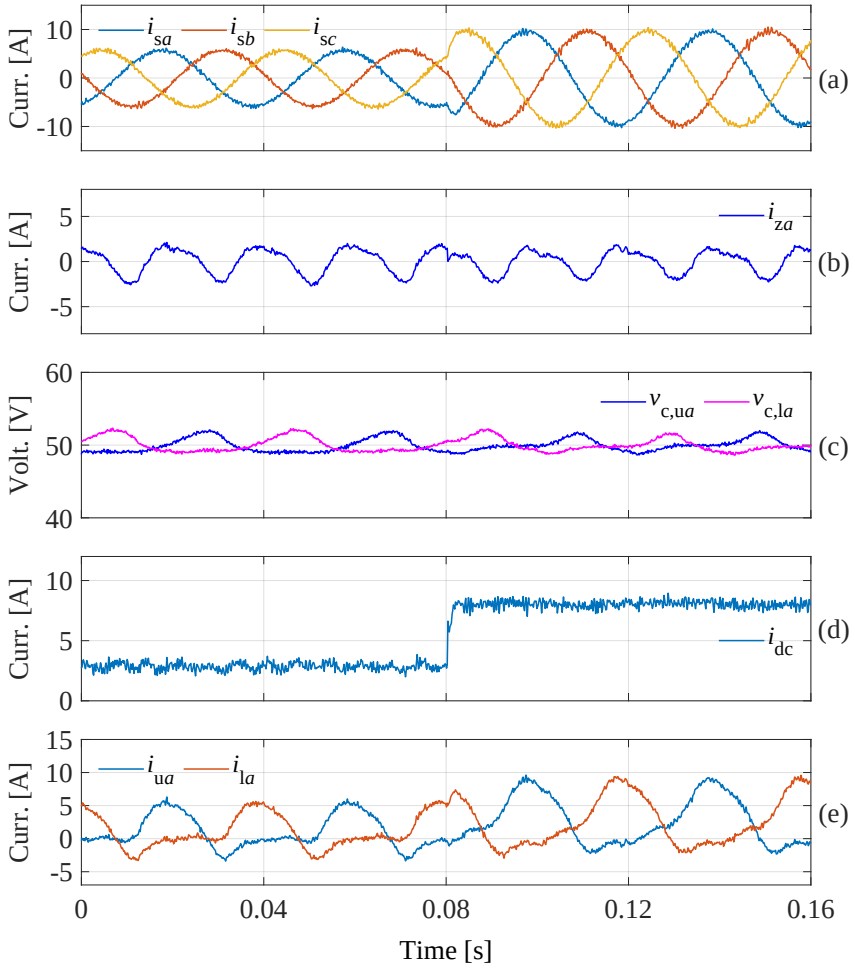

Figure 4.23: Step change in ac currents with the conventional modulated MPC at 25 Hz.

From Fig. 4.18, it can be seen that the dynamic response of ac-side currents, circulating currents and the dc-link current is fast. Besides, with the proposed method, the SM capacitor voltages of the upper and lower arms are well balanced. Therefore, it can be concluded that the proposed method with the novel cost function can work well at high frequency. The conventional modulated MPC scheme has been presented in Fig. 4.19. It can be seen that the circulating current of the proposed method is smaller than that of the conventional method when the amplitude of ac currents is 6 A. However, the dc-link current ripple is slightly higher than that of the conventional method when the amplitude of ac currents increases to 10 A. Besides, in this case, the circulating current of the proposed method increases and exhibits a significant second order harmonic component. In order to evaluate the steady-state performance of the proposed method, the FFT analysis and THD results for both methods under different conditions are shown in Fig. 4.20 and Fig. 4.21, respectively.

As it is shown in Fig. 4.20, when the amplitude of ac currents is 6 A, the THD result of the proposed method is only 3.28%, which is slightly lower than that of the conventional method (3.39%). However, when the amplitude of ac currents increases to 10 A, the THD result of the proposed method becomes 2.66%, while the THD of the conventional method is 2.5%.

The experimental results of the proposed method at 25 Hz are shown in Fig. 4.22. Compared

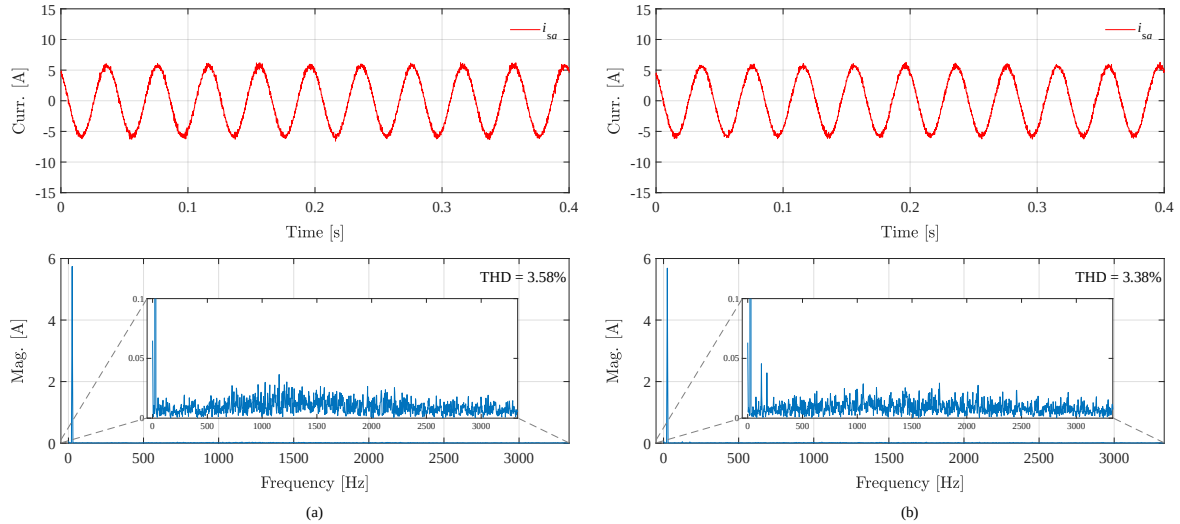

Figure 4.24: FFT analysis of the output current i_{sa} when the amplitude is $6\,\mathrm{A}$ at $25\,\mathrm{Hz}$. (a) Conventional method. (b) Proposed method.

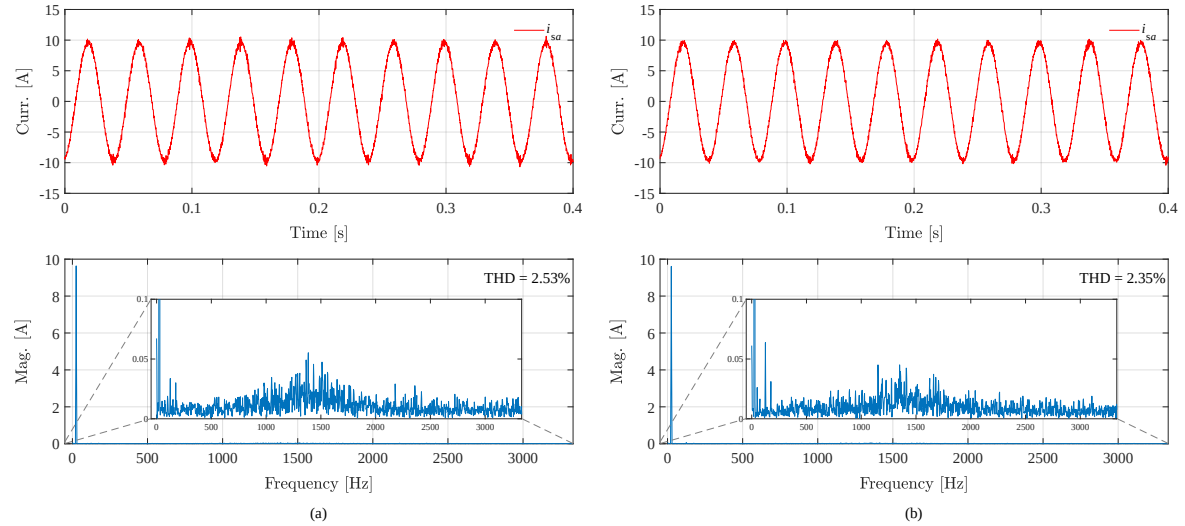

Figure 4.25: FFT analysis of the output current i_{sa} when the amplitude is $10\,\mathrm{A}$ at $25\,\mathrm{Hz}$. (a) Conventional method. (b) Proposed method.

with the conventional method shown in Fig. 4.23, the proposed method can achieve the better steady-state performance of the output ac currents shown in Fig. 4.24 and Fig. 4.25, and lower fluctuations of the circulating current shown in Fig. 4.22(b) under two different amplitudes of output ac currents ($6\,\mathrm{A}$ and $10\,\mathrm{A}$). It should be noted that with the proposed method, the fluctuation of the circulating current is always smaller than that of the conventional method at $25\,\mathrm{Hz}$ and $50\,\mathrm{Hz}$. This is because the ripple magnitude of SM capacitor voltage is small at $25\,\mathrm{Hz}$ and $50\,\mathrm{Hz}$, and thus a low circulating current is sufficient to regulate the SM capacitor voltage, which means that the proposed method can fully exploit the circulating current to control the SM capacitor voltage.

The experimental results of the proposed method under the step change in the amplitude of

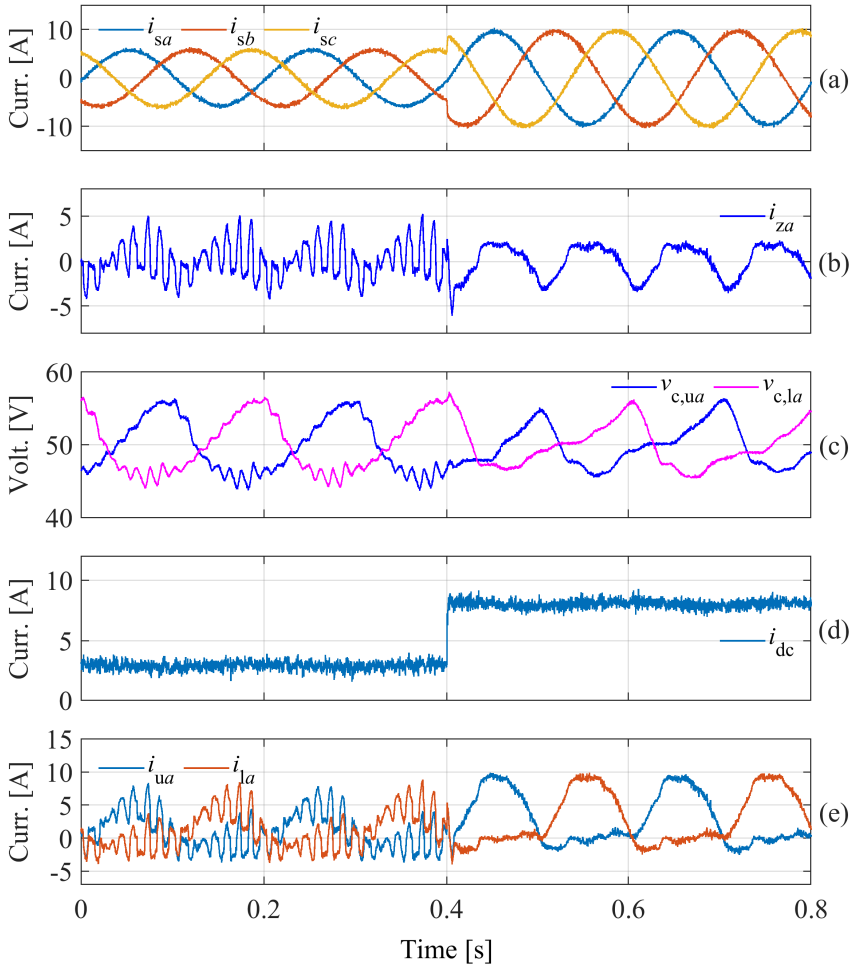

Figure 4.26: Step change in ac currents with the proposed modulated MPC at 5 Hz.

ac currents at low frequency (5 Hz) are shown in Fig. 4.26. It is worth noting that with the proposed method the circulating current shown in Fig. 4.26(b) presents a pattern similar to that of the methods with circulating current injection techniques in this case. Compared with the conventional method shown in 4.27, although the circulating current of the proposed method becomes larger, it can achieve smaller fluctuations of SM capacitor voltage. As we know, in the MMC system, large voltage fluctuations that cause instability of the MMC system should be avoided and a common measure is to sacrifice the amplitude of the circulating current to reduce the SM capacitor voltage fluctuation. From Fig. 4.26(c), it can be observed that the maximum ripple magnitude of the SM capacitor voltages is about 12 V, which is much smaller than the conventional method (17 V) shown in 4.27(c). In addition, conventional methods take longer than the proposed method to achieve voltage balancing between the upper and lower arm capacitors during transients. As discussed in Section 2.3.2.2, with the conventional method, the arm energy response caused by $v_{x\mathrm{N}}i_{zx}$ is slow due to the long fundamental period when MMC operates at low frequency. Instead, the proposed method regulates the arm energy (capacitor voltage) by adjusting its instantaneous power in real time, so that the dynamic response of the SM capacitor voltage is faster, and the fluctuations of the SM capacitor voltage becomes smaller.

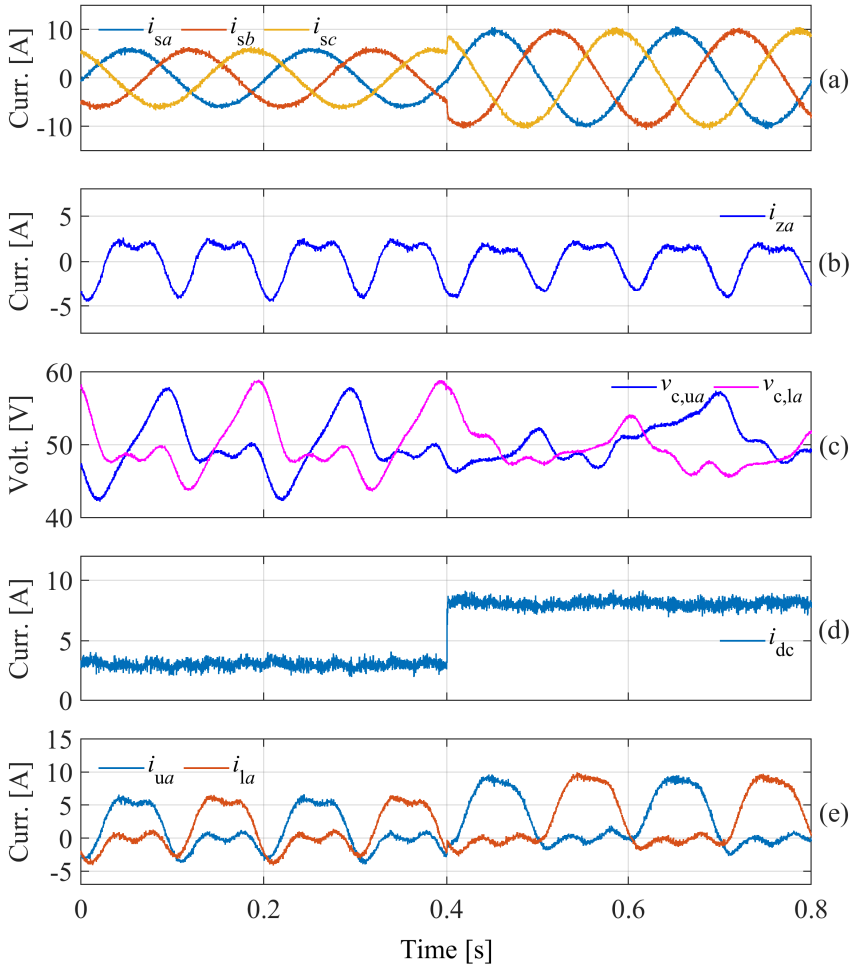

Figure 4.27: Step change in ac currents with the conventional modulated MPC at 5 Hz.

Note that from Fig. 4.26(e), we can also find that the pattern exhibited in arm currents is helpful for the suppression of capacitor voltage fluctuations. From Fig. 4.18, Fig. 4.22 and Fig. 4.26, it can verify that the proposed method can automatically present different control modes according to different working conditions. When the ripple magnitude of the SM capacitor voltage is small, the proposed method can limit the amplitude of the circulating current while ensuring the capacitor voltage balance between the upper and lower arms. When the MMC system operates at low frequencies, as the fluctuations of SM capacitor voltage become large, the proposed method will exhibit a similar pattern to the high-frequency circulating current injection method to eliminate the capacitor voltage ripples.

The spectrum and THD results of ac current i_{sa} at low frequency (5 Hz) are presented in Fig. 4.28 and Fig. 4.29, respectively. Not surprisingly, in such a low-frequency case, the proposed method keeps a superior steady-state performance of the ac current, where the THD results are 3.33% and 2.18% for the proposed method compared to 3.7% and 2.44% for the conventional method.

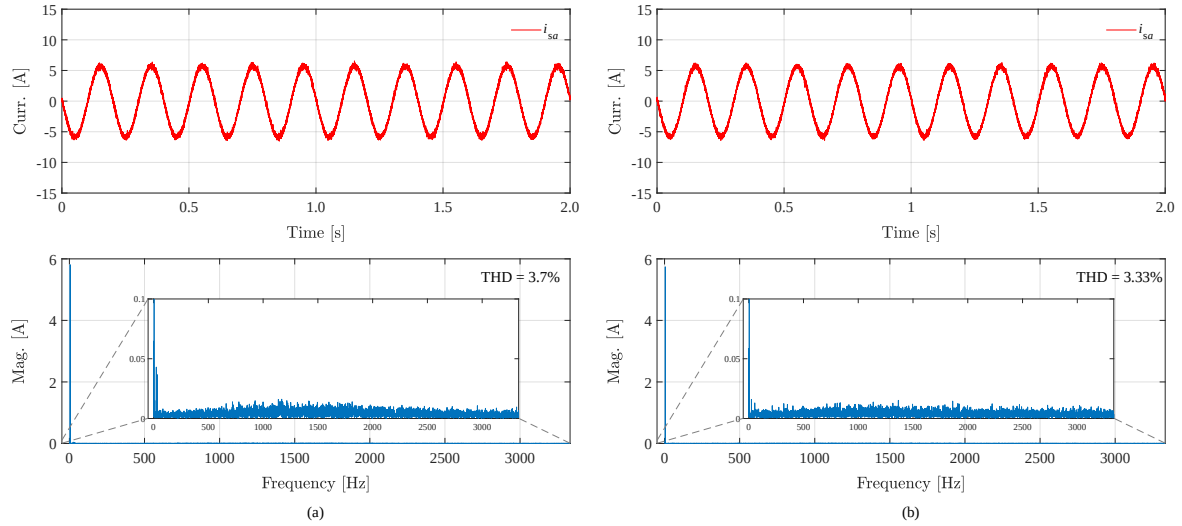

Figure 4.28: FFT analysis of the output current i_{sa} when the amplitude is $6\,\mathrm{A}$ at $5\,\mathrm{Hz}$. (a) Conventional method. (b) Proposed method.

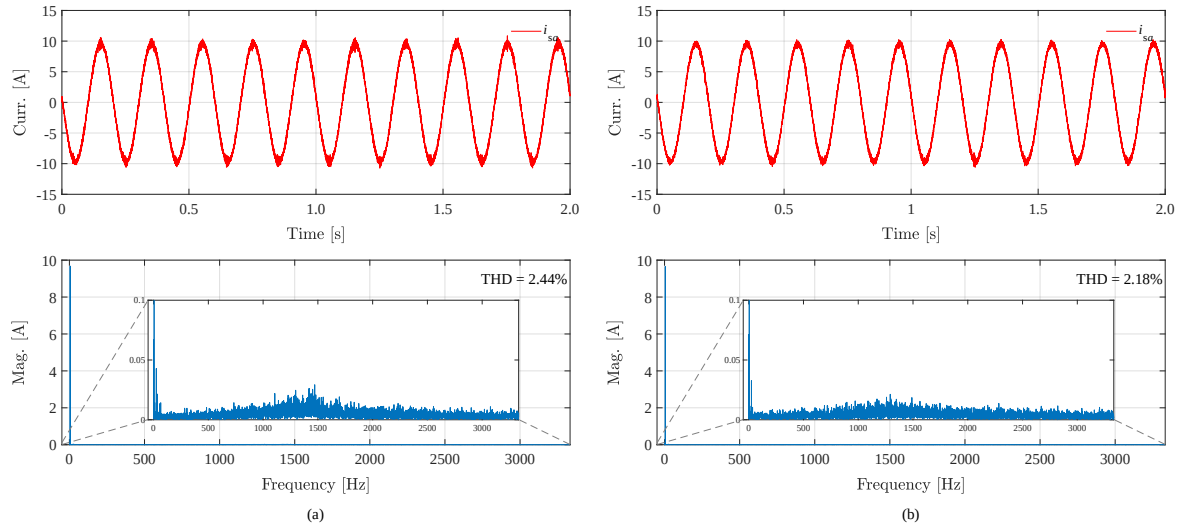

Figure 4.29: FFT analysis of the output current i_{sa} when the amplitude is $10\,\mathrm{A}$ at $5\,\mathrm{Hz}$. (a) Conventional method. (b) Proposed method.

4.5 Summary

In this chapter, a novel cost function for the MPC method has been designed to realize the MMC system operating at a wide frequency range. In order to reduce the computational burden and improve the steady-state performance of the output currents, it is necessary to find a modulated way to implement MPC with this novel cost function. Therefore, an exhaustive active-set method has been proposed to obtain the optimal solution for the modulated MPC scheme. The comparative experiments show that by applying this novel cost function, the proposed method

not only achieves satisfactory performance in the low-frequency condition but also works effectively at high frequency. In addition, the proposed MPC method can automatically present different control modes according to different working conditions. It can be seen that when the ripple magnitude of the SM capacitor voltage is small, the proposed method will mainly focus on suppressing the circulating current while ensuring the capacitor voltage balance between the upper arm and lower arm. When the fluctuations of SM capacitor voltage become large, the proposed method will exhibit a similar pattern to the high-frequency circulating current injection method to eliminate the capacitor voltage ripples. The experimental results have verified the effectiveness of the proposed method at low frequency, medium frequency, and high frequency. Also, the experimental results of the MMC driving a PMSM at various speed conditions have been given to further check the effectiveness of the proposed method.

CHAPTER 5

Model predictive control for modular multilevel converters operating in quasi-two-level mode

5.1 Introduction

As mentioned in the former chapter, an alternative method to enable MMCs to operate at low frequencies is to make MMCs operate in Quasi-Two-Level (Q2L) mode [62–65]. This method mimics the standard two-level voltage source inverter (VSI) to reduce the charging or discharging time of the MMC branches/arms. However, instead of the rectangle waveform for a two-level VSI, a staircase waveform for the quasi-two-level mode has been employed to limit the $\mathrm{d}v/\mathrm{d}t$. By applying this operation mode, long-time charging and/or discharging for SM capacitors can be decreased. Considering an ideal case in a steady state, all SMs in the upper arm are inserted and all SMs in the lower arm are bypassed. The output current is provided by the bypassed arm (lower arm) and the current in the inserted arm (upper arm) will be 0. In this case, SM capacitors in both arms will not be charged or discharged. The arm energy variation only occurs during the commutation process, which will not last long. In other words, SM capacitors will not be charged or discharged over a long time in the quasi-two-level operation mode. This is why operating the MMC in this mode can significantly reduce the energy variation.

From the above analysis, we can find that the superior multilevel output voltage will be sacrificed by applying the Q2L mode. Therefore, when MMC operates in this mode, the THD for output currents will be similar to that of the two-level VSI. This is the main drawback of this operation mode. However, on the other hand, as the Q2L mode significantly attenuates the branch energy variation, the SM capacitance can be greatly reduced compared to the conventional operation mode. Besides, due to the limitation of the $\mathrm{d}v/\mathrm{d}t$ by using the staircase waveform, the branch/arm inductance can also be decreased. Therefore, when MMC operates in Q2L mode, its volume can be small, which is another advantage for industrial applications.

The difficulty in implementing Q2L mode for the MMC is the arm current commutation control. To minimize the arm energy variation, the output current should be provided entirely by the

bypassed arm after the commutation. It requires that the commutation control algorithm should regulate arm currents to their reference values while the MMC completes the commutation. In order to achieve this control target, an MPC method with an extrapolation technique has been proposed to control the arm current commutation process. In this method, the SMs in arms will be determined to delay or bypass each step during the commutation process. Note that these delays can help the MMC complete the commutation. In addition, with this method, MMC can complete the commutation process as quickly as possible. As the commutation process can be completed quickly, the voltage fluctuation of SM capacitors will be suppressed significantly even if the MMC is operating at zero/low frequencies. The simulation and experimental results verify the effectiveness of the proposed method.

5.2 Quasi-two-level operation mode

In the conventional operation mode of MMCs. It employs a cascaded connection of SMs to reach the desired multilevel output voltage. In order to achieve such multilevel voltage waveforms, some SMs should insert into the circuit for a certain time and supply the load currents while the corresponding arm current will charge or discharge these SM capacitors. Therefore, at low-frequency conditions, the inserted SMs will experience a longtime charging or discharging process in this operation mode, resulting in a large voltage fluctuation in the SM capacitor.

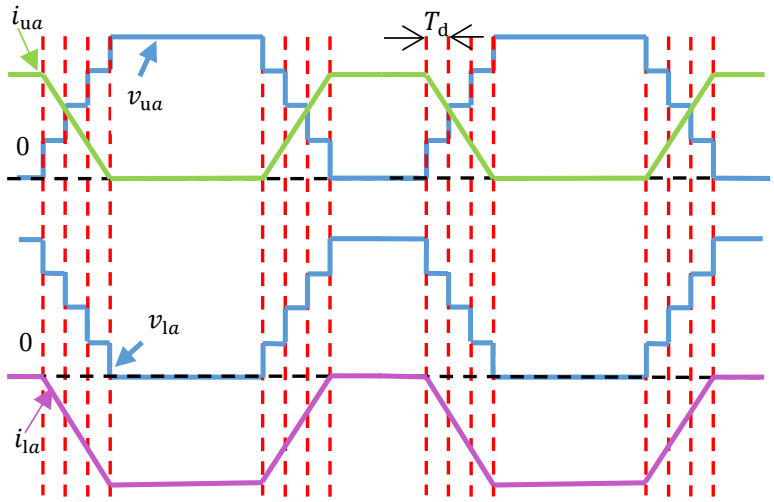

Figure 5.1: Idealized waveforms for the Q2L operation mode: arm voltages and arm currents.

The quasi-two-level operation mode of MMC is to mimic the classical two-level VSI operation mode. It is known that the power fluctuation in each arm (or IGBT) of VSI is extremely small. This is because the high voltage and the large current will not be supplied by the same arm (or IGBT) simultaneously. For example, the lower arm sustains the dc-link voltage but the current is zero. Instead, the upper arm supplies a large current but the voltage is small. The quasi-two-level operation mode of MMCs derives from such a phenomenon. To limit the high $\mathrm{d}v/\mathrm{d}t$, the ideal square waveform like the two-level VSI will not be suitable for MMCs. Instead, the SMs should be inserted or bypassed one by one with a small time interval T_d, resulting in a staircase waveform. The ideal quasi-two-level operation mode for MMCs is presented in

Fig. 5.1. It can be seen that when all SMs of the upper arm are inserted, the current flowing through this arm is zero. Instead, the load current is provided entirely by the lower arm while all SMs in this arm are bypassed under such a condition. Therefore, the charging or discharging process is eliminated at a steady state and thus the capacitor voltage variation is suppressed. In the ideal case, the voltage fluctuation results only from the current commutation process between the upper and lower arms.

To achieve such an operation mode, the control for the arm current commutation process is required. Unlike the two-level VSI, the upper arm and lower arm in the same phase leg are connected by two arm inductors. Therefore, the current commutation process of MMCs cannot be finished instantly. The rate of the arm current commutation depends on the arm inductance. A proper voltage can be applied to the arm inductors to force the load current transfer from one arm to the other one. Due to the voltage fluctuation occurring during the arm current commutation process, the duration of this process should be as short as possible. The control method that can satisfy these requirements for the current commutation process will be presented in the following Section 5.4.

5.3 Control scheme for MMC in the quasi-two-level operation mode

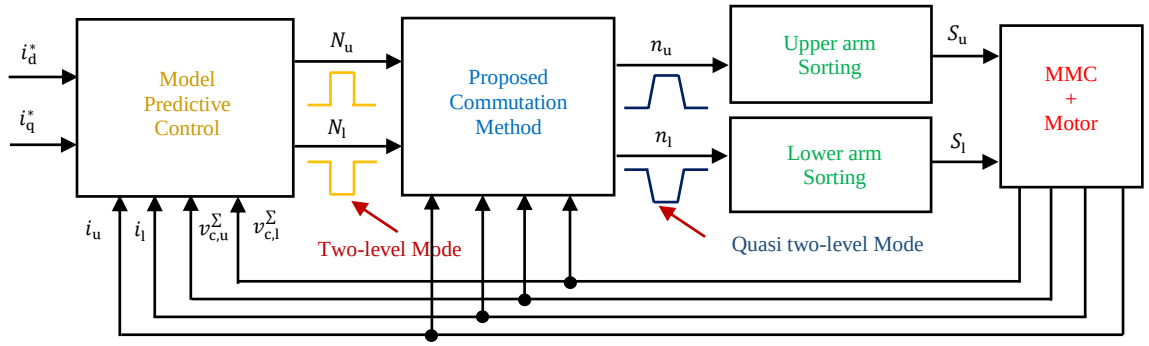

Figure 5.2: Control scheme for the MMC operating in the quasi two-level mode.

The overall control block diagram for the MMC system has been presented in Fig. 5.2. It includes the output current control, circulating current control (arm current commutation control) and capacitor voltage balancing control. These controllers are cascaded with each other to implement the Q2L operation mode of MMCs [68].

The MPC method has been used to control the output currents. The reference values i_d^* and i_q^* are obtained from the speed control (or torque control) for the motor. Different from the conventional multilevel operation mode of MMC, there are only two statuses for each arm in the Q2L mode at steady state, all SMs bypassed or inserted. Besides, the upper arm and lower arm in the same phase have the opposite status. For example, if the insertion index of the upper arm is N, the insertion index of the lower arm should be 0. Therefore, for the three-phase MMC, only 2^3 operating states need to be evaluated. The selected insertion index for each arm derived from the MPC controller will be passed to the circulating current controller to realize the arm

current commutation control. It should be noted that the output currents and circulating currents are not controlled in a parallel manner. Instead, they are cascaded to each other. It requires that the sampling frequency of the circulating current controller ($1/T_{\mathrm{d}}$) should be high enough to accomplish a fast current commutation without affecting the output current. Therefore, the arm inductance of L is usually chosen small, otherwise, a long commutation period will cause the degradation of output currents.

For the circulating current control method, more details will be given in the following section. In brief, the function of this controller is to convert the two-level square waves (insertion indices, N_{u} and N_{l}) given by the output current controller into the staircase waves (n_{u} and n_{l}) and complete the commutation process at the same time.

The capacitor voltage balancing control method is also required to keep the capacitor voltages of all the SMs in the same arm balanced. In this chapter, the classical capacitor voltage balancing method based on the sorting algorithm has been applied [69]. It should be noted that the sorting algorithm is only activated during the current commutation process, which is different from the conventional voltage balancing control operating in the multi-level PWM mode.

5.4 Proposed control method

In order to describe the proposed control method conveniently, the current commutation process of an MMC with 4 SMs in each arm is considered as an example, as shown in Fig. 5.3. In this

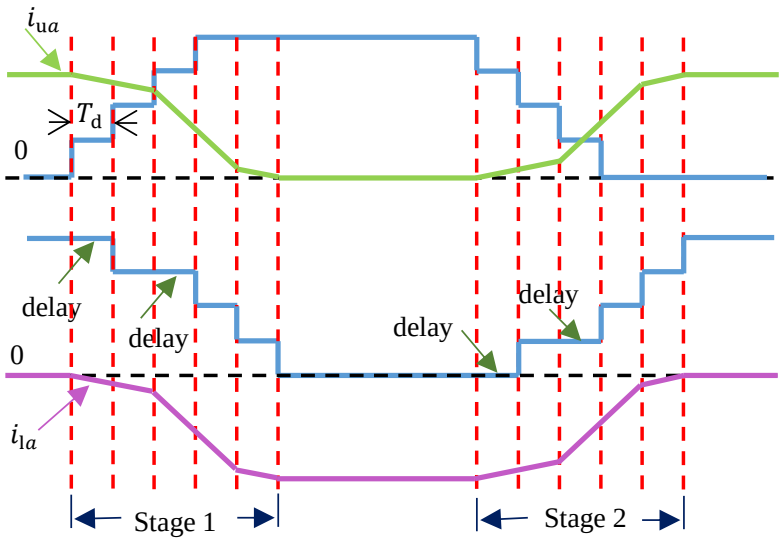

Figure 5.3: Commutation process of the quasi two-level mode.

case, the output current i_{sa} is positive and it can be expressed as $i_{sa} = i_{ua} - i_{la}$. The circulating current $i_{cira} = (i_{ua} + i_{la})/2$ in the quasi two-level mode has been employed to realize the current commutation algorithm. For example, at stage 1 in Fig. 5.3, the desired state i_{ua} should be regulated to 0 and i_{la} should provide the entire output current $-i_{sa}$ after the arm current commutation. Due to the relatively large inductors for the output side and a short commutation period, i_{sa} can be seen as constant during a control period. Therefore, the control task can be changed to regulate the circulating current i_{cira} from $i_{sa}/2$ to $-i_{sa}/2$. In this case, the voltage

in phase a should be larger than the dc-link voltage V_{dc} for certain time in the commutation process according to (5.1).

$$\Delta i_{\mathrm{cir}a} = T_{\mathrm{d}} \frac{V_{\mathrm{dc}} - v_{\mathrm{ph}a}}{2L}, \tag{5.1}$$

where T_{d} is the unit dwell time interval, which is inserted between the SM switching instants to limit the $\mathrm{d}v/\mathrm{d}t$ and generate the staircase waveform for the arm voltage. $v_{\mathrm{ph}a}$ is defined as

$$\begin{aligned} v_{\mathrm{ph}a} &= \frac{n_{\mathrm{u}a}}{N} \sum_{i=1}^{N} v_{\mathrm{c,u}a}^{i} + \frac{n_{\mathrm{l}a}}{N} \sum_{i=1}^{N} v_{\mathrm{c,l}a}^{i} \\ &= n_{\mathrm{u}a} \bar{v}_{\mathrm{c,u}a} + n_{\mathrm{l}a} \bar{v}_{\mathrm{c,l}a}, \end{aligned} \tag{5.2}$$

where $n_{\mathrm{u}a}$ and $n_{\mathrm{l}a}$ are insertion indices. It can be seen that when i_{sa} is positive, the upper arm will experience NT_{d} to insert (stage 1) or bypass (stage 2) all the SMs, while the lower arm will take longer time (more than NT_{d}) to help complete the commutation of the whole phase. The operating mode of each arm during the commutation can be found in Fig. 5.3.

In order to achieve the control target $i_{\mathrm{cir}a}$ from $i_{\mathrm{s}a}/2$ to $-i_{sa}/2$ at stage 1 or $i_{\mathrm{cir}a}$ from $-i_{sa}/2$ to $i_{sa}/2$ at stage 2, the MPC with extrapolation technique has been applied. Here, we will only consider the case in stage 1 without loss of generality. The SMs in the upper arm will be inserted step by step at each dwell time interval (T_{d}). While at each sampling period, SMs in the lower arm will be judged whether to be directly bypassed or delayed. The judgment principle is to compare the final value of circulating current $i_{\mathrm{cir}a}$ with its desired value $-i_{sa}/2$ and choose the operation (delay or bypass the SM in the lower arm) which can minimize the absolute value of the error $e = |-i_{sa}/2 - i_{\mathrm{cir}a}|$.

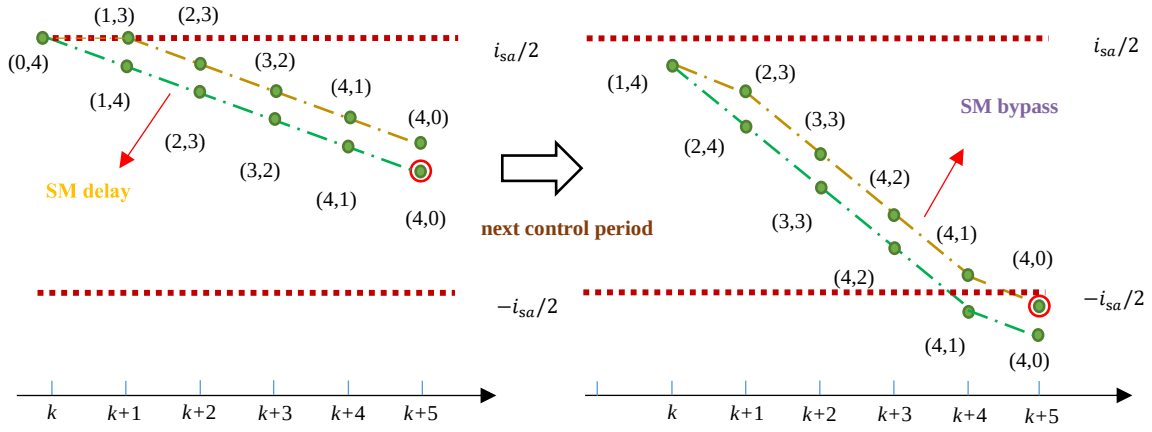

Figure 5.4: Two candidate switching sequences and the resulting circulating current trajectories when extrapolation is used.

In order to derive the prediction model for the final value of the circulating current, the following case will be considered, which is shown in Table 5.1. The insertion index of the upper arm $n_{\mathrm{u}a}$ changes from 0 to 1, which means that one SM has been inserted into the circuit. While the insertion index of lower arm $n_{\mathrm{l}a}$ can change from 4 to 3 (bypass case) or keep at 4 (delay case). Then we assume that there can only be 'one delay' in the whole commutation process at the present control period. For the delay case, it is obvious to get 'one delay'. For the

Table 5.1: Commutation process with 'one delay'

time	$n_{\mathrm{u}a}$	$n_{\mathrm{l}a,d}$ (delay)	$n_{\mathrm{l}a,p}$ (bypass)
k (Start)	1	4 (delay)	3 (bypass)
$k+1$	2	3	3 (delay)
$k+2$	3	2	2
$k+3$	4	1	1
$k+4$ (End)	4	0	0
Sum (End)	$n_{\mathrm{u}a,\mathrm{sum}}=14$	$n_{\mathrm{l}a,d,\mathrm{sum}}=10$	$n_{\mathrm{l}a,p,\mathrm{sum}}=n_{\mathrm{l}a,d,\mathrm{sum}}-1$

bypass case mentioned above, we prefer to let this 'one delay' occur at the next moment. This method is similar to the greedy algorithm. Fig. 5.4 reveals the principle of the proposed method. Note that only two candidate switching sequences are considered in this method and different switching sequence selection criteria may result in different performance for the commutation process. Then the final values of the circulating current used for the judgment at the present control period can be expressed as:

$$i_{\mathrm{cir}a,d}=i_{\mathrm{cir}a}(k)+\frac{T_{\mathrm{d}}}{2L}\left((n_{\mathrm{l}a}+1)V_{\mathrm{dc}}-n_{\mathrm{u}a,\mathrm{sum}}\bar{v}_{\mathrm{c},\mathrm{u}a}-n_{\mathrm{l}a,d,\mathrm{sum}}\bar{v}_{\mathrm{c},\mathrm{l}a}\right), \tag{5.3}$$

$$i_{\mathrm{cir}a,p}=i_{\mathrm{cir}a}(k)+\frac{T_{\mathrm{d}}}{2L}\left((n_{\mathrm{l}a}+1)V_{\mathrm{dc}}-n_{\mathrm{u}a,\mathrm{sum}}\bar{v}_{\mathrm{c},\mathrm{u}a}-n_{\mathrm{l}a,p,\mathrm{sum}}\bar{v}_{\mathrm{c},\mathrm{l}a}\right). \tag{5.4}$$

The cost functions are defined as

$$g_d=\left|\frac{-i_{\mathrm{s}a}}{2}-i_{\mathrm{cir}a,d}\right|, \tag{5.5}$$

$$g_p=\left|\frac{-i_{\mathrm{s}a}}{2}-i_{\mathrm{cir}a,p}\right|. \tag{5.6}$$

These two cost functions can be used to decide whether the SM in the lower arm is delayed or directly bypassed. It can be observed that if $g_d<g_p$, the SM in the lower arm should be delayed to bypass. Otherwise, the SM will be bypassed directly. In the present control period, the SM from the lower arm should be determined whether to be bypassed or not and in the following steps, this judgment process will be repeated until the commutation is completed.

5.5 Simulation results for the MMC-based motor drives

To verify the proposed arm current commutation control method in this chapter, a scaled-down three-phase MMC inverter with 4 SMs per arm driving a permanent magnet synchronous motor (PMSM) is simulated in Matlab/Simulink. The parameters are shown in Table 5.2.

In Fig. 5.5, the simulation results of the MMC system using the proposed method are presented. It should be noted that the speed of PMSM is regulated by a PI controller and stator currents are regulated by MPC, as shown in Fig. 5.2. Firstly, the proposed method has been tested under the start-up condition from 0 to 100 $\mathrm{r/min}$ with a small load torque. It can be observed that the load current in phase a is alternately provided by the upper and lower arms in

Table 5.2: Simulation Parameters

MMC parameters		
Name	Symbol	Value
DC link voltage	V_{dc}	560 V
Number of SMs per arm	N	4
Nominal SM capacitor voltage	$V_{\mathrm{c,rated}}$	140 V
SM Capacitance	C_{SM}	3.3 mF
Arm Inductance	L	1 mH
Unit delay	T_{d}	10 µs
Control period	T_{s}	120 µs
PMSM parameters		
Moment of inertia	J	0.005 445 kg m^2
Stator resistance	R_s	0.85 Ω
Stator inductance	L_s	9.6 mH
Permanent-magnet flux linkage	ψ_{pm}	0.27 Wb
Pole pairs	n_p	4

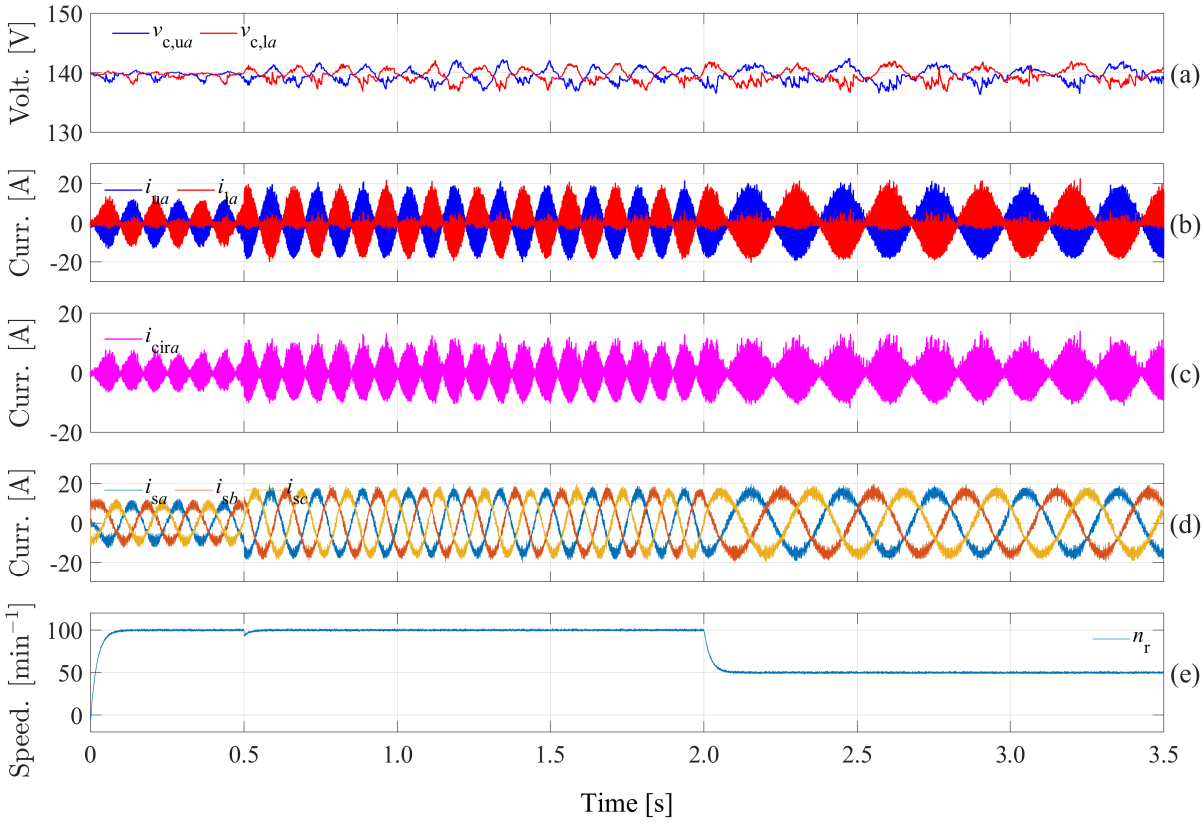

Figure 5.5: Simulated waveforms of MMC operating in Q2L mode with the proposed arm current commutation method.

Fig. 5.5(b). The capacitor voltage ripples are small under the start-up condition due to the light load, as shown in Fig. 5.5(a). A load torque has been added at $t = 4\,\mathrm{s}$. The voltage fluctuation has been increased but still kept at a small range. At last, the speed has further reduced to $50\ \mathrm{r/min}$ to test the proposed method. The capacitor voltage ripple is slightly increased compared to the previous case where the speed doubled. It can be seen that the voltage fluctuation not only depends on the magnitude of load currents, but the speed (output frequency) also has an effect on it. The proposed method can effectively and significantly suppress the capacitor voltage ripples even under the large output current condition. It can be found that the voltage fluctuation of each SM capacitor is very small ($\pm 4\,\mathrm{V}$ with the rated SM capacitor voltage) throughout the whole test. However, due to the sacrifice of the multilevel output waveform, the ripples of output currents are large.

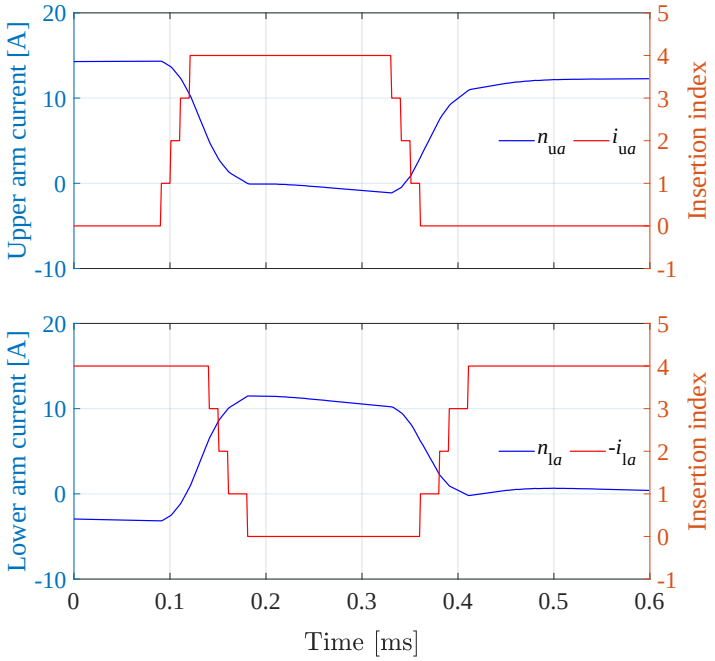

Figure 5.6: Detailed waveforms of insertion indices and arm currents using the proposed arm current commutation method.

In Fig. 5.6, the detailed waveforms of the insertion indices and arm currents are presented. The details of the upper and lower arm operation mode are presented. At the rising stage (like stage 1 in Fig. 5.6), SMs in the upper arm are inserted one by one while SMs in the lower arm are bypassed in turn but with some 'delay'. The upper arm current decreases to about 0 after the commutation process and the lower arm provides the load current at the same time. It can be found that when the arm voltage is large, its current always remains small. The large energy fluctuation only occurs during the commutation process. Besides, the upper arm and lower arm support the output current alternately by using the proposed method. It can be observed that when the insertion index of either of each arm is equal to the number of SMs in this arm (N), the current flowing through this arm stays low and vice versa, which can indicate the effectiveness of the proposed method.

5.6 Experimental results

A two-phase MMC platform with 2 SMs per arm has been used for verification. A resistor-inductor (RL) load is connected to the terminals of these two phases. System parameters are listed in Table 5.3.

Table 5.3: Experimental Parameters

Two-phase MMC parameters		
Name	Symbol	Value
DC link voltage	V_{dc}	100 V
Nr. of SMs per arm	N	2
SM Capacitance	C_{SM}	5.04 mF
Arm Inductance	L	1.9 mH
Unit delay	T_{d}	30 µs
Control period	T_{s}	300 µs
Load resistance	R_s	10.38 Ω
Load inductance	L_s	9.5 mH

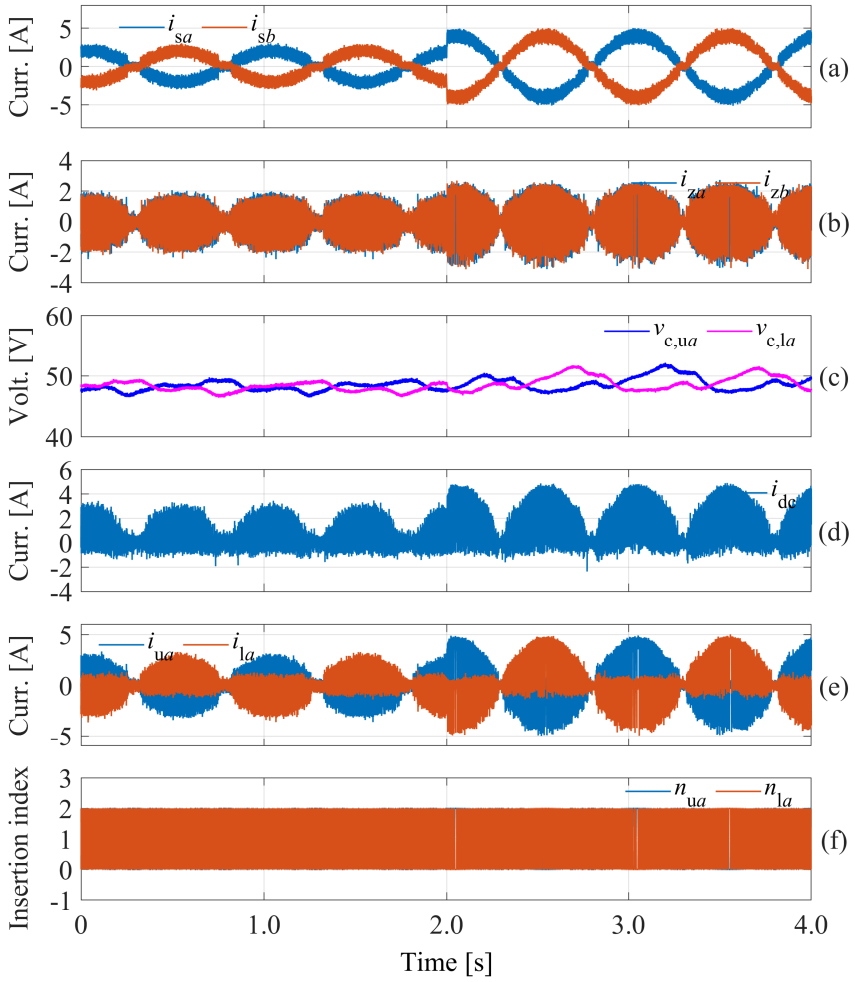

Figure 5.7: Step change in output currents with the proposed method at 1 Hz.

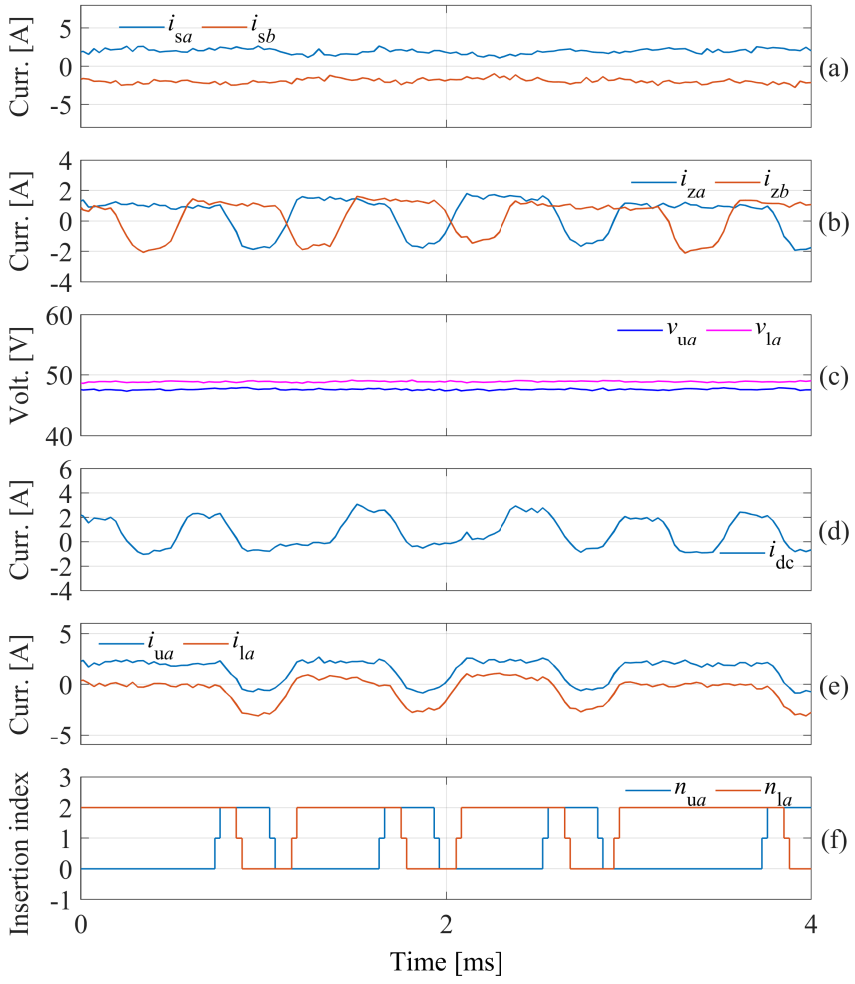

Figure 5.8: Detail waveforms with the proposed method at 1 Hz.

Fig. 5.7 presents the experimental results of MMC operating in Q2L mode at 1 Hz with the proposed method. From Fig. 5.7(c), it can be seen that the ripple magnitude of the capacitor voltage is small even if the output frequency is extremely low. The arm currents shown in Fig. 5.7(e) alternate their operating mode many times during a fundamental period. The same is true for the circulating currents in Fig. 5.7(b). The amplitude of the circulating currents is approximately half of the output current amplitude, which is consistent with the control objective for the proposed method, as discussed in Section 5.4. Although the output current presented in Fig. 5.7(a) is sinusoidal, its ripple is relatively large.

It is worth noting that the dynamic response of the proposed method is fast due to the use of MPC. Besides, when the conventional modulation-based methods [65] have been applied to control the output currents, the maximum duty cycle has to be limited to guarantee sufficient commutation time. This means that these modulation-based methods cannot fully utilize the dc-link voltage when the MMC system operates at high modulation index or during transients. Instead, with the MPC method, we only need to ensure that the control interval for the outer loop is longer than the commutation period. Therefore, the utilization rate of the dc-link voltage will not be affected by the MPC method and a fast dynamic response can be achieved by using the

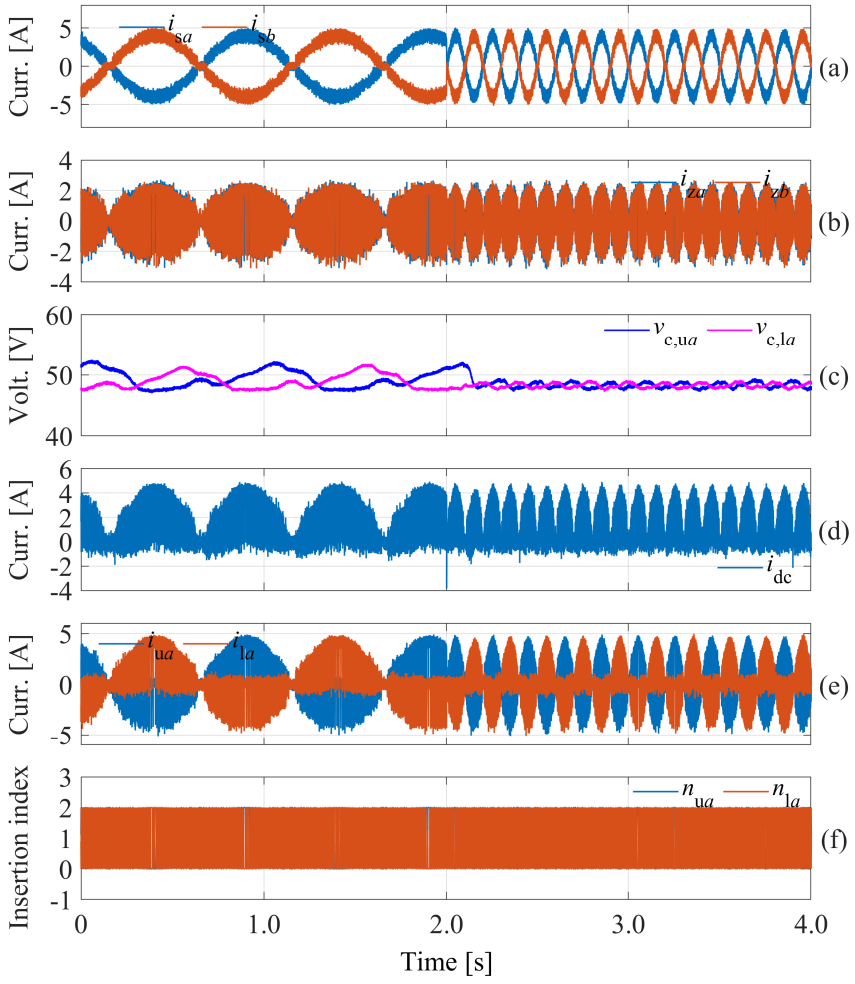

Figure 5.9: Step change in output frequency with the proposed method (from 1 Hz to 5 Hz).

proposed method. From Fig. 5.7(c), we can observe that the ripple magnitude of the capacitor voltage increases slightly when the output current increases. It is not difficult to analyze that as the output current increases, the commutation time will become longer, so the arm will accumulate more power.

Detail waveforms shown in Fig. 5.8 have been provided to further illustrate the principle of the proposed method. The commutation process can be clearly observed in Fig. 5.8(e) and Fig. 5.8(f). It can be seen that as the output current is small in this case, the arm current commutation process will be completed quickly. After finishing the current commutation, we will find that the arm carries the most output current while remaining short-circuited (all SMs in this arm are bypassed). Therefore, the fluctuation of the capacitor voltage shown in Fig. 5.8(c) is extremely low.

Fig. 5.9 shows the experimental results of the MMC operating in the Q2L mode with the proposed method under the step change in output frequency (from 1 Hz to 5 Hz). From Fig. 5.9(c) we can find that the capacitor voltage ripple decreases as the output frequency increases. However, a small steady-state error can be observed as the proposed method only works during the commutation process. This steady-state error can be eliminated when a high-frequency arm

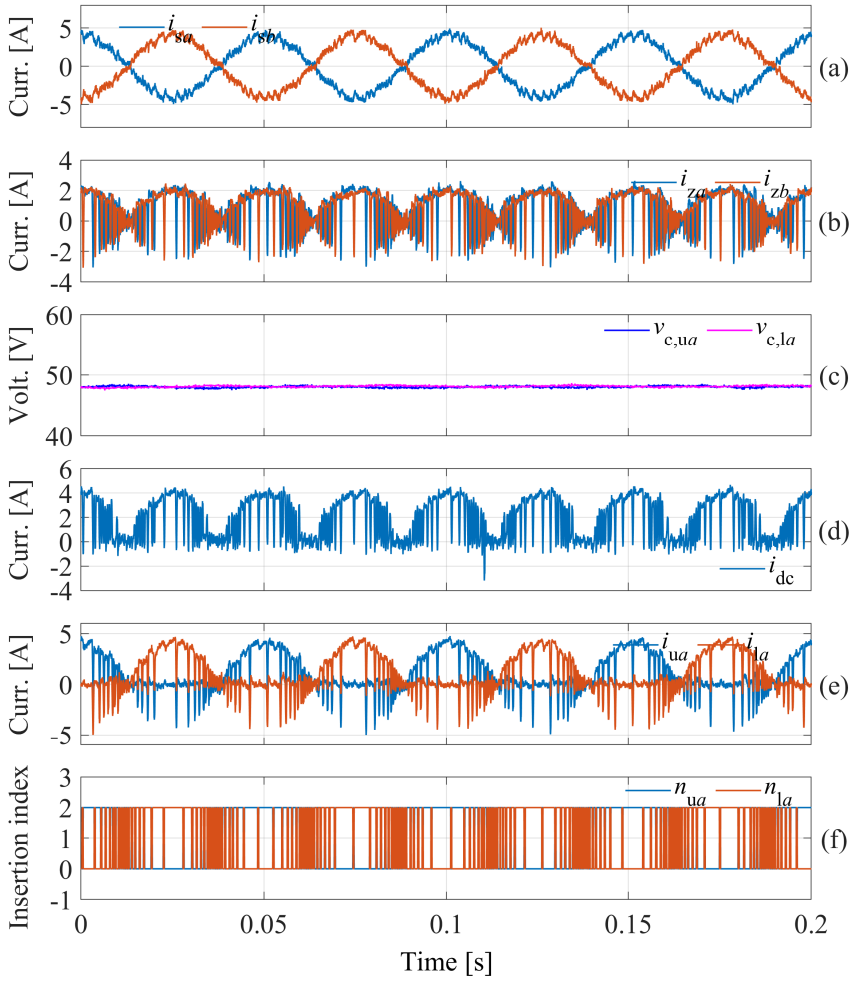

Figure 5.10: Steady-state performance of MMC operating at 20 Hz with proposed method.

energy controller is employed at steady state [62]. Although the proposed method is involved in voltage regulation for a short time, it can still ensure a stable operation of the MMC system.

At last, the steady-state performance of the MMC operating in the Q2L mode at high frequency (20 Hz) has been presented in Fig. 5.10. The commutation process can be easily found in Fig. 5.10(e) and Fig. 5.10(f). It can be observed that the ripple magnitude of SM capacitor voltage is further reduced at 20 Hz compared with that at 5 Hz. In this case, the fluctuation of the capacitor voltage is hardly observed. However, although the MMC system works well at high frequency in the Q2L mode, its output current performance is poor, as shown in Fig. 5.10(a). It should be noted that although the capacitor voltage suppression capability of the conventional method with the multilevel mode is not as good as that of the proposed method in Q2L mode, in the case of high frequency, the conventional method can also ensure that the capacitor voltage fluctuation is within a reasonable range. In contrast, since the conventional method can work in the multilevel mode, its output current performance is much better than the Q2L method. Therefore, in order to obtain a better performance of output currents, it is inevitable to switch the operation mode from Q2L mode to multilevel PWM mode.

5.7 Summary

This paper proposed a new arm current commutation control method using the MPC with extrapolation technique. By using the proposed method, the arm current commutation process can be controlled as the desired behavior (one arm supplies the load current but all SMs in this arm are bypassed). Therefore, the power fluctuation is significantly attenuated and the capacitor voltage ripple is suppressed. As the large voltage variation mainly occurs during the commutation process, the proposed method can complete this commutation process as quickly as possible. The effectiveness of the proposed arm current commutation method has been verified by simulation and experimental results.

CHAPTER 6

Conclusion

This dissertation is mainly carried out to solve the problem of applying MPC on MMC. The main challenges mentioned in Chapter 1:

1) how to decrease the computational complexity brought by MPC;

2) how to use MPC to realize the MMC-based motor drive application.

are answered. More specifically:

Chapter 3 proposes a unified method to solve the computational burden brought by MPC. The method first employs a fast bound-constrained quadratic programming method to obtain the continuous solution of the control problem constructed from the cost function. Then, this continuous solution can be used to realize the modulated MPC scheme. More importantly, the search space for the FCS-MPC method can be greatly reduced based on this obtained continuous solution. The number of insertion index combinations will be reduced from $(N+1)^6$ to 2^6, which is independent of the number of SMs per arm. Therefore, the proposed FCS-MPC method is very suitable for HVDC applications, in which N is large.

In Chapter 4, a novel cost function has been designed to allow the MMC to operate over a wide frequency range. A comparative study has been made to verify the effectiveness and superiority of the proposed method. It can be seen that the proposed method extends the modulation range compared with the circulating current injection method at low frequencies. Besides, it can also achieve better performance on the output currents at nominal operating conditions in comparison with the conventional MPC method. In addition, in order to achieve better steady-state performance and less calculation load, a modulated MPC method based on the proposed cost function has been implemented. Note that due to the ill-conditioned control problem, an exhaustive way to obtain the optimal insertion index has been proposed. In this way, this optimal solution can be found within a determined computational time. What's more, the computational burden is once again decoupled from the number of SMs per arm.

In the end, a particular operation mode (Q2L mode) of the MMC has been investigated. Such an operation mode not only guarantees the stable operation of MMC at low frequencies

but also facilitates the lightweight of the MMC. A key issue of Q2L mode is to ensure that when the upper arm and lower arm complete the current commutation, their corresponding arm currents are adjusted to the desired values at the same time. Conventional control methods are difficult to handle such control tasks as the system states need to experience a period to reach their desired values. These control tasks are more suitable to be handled by predictive control methods. Chapter 5 provides an efficient arm current commutation control method using MPC with extrapolation technique. By using this method, the commutation process can be completed as quickly as possible. As a result, large voltage fluctuations that occur during the commutation process will be avoided.

In this dissertation, some key issues regarding the application of MPC to MMC are discussed. As we know, the inherent drawbacks of MPC, such as computational complexity, hinder its wide application in MMC. This dissertation gives some solutions to such problems. Besides, it can be found that MPC has its unique advantages when applied to MMC. For example, compared with conventional modulation-based methods, FCS-MPC can achieve a lower average switching frequency under the same sampling frequency, resulting in lower power losses while ensuring the good steady-state performance of output currents. Also, MPC can fully utilize the dc-link voltage and easily achieve the trade-off of different control objectives. In addition, unlike the conventional method that requires different voltage balancing algorithms at high and low frequencies, we utilize the characteristics of MPC with multiple control modes to realize a novel capacitor voltage balancing method, which enables MMC to not only operate effectively at high frequencies but also achieve satisfactory performance at low frequencies. At last, the key issue of MMC operating in Q2L mode can be competently handled by MPC. In conclusion, it is necessary to study the MPC technique in MMC applications.

List of Figures

List of Tables

Bibliography

[1] N. Flourentzou, V. G. Agelidis, and G. D. Demetriades, "Vsc-based hvdc power transmission systems: An overview," *IEEE Transactions on Power Electronics*, vol. 24, no. 3, pp. 592–602, 2009.

[2] A. Nabae, I. Takahashi, and H. Akagi, "A new neutral-point-clamped pwm inverter," *IEEE Transactions on Industry Applications*, vol. IA-17, no. 5, pp. 518–523, 1981.

[3] B. Wu and M. Narimani, *High-power converters and AC drives*. John Wiley & Sons, 2017.

[4] S. Kouro, M. Malinowski, K. Gopakumar, J. Pou, L. G. Franquelo, B. Wu, J. Rodriguez, M. A. Pérez, and J. I. Leon, "Recent advances and industrial applications of multilevel converters," *IEEE Transactions on Industrial Electronics*, vol. 57, no. 8, pp. 2553–2580, 2010.

[5] T. Meynard and H. Foch, "Dispositif électronique de conversion d'énergie électrique," *French Patent*, vol. 267, p. 971, 1991.

[6] M. Marchesoni, M. Mazzucchelli, and S. Tenconi, "A non conventional power converter for plasma stabilization," in *PESC '88 Record., 19th Annual IEEE Power Electronics Specialists Conference*, 1988, pp. 122–129 vol.1.

[7] P. Hammond, "A new approach to enhance power quality for medium voltage ac drives," *IEEE Transactions on Industry Applications*, vol. 33, no. 1, pp. 202–208, 1997.

[8] A. Lesnicar and R. Marquardt, "An innovative modular multilevel converter topology suitable for a wide power range," in *2003 IEEE Bologna Power Tech Conference Proceedings,*, vol. 3, 2003, pp. 6 pp. Vol.3–.

[9] R. Marquardt, "Modular multilevel converters: State of the art and future progress," *IEEE Power Electronics Magazine*, vol. 5, no. 4, pp. 24–31, 2018.

[10] M. Saeedifard and R. Iravani, "Dynamic performance of a modular multilevel back-to-back hvdc system," in *2011 IEEE Power and Energy Society General Meeting*, 2011, pp. 1–1.

[11] G. J. Kish, M. Ranjram, and P. W. Lehn, "A modular multilevel dc/dc converter with fault blocking capability for hvdc interconnects," *IEEE Transactions on Power Electronics*, vol. 30, no. 1, pp. 148–162, 2015.

[12] A. Antonopoulos, L. Ängquist, S. Norrga, K. Ilves, L. Harnefors, and H. Nee, "Modular multilevel converter ac motor drives with constant torque from zero to nominal speed," *IEEE Transactions on Industry Applications*, vol. 50, no. 3, pp. 1982–1993, 2014.

[13] B. Li, S. Zhou, D. Xu, S. J. Finney, and B. W. Williams, "A hybrid modular multilevel converter for medium-voltage variable-speed motor drives," *IEEE Transactions on Power Electronics*, vol. 32, no. 6, pp. 4619–4630, 2017.

[14] M. Hagiwara, R. Maeda, and H. Akagi, "Negative-sequence reactive-power control by a pwm statcom based on a modular multilevel cascade converter (mmcc-sdbc)," *IEEE Transactions on Industry Applications*, vol. 48, no. 2, pp. 720–729, 2012.

[15] S. Du and J. Liu, "A study on dc voltage control for chopper-cell-based modular multilevel converters in d-statcom application," *IEEE Transactions on Power Delivery*, vol. 28, no. 4, pp. 2030–2038, 2013.

[16] Y. Long, X. Xiao, Y. Xu, B. Yu, Y. Xu, and J. Hao, "Mmc-upqc: Application of modular multilevel converter on unified power quality conditioner," in *2013 IEEE Power Energy Society General Meeting*, 2013, pp. 1–5.

[17] V. Khadkikar, "Enhancing electric power quality using upqc: A comprehensive overview," *IEEE Transactions on Power Electronics*, vol. 27, no. 5, pp. 2284–2297, 2012.

[18] L. Harnefors, A. Antonopoulos, S. Norrga, L. Angquist, and H.-P. Nee, "Dynamic analysis of modular multilevel converters," *IEEE Transactions on Industrial Electronics*, vol. 60, no. 7, pp. 2526–2537, 2013.

[19] Q. Tu, Z. Xu, and L. Xu, "Reduced switching-frequency modulation and circulating current suppression for modular multilevel converters," *IEEE Transactions on Power Delivery*, vol. 26, no. 3, pp. 2009–2017, 2011.

[20] Qingrui Tu, Zheng Xu, and Lie Xu, "Reduced switching-frequency modulation and circulating current suppression for modular multilevel converters," in *PES T D 2012*, 2012, pp. 1–1.

[21] X. She, A. Huang, X. Ni, and R. Burgos, "Ac circulating currents suppression in modular multilevel converter," in *IECON 2012 - 38th Annual Conference on IEEE Industrial Electronics Society*, 2012, pp. 191–196.

[22] Z. Li, P. Wang, Z. Chu, H. Zhu, Y. Luo, and Y. Li, "An inner current suppressing method for modular multilevel converters," *IEEE Transactions on Power Electronics*, vol. 28, no. 11, pp. 4873–4879, 2013.

[23] Z. Yuebin, J. Daozhuo, G. Jie, H. Pengfei, and L. Zhiyong, "Control of modular multilevel converter based on stationary frame under unbalanced ac system," in *2012 Third International Conference on Digital Manufacturing Automation*, 2012, pp. 293–296.

[24] J. Wang and P. Wang, "Decoupled power control for direct-modulation-based modular multilevel converter with improved stability," *IEEE Transactions on Industrial Electronics*, vol. 66, no. 7, pp. 5264–5274, 2019.

[25] A. Dekka, B. Wu, V. Yaramasu, R. L. Fuentes, and N. R. Zargari, "Model predictive control of high-power modular multilevel converters-an overview," *IEEE Journal of Emerging and Selected Topics in Power Electronics*, vol. 7, no. 1, pp. 168–183, 2019.

[26] A. Antonopoulos, L. Angquist, and H.-P. Nee, "On dynamics and voltage control of the modular multilevel converter," in *2009 13th European Conference on Power Electronics and Applications*, 2009, pp. 1–10.

[27] S. Cui, S. Kim, J. Jung, and S. Sul, "A comprehensive cell capacitor energy control strategy of a modular multilevel converter (mmc) without a stiff dc bus voltage source," in *2014 IEEE Applied Power Electronics Conference and Exposition - APEC 2014*, 2014, pp. 602–609.

[28] M. Hagiwara and H. Akagi, "Control and experiment of pulsewidth-modulated modular multilevel converters," *IEEE Transactions on Power Electronics*, vol. 24, no. 7, pp. 1737–1746, 2009.

[29] S. B. Bashir and A. R. Beig, "A novel svpwm-based switching algorithm for mmc for high power applications," in *2016 IEEE 59th International Midwest Symposium on Circuits and Systems (MWSCAS)*, 2016, pp. 1–4.

[30] K. Sekiguchi, P. Khamphakdi, M. Hagiwara, and H. Akagi, "A grid-level high-power btb (back-to-back) system using modular multilevel cascade converters withoutcommon dc-link capacitor," *IEEE Transactions on Industry Applications*, vol. 50, no. 4, pp. 2648–2659, 2014.

[31] A. E. Leon and S. J. Amodeo, "Energy balancing improvement of modular multilevel converters under unbalanced grid conditions," *IEEE Transactions on Power Electronics*, vol. 32, no. 8, pp. 6628–6637, 2017.

[32] J. Qin and M. Saeedifard, "Predictive control of a modular multilevel converter for a back-to-back hvdc system," *IEEE Transactions on Power Delivery*, vol. 27, no. 3, pp. 1538–1547, July 2012.

[33] J. Böcker, B. Freudenberg, A. The, and S. Dieckerhoff, "Experimental comparison of model predictive control and cascaded control of the modular multilevel converter," *IEEE Transactions on Power Electronics*, vol. 30, no. 1, pp. 422–430, 2015.

[34] J.-W. Moon, J.-S. Gwon, J.-W. Park, D.-W. Kang, and J.-M. Kim, "Model predictive control with a reduced number of considered states in a modular multilevel converter for hvdc system," *IEEE Transactions on Power Delivery*, vol. 30, no. 2, pp. 608–617, 2015.

[35] P. Liu, Y. Wang, W. Cong, and W. Lei, "Grouping-sorting-optimized model predictive control for modular multilevel converter with reduced computational load," *IEEE Transactions on Power Electronics*, vol. 31, no. 3, pp. 1896–1907, 2016.

[36] M. Vatani, B. Bahrani, M. Saeedifard, and M. Hovd, "Indirect finite control set model predictive control of modular multilevel converters," *IEEE Transactions on Smart Grid*, vol. 6, no. 3, pp. 1520–1529, May 2015.

[37] Z. Gong, P. Dai, X. Yuan, X. Wu, and G. Guo, "Design and experimental evaluation of fast model predictive control for modular multilevel converters," *IEEE Transactions on Industrial Electronics*, vol. 63, no. 6, pp. 3845–3856, 2016.

[38] F. Zhang, W. Li, and G. Joós, "A voltage-level-based model predictive control of modular multilevel converter," *IEEE Transactions on Industrial Electronics*, vol. 63, no. 8, pp. 5301–5312, 2016.

[39] J. Huang, B. Yang, F. Guo, Z. Wang, X. Tong, A. Zhang, and J. Xiao, "Priority sorting approach for modular multilevel converter based on simplified model predictive control," *IEEE Transactions on Industrial Electronics*, vol. 65, no. 6, pp. 4819–4830, 2018.

[40] B. Gutierrez and S. Kwak, "Modular multilevel converters (mmcs) controlled by model predictive control with reduced calculation burden," *IEEE Transactions on Power Electronics*, vol. 33, no. 11, pp. 9176–9187, 2018.

[41] X. Chen, J. Liu, S. Song, S. Ouyang, H. Wu, and Y. Yang, "Modified increased-level model predictive control methods with reduced computation load for modular multilevel converter," *IEEE Transactions on Power Electronics*, vol. 34, no. 8, pp. 7310–7325, 2019.

[42] A. Dekka, B. Wu, V. Yaramasu, and N. R. Zargari, "Dual-stage model predictive control with improved harmonic performance for modular multilevel converter," *IEEE Transactions on Industrial Electronics*, vol. 63, no. 10, pp. 6010–6019, 2016.

[43] ——, "Integrated model predictive control with reduced switching frequency for modular multilevel converters," *IET Electric Power Applications*, vol. 11, no. 5, pp. 857–863, 2017.

[44] T. Geyer, *Model predictive control of high power converters and industrial drives*. John Wiley & Sons, 2016.

[45] H. Mahmoudi, M. Aleenejad, and R. Ahmadi, "Modulated model predictive control of modular multilevel converters in vsc-hvdc systems," *IEEE Transactions on Power Delivery*, vol. 33, no. 5, pp. 2115–2124, 2018.

[46] Z. Gong, X. Wu, P. Dai, and R. Zhu, "Modulated model predictive control for mmc-based active front-end rectifiers under unbalanced grid conditions," *IEEE Transactions on Industrial Electronics*, vol. 66, no. 3, pp. 2398–2409, March 2019.

[47] J. Wang, X. Liu, Q. Xiao, D. Zhou, H. Qiu, and Y. Tang, "Modulated model predictive control for modular multilevel converters with easy implementation and enhanced steady-state performance," *IEEE Transactions on Power Electronics*, vol. 35, no. 9, pp. 9107–9118, 2020.

[48] M. Narimani, B. Wu, V. Yaramasu, Z. Cheng, and N. R. Zargari, "Finite control-set model predictive control (fcs-mpc) of nested neutral point-clamped (nnpc) converter," *IEEE Transactions on Power Electronics*, vol. 30, no. 12, pp. 7262–7269, 2015.

[49] P. Cortes, S. Kouro, B. La Rocca, R. Vargas, J. Rodriguez, J. I. Leon, S. Vazquez, and L. G. Franquelo, "Guidelines for weighting factors design in model predictive control of power converters and drives," in *2009 IEEE International Conference on Industrial Technology*, 2009, pp. 1–7.

[50] K. Kunisch and F. Rendl, "An infeasible active set method for quadratic problems with simple bounds," *SIAM Journal on Optimization*, vol. 14, no. 1, pp. 35–52, 2003.

[51] W. Yang, Q. Song, and W. Liu, "Decoupled control of modular multilevel converter based on intermediate controllable voltages," *IEEE Transactions on Industrial Electronics*, vol. 63, no. 8, pp. 4695–4706, 2016.

[52] J. Yin, J. I. Leon, M. A. Perez, L. G. Franquelo, A. Marquez, and S. Vazquez, "Model predictive control of modular multilevel converters using quadratic programming," *IEEE Transactions on Power Electronics*, vol. 36, no. 6, pp. 7012–7025, 2021.

[53] A. Dekka, B. Wu, V. Yaramasu, and N. R. Zargari, "Model predictive control with common-mode voltage injection for modular multilevel converter," *IEEE Transactions on Power Electronics*, vol. 32, no. 3, pp. 1767–1778, 2017.

[54] M. A. Perez, S. Bernet, J. Rodriguez, S. Kouro, and R. Lizana, "Circuit topologies, modeling, control schemes, and applications of modular multilevel converters," *IEEE Transactions on Power Electronics*, vol. 30, no. 1, pp. 4–17, 2015.

[55] W. Tian, X. Gao, and R. Kennel, "Model predictive control of modular multilevel converters with independent arm-balancing control," in *2019 IEEE International Symposium on Predictive Control of Electrical Drives and Power Electronics (PRECEDE)*, May 2019, pp. 1–5.

[56] B. Li, S. Zhou, D. Xu, R. Yang, D. Xu, C. Buccella, and C. Cecati, "An improved circulating current injection method for modular multilevel converters in variable-speed drives," *IEEE Transactions on Industrial Electronics*, vol. 63, no. 11, pp. 7215–7225, 2016.

[57] R. Yang, B. Li, G. Wang, C. Cecati, S. Zhou, and D. Xu, "Asymmetric mode control of mmc to suppress capacitor voltage ripples in low-frequency, low-voltage conditions," *IEEE Transactions on Power Electronics*, vol. 32, no. 6, pp. 4219–4230, 2017.

[58] A. J. Korn, M. Winkelnkemper, and P. Steimer, "Low output frequency operation of the modular multi-level converter," in *2010 IEEE Energy Conversion Congress and Exposition*, 2010, pp. 3993–3997.

[59] S. Debnath, J. Qin, and M. Saeedifard, "Control and stability analysis of modular multilevel converter under low-frequency operation," *IEEE Transactions on Industrial Electronics*, vol. 62, no. 9, pp. 5329–5339, 2015.

[60] M. Hagiwara, I. Hasegawa, and H. Akagi, "Start-up and low-speed operation of an electric motor driven by a modular multilevel cascade inverter," *IEEE Transactions on Industry Applications*, vol. 49, no. 4, pp. 1556–1565, 2013.

[61] J. Jung, H. Lee, and S. Sul, "Control strategy for improved dynamic performance of variable-speed drives with modular multilevel converter," *IEEE Journal of Emerging and Selected Topics in Power Electronics*, vol. 3, no. 2, pp. 371–380, 2015.

[62] A. Mertens and J. Kucka, "Quasi two-level pwm operation of an mmc phase leg with reduced module capacitance," *IEEE Transactions on Power Electronics*, vol. 31, no. 10, pp. 6765–6769, 2016.

[63] C. Wang, K. Wang, Z. Zheng, and Y. Li, "A new control strategy for modular multilevel converter operating in quasi two-level pwm mode," in *2018 International Power Electronics Conference (IPEC-Niigata 2018 -ECCE Asia)*, 2018, pp. 2386–2392.

[64] X. Gao, W. Tian, Z. Zhang, and R. Kennel, "Model predictive control with extrapolation strategy for the arm current commutation control of modular multilevel converter operating in quasi two-level mode," in *2019 10th International Conference on Power Electronics and ECCE Asia (ICPE 2019 - ECCE Asia)*, 2019, pp. 1–6.

[65] J. Kucka and A. Mertens, "Improved current control for a quasi-two-level pwm-operated modular multilevel converter," *IEEE Transactions on Power Electronics*, vol. 35, no. 7, pp. 6842–6853, 2020.

[66] S. Du, B. Wu, N. R. Zargari, and Z. Cheng, "A flying-capacitor modular multilevel converter for medium-voltage motor drive," *IEEE Transactions on Power Electronics*, vol. 32, no. 3, pp. 2081–2089, 2017.

[67] Y. S. Kumar and G. Poddar, "Control of medium-voltage ac motor drive for wide speed range using modular multilevel converter," *IEEE Transactions on Industrial Electronics*, vol. 64, no. 4, pp. 2742–2749, 2017.

[68] J. Kucka and A. Mertens, "Control for quasi two-level pwm operation of modular multilevel converter," in *2016 IEEE 25th International Symposium on Industrial Electronics (ISIE)*, 2016, pp. 448–453.

[69] P. Hu and D. Jiang, "A level-increased nearest level modulation method for modular multilevel converters," *IEEE Transactions on Power Electronics*, vol. 30, no. 4, pp. 1836–1842, 2015.